UNIVERSIDADE DE LISBOA
FACULDADE DE CIÊNCIAS
DEPARTAMENTO DE CIÊNCIAS DA TERRA E ENERGIA

# Temperature control in the evaluation of degradation parameters of LFP batteries

Santo Giuseppe Coccoluto Pestana

**Mestrado em Engenharia da Energia e Ambiente**

Dissertação orientada por:
Killian Paulo Kiernan Lobato

2025

# Acknowledgements

Agradeço à Faculdade e a todos os professores que me acompanharam ao longo desta caminhada, bem como pelas aprendizagens que me transmitiram ao longo do percurso, em especial ao meu orientador Killian Lobato, pelo apoio e orientação prestados ao longo deste trabalho.

Ao Hélder e à Beatriz, por serem aquelas pessoas que me acompanharam desde que entrei na faculdade e por terem sido sempre um suporte que, muitas vezes, me permitiu pensar fora da caixa; através das risadas resultantes de tantas conversas, elevaram com humor o meu nível de exigência.

À Leonor, por ter sido aquela pessoa, já no mestrado, com a qual me consegui identificar, por prestar palavras de apoio de forma constante e, não menos importante, pelas fofocas e conversas sobre séries que mantivemos em dia, criando nomes criativos para todas as pessoas que cruzaram a nossa vida académica.

A Manuel y Germán, por haber sido esos amigos constantes que, aunque la vida haga que nos veamos cada vez menos, cuando lo hagamos todo siga siendo igual que siempre, siendo personas en las que puedo confiar plenamente y que quiero tener a mi lado el resto de mi vida.

A mi familia, en especial a mi mamá y a mis hermanas Nathalie y Stephanie, junto con sus esposos Christián e Iván, por haber estado siempre pendientes de mí a lo largo del camino, y, aunque no entendieran mucho de mi tesis, por estar presentes en este momento y a lo largo de toda mi vida, ayudándome a alcanzar todos estos hitos.

Por último, a mi novia Ana, por ser la persona que lidió con todos mis estrés relacionados con la tesis y que fue siempre una fuente de alívio en cada momento, siendo mi pilar principal; sin su presencia y su amor paciente, este documento nunca habría sido posible.

# Resumo

A dissertação apresentada centra-se na necessidade de explorar soluções que garantam a implementação de fontes renováveis de energia sem constrangimentos no consumo energético devido à sua variabilidade, através de sistemas de armazenamento de energia. Os Objetivos de Desenvolvimento Sustentável (ODS) propostos pelas Nações Unidas exigem a exploração de sistemas tais como as baterias de ião de lítio, desenvolvidas pelos laureados com o Nobel John B. Goodenough, M. Stanley Whittingham e Akira Yoshino, cujos avanços permitiram a criação de tecnologias, tais como as baterias de fosfato de ferro-lítio (LFP), caracterizadas por uma baixa densidade energética, mas longa vida útil, tornando-se uma alternativa para sistemas de armazenamento estacionário, também destacadas pela sua rentabilidade no mercado.

Os objetivos principais deste trabalho baseiam-se na caracterização eletroquímica de baterias LFP através de Espectroscopia de Impedância Eletroquímica (EIS), analisando a evolução do seu comportamento com o aumento do número de ciclos, sob diferentes temperaturas controladas e identificando as alterações específicas nos espectros de impedância, bem como na possibilidade de estimar o número de ciclos de uma bateria com as mesmas características, recorrendo à análise do espectro de impedância a diferentes temperaturas e dos parâmetros dos modelos de circuitos equivalentes (ECM) obtidos no ajuste.

Na estrutura do trabalho constam cinco capítulos, sendo que o primeiro aborda o conceito de sistemas de armazenamento encaixados como facilitadores de uma transição energética renovável, analisando especificamente a tecnologia LFP e a sua rentabilidade, adoção e crescimento no mercado atual, tanto na mobilidade como em sistemas de armazenamento estacionário. A adoção desta tecnologia é um promotor dos ODS, tais como os ODS 9 e 13, relacionados com a inovação de infraestruturas e com o combate às alterações climáticas, através do desenvolvimento de tecnologias para a mobilidade elétrica e o armazenamento de energia, permitindo o aumento da penetração renovável que contribui para a descarbonização da energia. Outro ODS favorecido está relacionado com cidades e comunidades sustentáveis, visto que os sistemas de armazenamento permitem uma maior estabilidade da produção renovável.

O segundo capítulo, está relacionado com o funcionamento de uma bateria de lítio, tanto no seu processo de carga como descarga, que se baseia no movimento de iões entre o ânodo e o cátodo, através do eletrólito e do separador. São apresentados diferentes tipos de baterias de lítio sendo de especial destaque as LFP e as de Níquel-Manganês-Cobalto (NMC), as mais comercializadas na Europa, que destacam pela sua alta densidade energética, mas caraterizam-se por uma reduzida esperança de vida. Nesta comparativa a LFP, emerge como uma solução pouco densa energeticamente, mas de grande durabilidade e estabilidade.

Neste capítulo é realizada uma revisão das métricas mais comuns na caracterização de sistemas de armazenamento: a profundidade de descarga (DOD), que indica a quantidade de energia utilizada em relação à sua capacidade total; o estado de carga (SOC), que indica a capacidade da bateria em relação à sua capacidade máxima; a resistência interna, que expressa a oposição da bateria à corrente; o estado de saúde da bateria (SOH), que expressa o decaimento da capacidade com o número de ciclos; e, por último, o C-rate, que expressa a taxa a que a bateria é carregada ou descarregada.

Estes indicadores podem propiciar alterações ou ser afetados por diferentes mecanismos de degradação, incluindo o crescimento da Interfase Eletrolítica Sólida (SEI), que consome lítio ativo e reduz a capacidade; o *plating* de lítio, podendo originar dendrites; as fraturas nas partículas, resultantes das variações de volume que conduzem a reações secundárias; a perda de material ativo, que diminui a saúde da bateria; e as vibrações, que geram tensões internas e aceleram reações irreversíveis.

Por último, o segundo capítulo finaliza com a introdução de métodos de caracterização eletroquímica de baterias, destacando-se o EIS, que avalia sistemas eletroquímicos aplicando um pequeno sinal sinusoidal e analisando a resposta em corrente ou tensão a diferentes frequências. Ao contrário de outros testes, a EIS estuda a impedância no domínio da frequência, fornecendo informações sobre a interfase sólido-líquido e a dinâmica de transferência de carga. São ainda abordados os efeitos térmicos e de ciclagem no espetro, bem como diferentes parâmetros do ECM registados na literatura.

O terceiro capítulo divide-se em quatro subcapítulos. Inicialmente, são apresentadas as especificações técnicas das baterias, oito LFP de 3,2 V e 200 mAh. De seguida, definem-se os protocolos de ciclagem de acordo com os limites estabelecidos anteriormente, submetendo as baterias a um ciclo padrão de carga a 0,5 C e descarga a 1 C, utilizando o protocolo Corrente Constante – Tensão Constante (CC–CV) com tensão de corte de 3,6 V. Antes de cada descarga, é realizado um tempo de repouso, seguido de descarga CC até atingir o limite inferior de 2,5 V. Este processo é repetido 10 vezes para definir a capacidade inicial da bateria. Todas as medições foram efetuadas com um analisador MTI BST de 8 canais, capaz de controlar tensão e corrente de cada canal independentemente.

Posteriormente, para caracterizar eletroquimicamente as baterias ao longo da sua vida útil, foram realizadas medições de impedância a diferentes frequências (FRA) e SOC diferentes, começando em 100% e em intervalos de 10%. As medições foram efetuadas com o PGSTAT302N da *Metrohm Autolab*, utilizando a técnica galvanostática, adequada a sistemas de baixa impedância, onde pequenas variações de tensão provocam respostas de corrente instáveis. Durante a experiência, o *Autolab* aplica uma corrente de descarga igual à capacidade nominal durante seis minutos, garantindo o descarregamento de 10% do SOC, seguido de medições FRA entre 10 kHz e 0,1 Hz, obtendo um total de 45 pontos.

Durante os testes de EIS, o controlo de temperatura é assegurado por um cilindro de plástico hermético, preenchido com óleo mineral não condutor, colocado dentro de um banho refrigerado com termóstato (*B. Braun Frigomix FX-U*) contendo uma mistura de água e glicol. Sensores de temperatura no banho e no óleo permitem ajustar a temperatura da bateria, enquanto a agitação garante a uniformidade térmica.

Após a realização dos testes de impedância, séries de dados foram ajustadas recorrendo ao ECM de primeira ordem, de forma a representar o comportamento da bateria nas diferentes situações (número de ciclos, SOC e temperatura) através de um circuito elétrico, permitindo que o circuito obtido descreva as características da bateria, com os seus três elementos principais: Resistência em Série, Resistência de Transferência de Carga e impedância de *Warburg*.

A análise de resultados foi dividida em quatro seções, sendo que a primeira consiste na avaliação da capacidade da bateria ao longo da ciclagem. No caso das LFP analisadas, a capacidade das baterias difere da estipulada nas especificações técnicas, mas observa-se que não há um decaimento da mesma.

Subsequentemente, foram analisados os espectros de impedância, de forma a avaliar a similitude entre as baterias. Foram identificadas duas baterias que se diferenciavam do comportamento das restantes, apresentando um diâmetro no semicírculo superior ao das restantes. A análise posterior foi realizada com base no valor médio obtido para as seis baterias semelhantes. Pela avaliação dos espectros médios, observa-se a diminuição do diâmetro do semicírculo (Resistência de Transferência de Carga) com o aumento da temperatura, indicando que a temperatura mais elevada facilita a intercalação de iões de lítio. Na análise do espectro, é evidente que o SOC praticamente não gera variações, exceto nos valores a 100%, onde o ECM selecionado não proporcionou um ajuste eficiente nas baixas frequências, apresentando um comportamento anómalo.

Na sequência da análise espectral através do ajuste do ECM, foi possível analisar mais profundamente o efeito da ciclagem no desempenho eletroquímico das baterias. A resistência em série, que representa a interseção do espectro com o eixo das abcissas, não apresentou alterações relacionadas

com variações de temperatura, enquanto os resultados apontaram um aumento desta resistência com o número de ciclos das LFP.

A Resistência de Transferência de Carga demonstrou uma alta dependência da temperatura, atingindo valores máximos a 0 ºC e mínimos a 20 ºC, sem tendências diretamente relacionadas com o número de ciclos. Tanto a resistência em série como a de transferência de carga não apresentam grandes mudanças com a evolução do SOC. No caso da impedância de *Warburg*, foi analisada a admitância, que aumentou à medida que a temperatura subia, enquanto os efeitos da ciclagem indicam um aumento da admitância, associado à migração de iões. A análise dos parâmetros do ECM e dos espetros de impedância permite identificar tendências úteis para estimar o número de ciclos de uma bateria LFP desconhecida

Em resumo, os resultados mostram que a capacidade das LFP, no período estudado, se manteve estável, embora a resistência em série tenha aumentado com o número de ciclos. Com o aumento da temperatura, a admitância de *Warburg* também aumentou, refletindo melhor difusão iónica. A resistência de transferência de carga diminuiu com a subida da temperatura, favorecendo a velocidade de reação e a migração dos iões de lítio. Para trabalhos futuros, recomenda-se realizar ciclagens mais rápidas (maior degradação), testar as baterias a temperaturas mais altas, DOD inferiores, aumentar a resolução dos dados experimentais e explorar ajustes com ECM alternativos, especialmente para SOC de 100%, de forma a melhorar a capacidade de estimar o número de ciclos duma bateria.

**Palavras-chave**: Espectroscopia de Impedância Eletroquímica (EIS), Baterias de fosfato de ferro-lítio (LFP), Modelo de Circuito Equivalente (ECM), Dependência da temperatura.

# Abstract

This study is motivated by the need for energy storage to achieve Sustainable Development Goals related to clean energy integration and to balance the consumption and production of variable renewable sources. Lithium iron-phosphate (LFP) is a recently commercialized battery with long lifespan and lower energy density compared to other lithium technologies, ideal for stationary storage systems. It has been proven that their electrochemical behavior is temperature dependent, highlighting the need to control temperature to observe changes in performance. The objective of this dissertation is to develop a temperature-controlled setup to investigate LFP degradation during cycling, by studying the electrochemical performance at different temperatures through Electrochemical Impedance Spectroscopy (EIS), and by identifying trends in the Equivalent Circuit Model (ECM) and impedance to determine the ageing of the LFP.

The methods involved standard cycling according to specifications, combined with EIS at every 10% SOC. This allowed monitoring of parameters obtained by fitting the data to an electrical circuit. Measurements were performed on eight batteries at 11 SOC levels, across five temperatures (0–20°C), and four ageing stages (10–450 cycles).

The capacity evolution during cycling showed no fade, indicating that the conditions were non-damaging for the LFP cells. The obtained spectra, with the selected ECM, were successfully fitted, except for the data at 100% SOC. Outliers were identified in the spectra and the ECM parameters. The analysis indicated the temperature dependence of Warburg admittance and Charge Transfer Resistance, with Warburg admittance elevated and Charge Transfer Resistance decreasing, alongside slight variations with SOC and cycling. In contrast, the Series Resistance provided indications of degradation, increasing with cycling while showing no temperature dependence. Further research is needed to include a higher number of cycles, accelerated degradation rates, and alternative ECMs for fitting, to achieve a more comprehensive understanding of the battery's electrochemical degradation mechanisms.

**Keywords:** Electrochemical Impedance Spectroscopy (EIS), Lithium iron-phosphate (LFP), Equivalent Circuit Model (ECM), Temperature dependence.

# Abbreviations and Acronyms

| | |
|---|---|
| AC | Alternating Current |
| CPE | Constant Phase Element |
| DC | Direct Current |
| DOD | Depth Of Discharge |
| ECM | Equivalent Circuit Model |
| EIS | Electrochemical Impedance Spectroscopy |
| FRA | Frequency Response Analysis |
| IEA | International Energy Agency |
| LDVs | Light Duty Vehicles |
| LIBs | Lithium-Ion Batteries |
| LCO | Lithium Cobalt Oxide |
| LFP | Lithium Iron Phosphate |
| LMO | Lithium Manganese Oxide |
| NCA | Lithium Nickel Cobalt Aluminum Oxide |
| NMC | Lithium Nickel Manganese Cobalt Oxide |
| SOC | State of Charge |
| SEI | Solid Electrolyte Interphase |
| SOH | State of Health |
| SDG | Sustainable Development Goals |

# Symbology

| | | |
|---|---|---|
| $C$ | Capacitance | [F] |
| $CPE$ | Constant phase element | [S s $^{n}$ ] |
| $I$ | Current | [A] |
| $L$ | Inductance | [H] |
| $R$ | Resistance | [Ω] |
| $R_{ct}$ | Charge Transfer Resistance | [Ω] |
| $R_s$ | Series Resistance | [Ω] |
| $V$ | Voltage | [V] |
| $Y_0$ | Constant Phase Element Constan | [S s $^{0.5}$ ] |
| $Z$ | Impedance | [Ω] |
| $Z'$ | Real Impedance | [Ω] |
| $Z''$ | Imaginary Impedance | [Ω] |
| $\varphi$ | Phase difference | [rad] |
| $\omega$ | Angular Frequency | [rad/s] |

# Index

# List of figures

# List of Tables

# List of equations

# 1 Introduction

## 1.1 Framework

In the past, lithium-ion batteries were not considered a solution for energy storage in large-scale applications or small appliances due to changes in their electrochemical characteristics over different numbers of cycles and varying temperatures during their lifespan[1]. Currently, lithium-ion batteries (LIBs) are commonly used in all types of applications such as electric vehicles or storage systems. Research in the field has shown significant advancement, marked by the contributions to the development of the chemistry Nobel prize winners John B. Goodenough, M. Stanley Whittingham and Akira Yoshino[2].

These contributions led to the invention of functional lithium-ion batteries (LIBs), a groundbreaking rechargeable storage technology. Over time, LIBs have achieved extensive implementation, incorporating various chemistries, such as lithium iron phosphate (LFP) batteries. The LFP was first introduced in 1997, [3] with again, the participation of Nobel Prize laureate John B. Goodenough, has become one of the most widely used chemistries globally. LFP batteries are now key enablers of the decarbonization of the mobility sector and the management of the disparities between energy consumption and production introduced by renewable energy, thereby contributing significantly to the achievement of the United Nations Sustainable Development Goals.

With the transition to renewable energy and technological growth, selected Sustainable Development Goals (SDGs) are becoming closer to being fulfilled through the use of storage technologies, such as lithium-ion batteries. The aim of ensuring access to affordable, reliable, sustainable, and modern energy for all (SDG number seven), can be supported by addressing the intermittency of the non-dispatchable technologies like photovoltaic and wind power production, where we can store surplus energy generated during peak production hours to address the deficits in variable renewable energy sources production [4].

Batteries are critical factors of innovation in the mobility sector. With the growing adoption of electric and hybrid vehicles, they play a crucial role in reducing direct carbon emissions, contributing significantly to decarbonization, and the development of advanced battery technologies that will be essential to power the future of electric mobility (objective nine and thirteen). As we can find in recent reports from IEA[5], there has been a reduction in emissions on the part of the most recognized automotive brands with the introduction of electrification and hybrid technologies in the transport sector.

Another goal that will be reinforced is Sustainable Cities and Communities (objective number eleven). The use of batteries to store self-produced energy by prosumers will allow greater independence from the grid, promoting sustainability and energy resilience, and also, decentralization of energy production [6]. Additionally, the introduction of battery swapping technologies, which enhance the efficiency of charging processes, is an essential innovation to accelerate the adoption of electric vehicle mobility and to ensure the increase of the battery life [7].

The growing need to adopt energy storage technologies has driven the investigation of lithium-ion batteries (LIBs), due to their high specific energy, long lifespan, high specific power, and high efficiency in each cycle (charge and discharge processes) [7]. Additionally, the significant rise in demand for LIBs in recent years, from around 100 GWh in 2018 to almost 1000 GWh in 2024 of total installed capacity, shows an increase of 65 % in the global electric vehicle market, This growing penetration of LIBs in the mobility sector, has powered efforts to enhance battery performance and electrochemical characterization, with an interest on understanding the mechanisms behind battery degradation. [8,9].

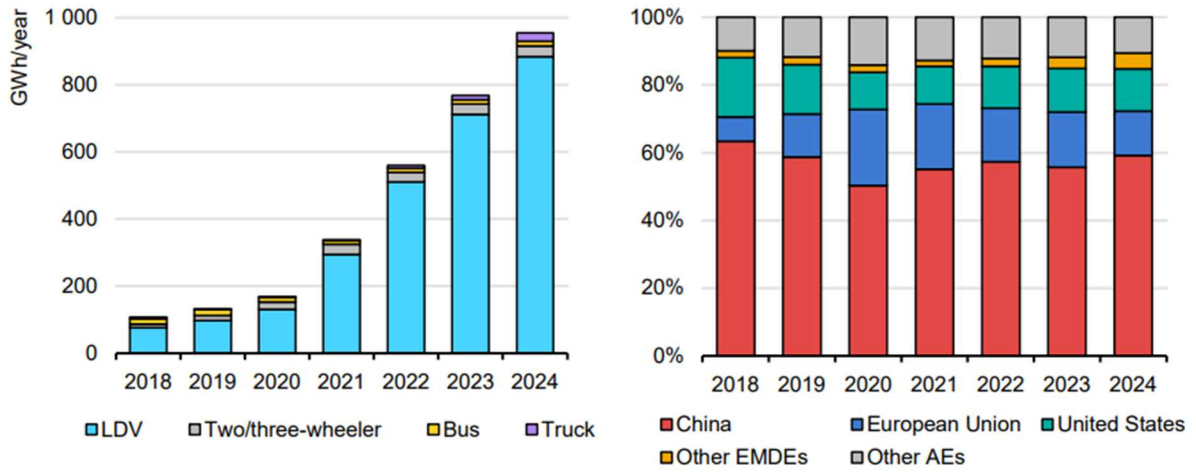


Figure 1.1.1: Annual battery demand by transportation mode (light-duty vehicles [LDVs], buses, and other modes) and by penetration by region (China, Europe, the United States, and other regions) from 2018 to 2024 [5].

More specifically, regarding Lithium Iron Phosphate (LFP) chemistry, there has been an increase in its market penetration, as indicated in recent reports from IEA [5]. This is directly related to continuing efforts to increase the lifespan of the batteries, while keeping production and distribution costs low. This technology (LFP) is the most affordable option on the actual market, and when comparing prices across regions, the differences have become smaller in recent years, with costs converging and showing only slight variations, as shown in the figure below:

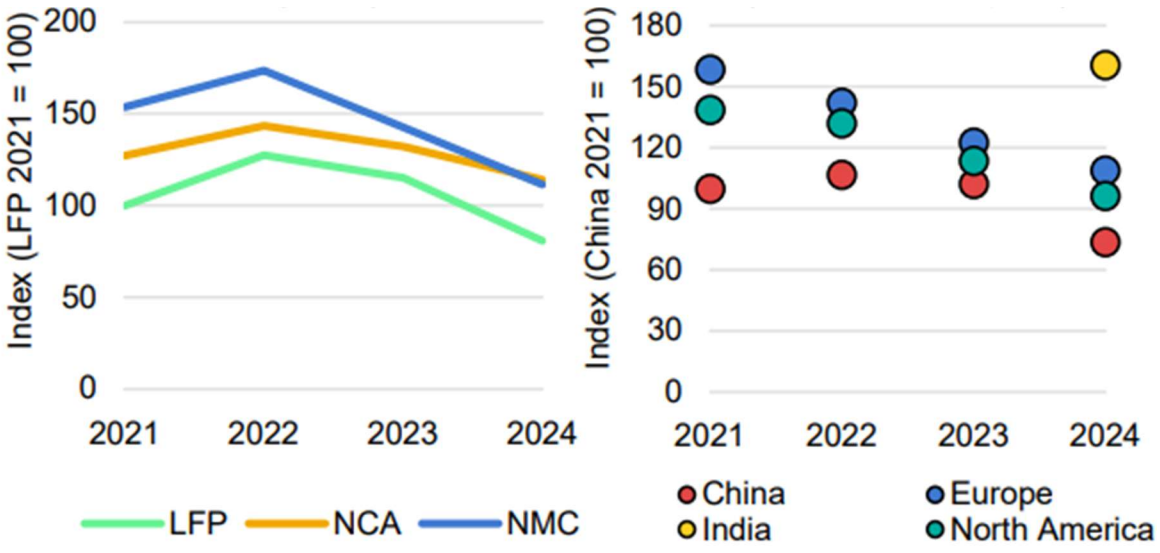


Figure 1.1.2: Average battery price index by chemistry (LFP: lithium iron phosphate, NCA: nickel cobalt aluminum, NMC: nickel manganese cobalt) and by region (China, Asia Pacific, North America, and Europe) from 2021 to 2024 [5].

In this figure, it is noted that the fixed index is set at 100, serving as a reference point to determine changes in prices over time. The LFP technology is the cheapest option and, therefore, represents the base index value (100). In the past years, Nickel Manganese Cobalt (NMC) and Nickel Cobalt Aluminum (NCA) chemistry, both of which will be discussed further in this study, have been

priced above LFP technology, with costs at least 40-50% higher. On the right side of the figure, the baseline is shown as LFP in China, representing the lowest cost. It is also observed that prices in Europe and North America are 50-60% higher. Additionally, the percentage difference in prices has decreased over time, in 2021, the gap between the cheapest and most expensive market was closely 70%, while by 2024, this difference had decreased to 20%, except from India

In the last five years, LFP market penetration has increased deeply. By 2024, they accounted for approximately 50% of the global electric vehicle market, from just almost 40% in 2022. This surge has been performed mostly by China, where the majority of EVs use LFP technology. Meanwhile, in Europe and the United States, the adoption of LFP batteries for electric vehicles remains limited, with less than 10% of EVs relying on this chemistry.

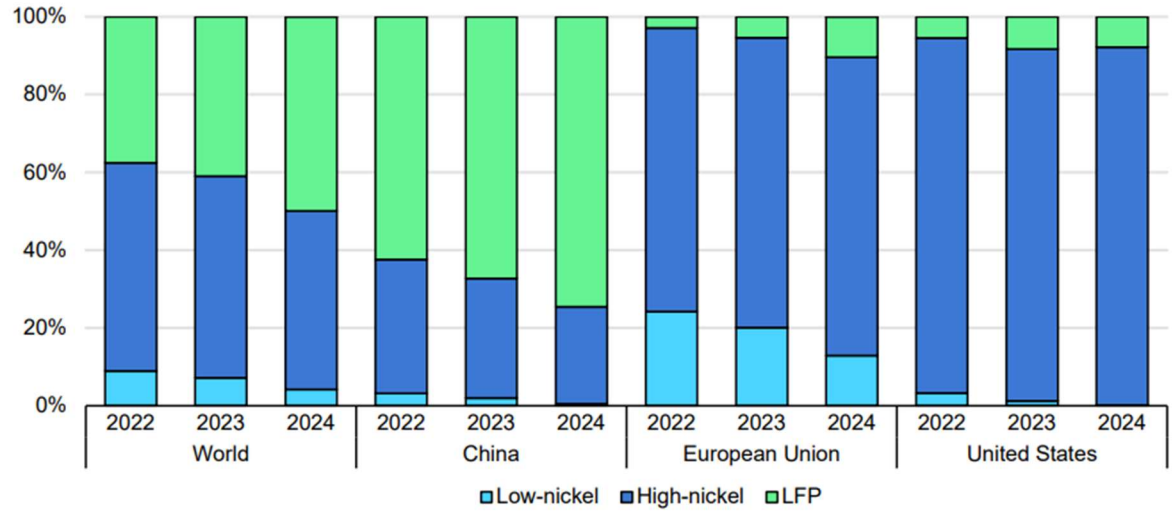


Figure 1.1.3: Share of battery capacity of electric vehicles by chemistry and region [5]

The figure clearly shows China's role in the global electric vehicle market, influencing the adoption of LFP technology worldwide. In Europe, the penetration of electric vehicles and LFP has been slower, this is related to the lack of adoption of LFP chemistries in vehicle storage solutions.

## 1.2 Objectives and Research Questions

The primary objective of this research is to develop a laboratory setup that enables electrochemical impedance tests (as the main tool) under controlled range of temperatures and after specific cycle numbers, in order to electrochemically characterize LFP batteries and gain a better understanding of the temperature and aging effects discussed in the literature, in the impedance spectra and electrical circuit components.

This study aims to electrochemically characterize a selected batch of LFP batteries, for which no public data exists, and which features a typical configuration representative of other similar LFP cells.

By the end of this study, the intention is to answer the following research question:

1. How does the electrochemical characterization 10430 200 mAh 3,2V LFP battery, as assessed through EIS tests, change with varying lifespan (number of cycles) under different controlled temperatures; and what specific changes can be observed in the impedance spectra.

2. Can the approximate lifespan of a lithium iron phosphate (LFP) battery with similar characteristics be estimated by analysing its impedance spectra and discharge curve, using comparison with data from 8 measured LFP batteries?

In the next section, it will be demonstrated that controlling temperature and ageing during Electrochemical Impedance Spectroscopy (EIS) is crucial, as the technique is sensitive to variations in temperatures and number of cycles.

## 1.3 Structure of the Dissertation

The dissertation is divided into 5 chapters. Chapter 1 introduces the context and structure of the study and presents the research questions addressed in this work. Chapter 2 supplies the theoretical background necessary to understand the state of the art of LIBs, including degradation mechanisms, commonly used techniques for electrochemical characterization such as electrochemical impedance spectroscopy (EIS), and the reported effects of temperature and ageing on LFP technology.

Chapter 3 describes the laboratory setups and experimental protocols employed for cycling tests, EIS and temperature control. Chapter 4 presents the analysis of the results obtained from cycling and EIS measurements at various stages and cycle numbers. The analysis begins with the evolution of capacity, followed by the interpretation of impedance spectra and fitting procedures, and concludes with the equivalent circuit model parameters, which help to understand the performance changes of the batteries during this study.

Chapter 5 summarizes the main conclusions of the study and gives suggestions for future research that could be used as a starting point for deeper research in LFP technology. Finally, the Attachments, are divided into two main sections: the first contains the impedance spectra of all eight batteries under different conditions, including examples for individual batteries, while the second presents the laboratory protocols and setups.

# 2 Literature review

The chapter begins by introducing the fundamentals of lithium-ion batteries (LIBs), including lithium iron phosphate (LFP) batteries, and explaining the basic functioning of these batteries, such as the interaction between the electrodes and the electrolyte during charge and discharge processes. It then presents and compares the most commonly adopted types of lithium-ion batteries, with a primary focus on their applications.

Additionally, key metrics for assessing battery condition are defined, providing a better understanding of the stressors and thermal issues that affect battery performance and the electrode-electrolyte structure.

Finally, the chapter introduces a technique for electrochemical characterization of LFP batteries, emphasizing the effects of ageing and controlled temperature on the impedance spectra and the corresponding equivalent circuit model [10,11,12] .

## 2.1 Fundamentals of LIBs batteries

LIBs batteries operate through the movement of lithium ions between two electrodes (anode and cathode) separated by a porous membrane and facilitated by an ion-conducting electrolyte. A battery cycle is composed of two phases, the discharge process, where the lithium ions are withdrawn from the anode (negative electrode, usually made of graphite or amorphous carbon), to be transferred via the electrolyte and separator to the cathode (positive electrode). [7,13] . In the case of LFP, ions migrate from the graphite anode to the iron phosphate cathode, facilitating the flow of electricity.

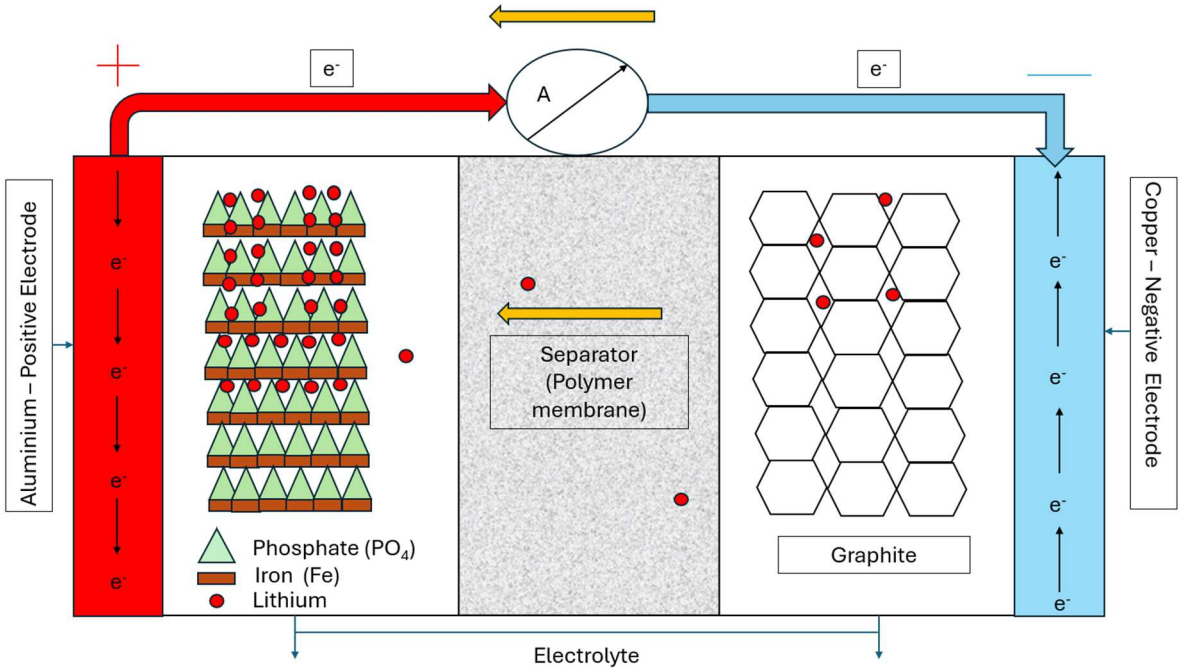


Figure 2.1.1: Schematic representation of the discharge process of a LFP battery.

Simultaneously, electrons flow from the anode to the cathode through an external circuit, generating an electric current. During the charging process, the process is inverted, with lithium ions migrating back to the anode, enabling energy storage. One complete cycle consists of both charging and discharging processes, with the lithium ions migrating in reverse directions during each phase.

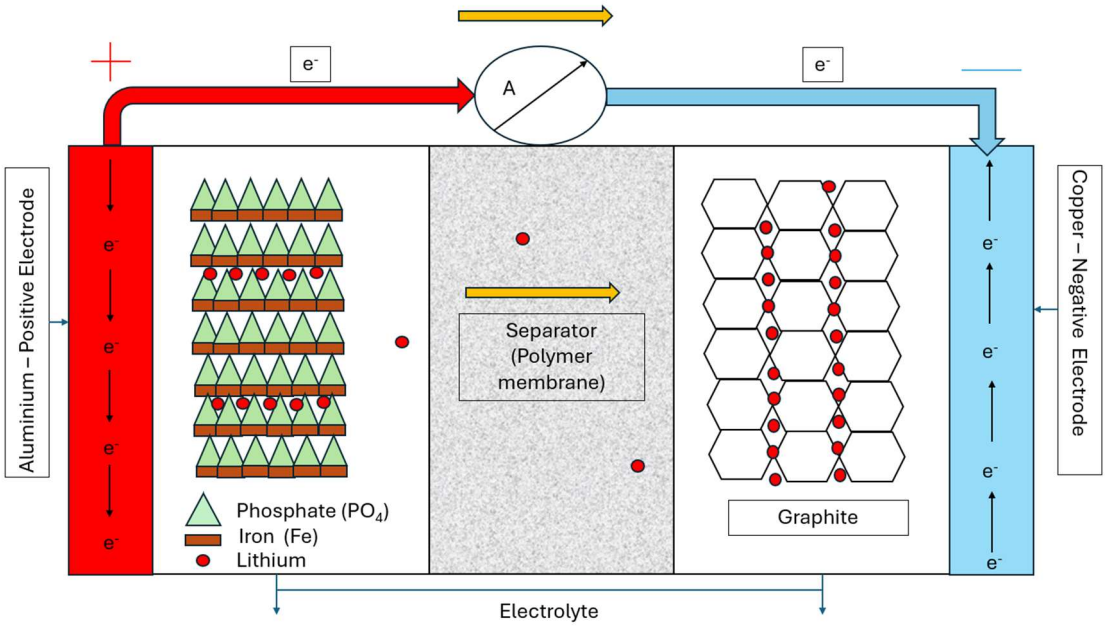


Figure 5: Schematic representation of the charge process of a LFP battery.

The batteries can be used as a single unit or several units connected in series or parallel, in a module, depending on the required capacity, voltage and application of the energy storage system. The capacity is defined as the amount of electric charge each source can supply under different charge/discharge conditions. This parameter is highly dependent on discharging current, the cut-off voltage (minimum voltage at which battery is considered fully discharged to avoid potential damage on the device), the temperature (which control is essential in this study) and the actual quantity of active materials.

## 2.2 Types of LIBs Batteries

The LIBs batteries can vary for many different types of chemistry, each of one fitted for different applications. According to literature, there are five main types of lithium ion batteries[7,14].

Table 2-1 :Comparison between different batteries chemistries. Adapted from [15]

| Chemistry | Nominal Voltage | Full Charge Voltage | Full Discharge Voltage | Minimal Voltage | Specific Energy | Charge rate | Discharge Rate | Cycle Life (Ideal) |
|---|---|---|---|---|---|---|---|---|
| Lithium Iron Phosphate (LFP) | 3.20-3.30V | 3.65V | 2.50V | 2.00V | 90-120 Wh/kg | 1C (3h) | 1C - 25C | 2000-10000 |
| Lithium Manganese Oxide (LMO) | 3.70V | 4.20V | 3.00V | 2.50V | 100-150 Wh/kg | 0.7-1C (3h) | 1C, 10C | 300-700 |
| Lithium Cobalt Oxide (LCO) | 3.60V | 4.20V | 3.00V | 2.50V | 150-200 Wh/kg | 0.7-1C (3h) | 1C (1h) | 500-1000 |
| Lithium Nickel Manganese Cobalt Oxide (NMC) | 3.60V | 4.20V | 3.00V | 2.50V | 150-220 Wh/kg | 0.7-1C (3h) | 1-2C | 1000-2000 |
| Lithium Nickel Cobalt Aluminum Oxide (NCA) | 3.60V | 4.20V | 3.00V | 2.50V | 200-260 Wh/kg | 1C | 1C | 500 |

Analyzing the table, LFP have the longest cycle life (2000-10000 cycles) compared to other chemistries, although its specific energy (90-120 Wh/kg) is the lowest. In contrast, NMC, NCA, and LCO provide higher specific energy, but their cycle life is shorter, ranging from 500 to 2000 cycles. The stability of LFP, especially at high temperatures, significantly contributes to its long lifespan making it an ideal choice for applications where durability and sustainability are prioritized over high energy density, such as in large-scale stationary storage systems, where battery mass and occupation is not a concern. [12] [13] [18]. In contrast, for compact portable applications where minimizing mass is critical, high energy density technologies such as NMC provide the most suitable solution. The characteristics of the system, combined with the battery cost (LFP as indicated in Chapter 1 being the most affordable technology worldwide), are the key factors in finding the optimal energy storage system solution.

## 2.3 Key metrics of LIBs

In the context of battery assessment, there are a set of parameters broadly referenced in the literature that relate to a battery's condition after numerous charge and discharge cycles in different conditions. These parameters are essential in determining the state and overall health of a battery, offering insights into its performance and degradation over time.

In order to cover all the concepts that are going to be discussed in this document, according to the MIT Electric Vehicle Team [19], it is necessary to understand various characteristics essential for quantifying battery degradation.

One of the indicators of battery condition is the State of Charge (SOC). According to the literature [20] , SOC is a critical factor in battery management because it reflects the battery's available

capacity, which means, the amount of charge that can still be stored or supplied. Usually, SOC is determined by accounting the battery current over a specific period (Ah). It is usually represented in percentage (0-100%).

Another important parameter for assessing LIBs is the Depth of Discharge (DOD), which indicates the percentage of the battery's capacity that is being charged/discharged in each cycle. The amount of active material that undergoes transformation during each charge and discharge cycle is directly related to the DOD, meaning higher DOD means more active material being involved in each cycle. The DOD to which a battery is subjected is crucial to consider, as different DOD levels impact the battery's lifespan [21]. It typically represents the range of SOC used in each cycle, for example a DOD of 60% could correspond to a SOC variation between 20% and 80%.

When discussing temperature variation, it is essential to consider the battery's internal resistance, which measures its opposition to current flow. This parameter is highly sensitive to temperature changes, fluctuating significantly as temperature increases or decreases. Such variations can affect the overall performance, efficiency, and lifespan of the battery, as higher internal resistance generally leads to greater energy losses and potential overheating. Moreover, the internal resistance is inversely proportional to the temperature, meaning that as temperatures decrease internal resistance increases, leading to limited ion intercalation [19].

Furthermore, the State of Health (SOH) represents the steady state status of the battery capacity (Ah) relative to its initial condition at initial stage (zero cycles). SOH serves as a key indicator of a battery's capacity and performance degradation over time, providing information about the aging process and the point at which the battery may need to be replaced. This describes the difference between a cycled battery and a new battery, representing the amount of capacity lost over time. This parameter is highly influenced by the cycling conditions, namely DOD, temperature and C-rate during the cycling period [22]

Finally, to better understand battery cycling, it is important to explore the concept of C-rate, a parameter that indicates the proportion at which a battery is charged or discharged in relation to its maximum capacity. The C-rate is expressed as a multiple of the battery's nominal capacity. For example, a value of 1C means that the full capacity is charged in one hour. Higher C-rates cause more abrupt increases and decreases in voltage, leading to faster battery degradation and reduced capacity.

## 2.4 Stressors of LIBs

Batteries ageing and degradation processes are well defined in the literature [23,24], and can be defined as a combination of multiple stress factors that contribute to the accelerated decline in performance and longevity of LIBs. These stressors can be related to various conditions, such as high or low temperatures, cycling frequency and DOD, all of which lead to a gradual deterioration of the battery's electrochemical properties, resulting in capacity loss and reduced efficiency over time.

According to [24], there are five main mechanisms of degradation that affect the performance and lifespan of LIBs:

1. Growth of the Solid Electrolyte interphase (SEI) layer: The solid electrolyte interphase layer plays an essential role for protecting the mechanical and chemical stability of batteries. Its formation occurs in two phases, first, the polarization of the negative electrode generates the decomposition of the solvent into new chemical compounds. These compounds are deposited on the anode surface, forming the SEI layer. Over the lifetime of a battery, the layer continues to grow, consuming active lithium by the new chemical compounds leading to capacity loss. This growth is influenced by temperature, charging rates, and electrolyte composition. [25,26]

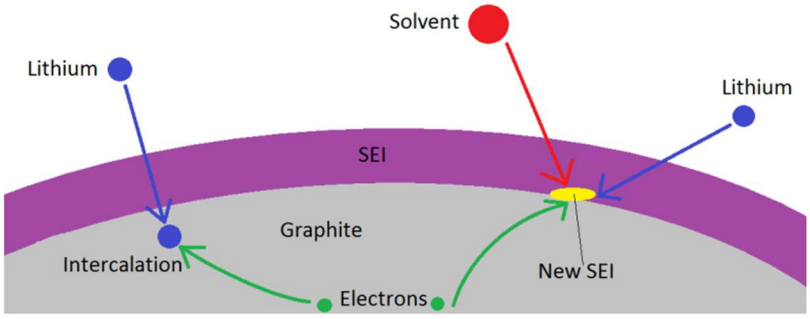

Figure 2.4.1: Representation of the growth of the Solid electrolyte interphase layer [27]

2. Lithium plating: occurs when lithium ions fail to intercalate into the electrode, specifically when the surface concentration of lithium ions in the graphite particles reaches its maximum (100% SOC), where lithium metal can instead plate onto the electrode surface. This plated lithium may be partially or fully recovered during discharge reactions through stripping. However, it is vulnerable to rapidly react with the electrolyte, resulting in the formation of the SEI. The SEI layer growth placed the plated lithium inaccessible for future stripping, being deposited with different morphology according to the charging conditions, particularly the C-rate [28]. At low C-rates (slow charging), mossy and granular lithium structures are formed. In contrast, high C-rates (fast charging) lead to the formation of dendritic structures. Dendritic growth is particularly problematic, as it can penetrate the separator, causing internal short circuits and rapid heating. This heat can melt the dendrites, disconnecting the short circuit but subsequently triggering aging mechanisms such as additional SEI formation and electrolyte decomposition [28] [29]

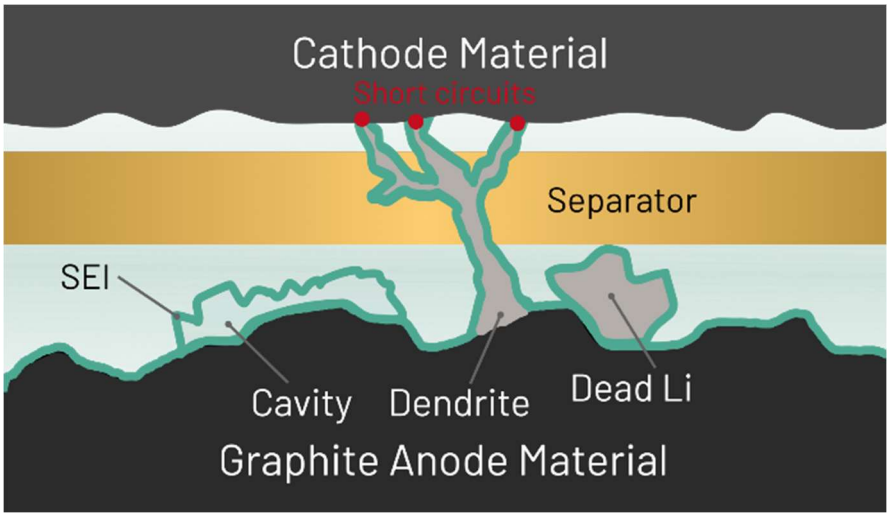

Figure 2.4.2 : Lithium plating of a battery [30]

3. Particle cracking: occurs as the electrode material (both anode and cathode) expands and contracts during the intercalation and deintercalation of lithium ions between the electrodes. This continuous deformation generates mechanical stress, which can lead to the propagation of fractures in the active particles. The resulting new surfaces can enable unwanted side reactions, such as the formation of the solid electrolyte interphase (SEI) and lithium plating. These fractures are especially common under cycling conditions that

involve constant temperature variations, in addition to the thermal stresses experienced during each phase of the cycle.

4. Loss of active material is related to the gradual reduction in the amount of material that can actively participate in the electrochemical reactions (oxidation and reduction) during the charging and discharging cycles. The loss of material could be related to unwanted side reactions or mechanical stress of the battery. As the active material decreases, the battery's capacity and overall performance is also reduced, affecting the lifespan of the battery and decreasing SOH.

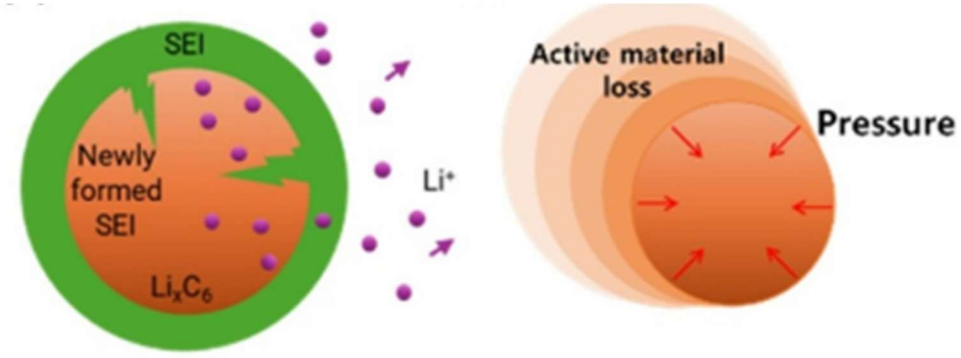


Figure 2.4.3: Schematic representation of particle cracking (left side) and loss of active material (right side)

5. Vibration: Mechanical oscillations that occur during battery operation can significantly affect the internal structure. These oscillations induce stress between the electrode materials and separators, which in turn disrupts ion migration. Additionally, vibrations can cause the graphite layers to separate and the active material in the positive electrode to fracture. This leads to intensified irreversible side reactions during cycling, ultimately resulting in a more significant loss of battery capacity [31].

## 2.5 Thermal issues

One significant limitation of LIBs is their sensitivity to temperature, which can greatly affect their performance and safety. Typically, LIBs operate reliably within a temperature range of -20 °C to 60 °C [32]. However, outside of this range, their degradation rate accelerates, enhancing the risk of critical safety issues like fire or explosion. This makes temperature control essential to maintaining the integrity and longevity of LIBs in various applications [12].

Related to temperature thermal issues, according to existing literature, there are four main problems that emphasize the need of regulation of temperature [1]:

1) Capacity/power fade: it is related to the loss of the available energy, while power fade is a decrease in the battery's competence to deliver energy in a quick way, both of which are worsened by high temperatures, and consequent low internal resistance of the battery [33].
2) Self-discharge: is the gradual loss of capacity during storage due to internal chemical reactions, which are aggravated at high temperatures. Fully charged graphite electrodes can lead to a slow release of ions through the solid electrolyte interphase (SEI), which does not completely prevent the transfer of electrons. At high temperatures, such as 60°C, the self-discharge rate increases significantly as surface compounds dissolve and the cell's electronic conductivity rises.

3) Thermal runaway: is a dangerous process where heat-generating reactions occur inside the battery, causing a rapid increase in temperature. This can happen due to mechanical damage, electrical faults, or overheating, which may lead to a short circuit when the separator between the anode and cathode fails. This parameter can be easily identified by a rapid increase in battery voltage, which in turn accelerates heating.
4) Low Temperature performance: analysis revealed that decreases in performance at lower temperatures are linked to reduced ionic conductivity, lower ionic diffusivity, and higher charge transfer resistance [11].

Understanding the impact of temperature on lithium-ion batteries (LIBs) requires examining how both low and high temperatures influence their electrochemical characteristics. Analyzing the initial stages of batteries across various lifespans (i.e., number of cycles) and range of temperatures helps prevent malfunction and highlights the importance of thermal management systems.

## 2.6 Electrochemical Impedance Spectroscopy (EIS)

Before defining Electrochemical Impedance Spectroscopy (EIS), it is important to first explain the basic concepts that form its foundation, corresponding to the literature [34]. Firstly, we need to consider that EIS measurements can be simulated to an equivalent electric circuit, which consists of passive components (inductors, capacitors, resistors) connected to distributed elements in different ways, and it is characterized by their time constant. The time constant of an electric circuit (τ) represents how quickly an electrochemical system responds to changes in the applied voltage or current at a well-defined range of frequencies.

A determined voltage or current, it is represented by a sinusoidal signal, defined by its amplitude (A) and angular frequency (ω), as described by the equation below:

$$X = A \sin(\omega t - \varphi) \qquad \text{Equation 2-1}$$

Where $Y_0$ represents the amplitude, τ, the time in seconds and ω the angular frequency. The φ represents the phase difference between two signals, most precisely, the input and output signal. Normally, these signals are represented by phasors, which also illustrate both amplitude and phase. In EIS, it is important to define the concept of a transfer function, which is the ratio between output and input signals. In impedance tests, Ohm's law defines the transfer function $Z(\omega)$, as the ratio between the voltage phasor $V$ to the current phasor $I$ at a given frequency ω.

The impedance can be defined as the total resistance in an electric circuit composed of inductors, capacitors or resistors, varying based on how these components are arranged. This transfer function has two components, one of which is the real part: the resistance R(ω), which is defined by Ohm's Law and applies to direct current (DC). Resistance represents the ratio between the voltage and the current, providing a measure of how much an electrochemical device opposes the flow of electric current

The imaginary part of the impedance is the reactance $X(\omega)$ which applies only to alternating current (AC) current, in circuits with capacitors and inductors. It defines the frequency dependent opposition to the current, creating a phase difference between voltage and current. There are two types of reactance, $X_c$, the capacitive reactance, which decreases with frequency, and $X_L$, the inductive reactance, which increases with frequency.

Electrochemical Impedance Spectroscopy (EIS) is an electrochemical technique used to evaluate the electrochemical properties of storage energy applications, such as batteries or fuel cells. In EIS tests, a small sinusoidal signal, either as a current or voltage, is applied to disturb a stable electrochemical system. The system's output evolution (observed as a sinusoidal current or voltage) is subjected to Frequency Response Analysis (FRA), which the impedance spectra is observed in different range of frequencies [34]. In contrast with many other electrochemical tests, such as cyclic voltammetry, chrono-

potentiometry or chronoamperometry, EIS analyzes the impedance of the system in a frequency domain, providing insights about the liquid-solid interface and charge transfer dynamics.

Impedance spectroscopy is commonly represented by a Nyquist plot, a graph used to visualize impedance characteristics, with the real part plotted on the x-axis and the imaginary part on the y-axis. In the case of batteries, higher frequencies appear on the left side, and low frequencies on the right. Another representation employed is the Bode plot, that consists of two separate logarithmic plots showing impedance magnitude versus frequency, and the other displaying phase against frequency [35]:

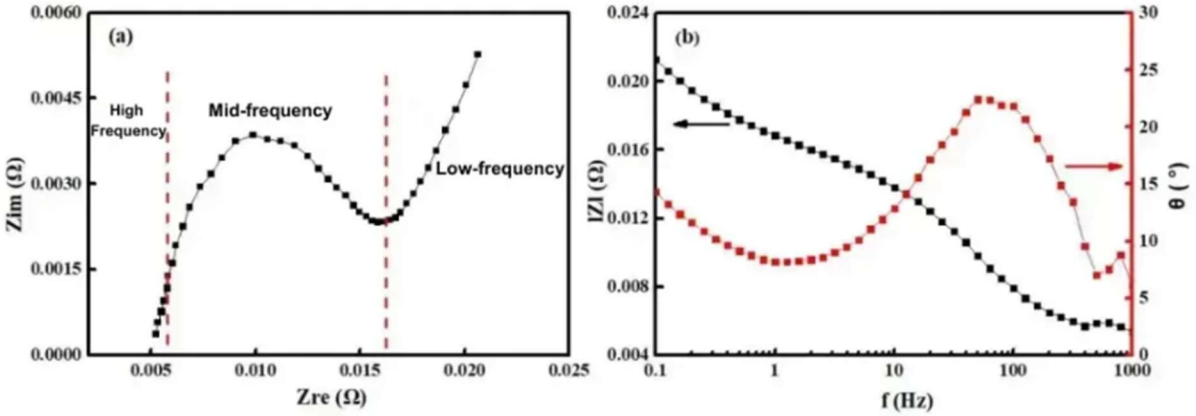


Figure 2.6.1: Schematic representation of Nyquist and Bode plots [36]

The EIS provides information about the charge transfer dynamic, where the equivalent circuit has capacitors/inductors and Warburg impedances (is the result of a diffusion process occurring at the electrode–electrolyte interface [35]). The equivalent circuit model (ECM) is the representation of the electrochemical characterization of the battery in electrical components. In lithium-ion battery electrochemical characterization, elements are introduced, like the constant phase element (CPE) and Warburg impedance (W), to address non-ideal capacitive behavior and ion diffusion dynamics. The CPE accounts for electrode surface irregularities, while the Warburg impedance models frequency-dependent diffusion effects, which is highly affected by the temperature [37].

In the literature, there exist several circuits models that are used to represent the behavior of electrochemical systems, which are often represented by 1$^{st}$ order and 2$^{nd}$ order equivalent circuits. The equivalent circuit model represents a more complex framework frequently applied in lithium-ion battery (LIB) systems, offering a detailed representation of one of the two electrodes in a galvanic cell or simple battery. The $R_{ohmic}$ represents the bulk resistance (resistance of the electrolyte solution, related to ionic conductivity of the electrolyte) It is largely independent of temperature under normal operating conditions, as it is determined by the intrinsic properties of the battery materials. R1 characterizes the resistance in the SEI layer, $CP_{SEI}$ represents the constant phase element that embodies the SEI layer, R2 emphasizes the charge transfer resistance (related to the electrochemical reactions occurring at the electrode/electrolyte interface) and CP2 the constant phase element of the electrode (models the non-ideal capacitive behavior of the electrode), as illustrated in the figure below.

a)

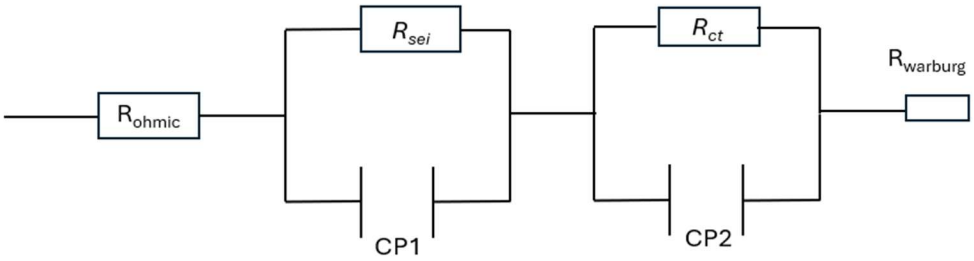


b)

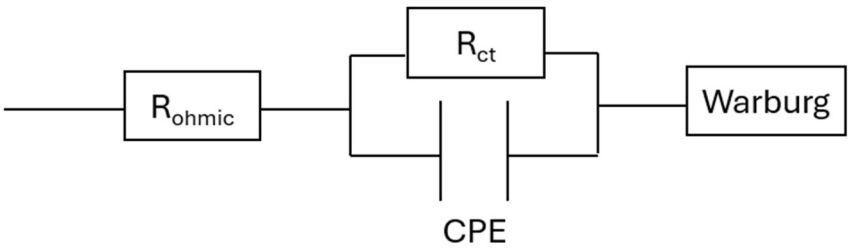


Figure 2.6.2: Equivalents circuits used to represent the behaviour on LFP electrochemical characteristics, a) represents a 2nd order circuit and b) represents a 1st order circuit.

The first RC (R1/CP1) couple represents the first semiarch in a Nyquist plot, which typically corresponds to the high-frequency region of an electrochemical impedance spectra. The second RC (R2/CP2) couple represents the second semiarch of the Nyquist plot, corresponding to the low-frequency section [38].

While it serves as a foundational tool for understanding basic cell behavior, the configuration of an equivalent circuit model can vary widely. These variations depend on factors such as the electrode materials, cell construction, and specific conditions like storage and cycling. This flexibility allows the model to be adapted for different applications and performance characteristics.

EIS applies a small AC potential at a fixed DC bias to ensure system stability, as most electrochemical reactions are not fully reversible when the potential is reversed. Using a high amplitude AC signal could destabilize and distort the system. Therefore, maintaining a constant DC bias throughout the measurement is essential to minimize the impact of the perturbation on the system's stability [39].

By integrating the concepts of Equivalent Circuit Models (ECMs) and the graphical representation of electrochemical systems, the correlation between model parameters and experimental impedance measurements becomes evident, as the figure below shows:

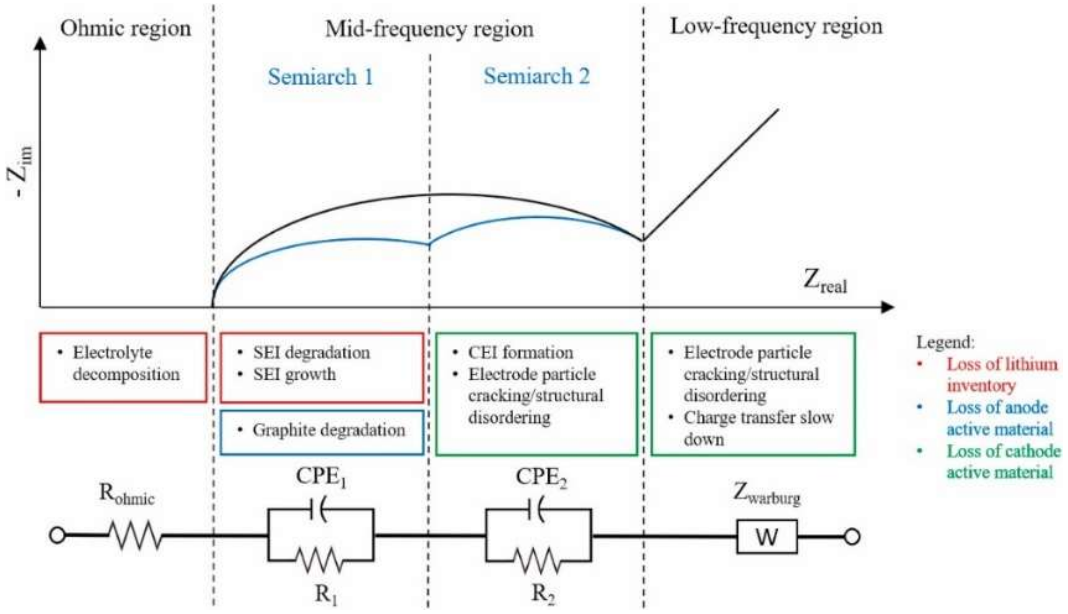


Figure 2.6.3: Integration of Equivalent Circuit Models and Nyquist plot [40].

The figure is divided into four sections describing different processes. The first section represents the start of ion conduction processes, following the inductive behavior at high frequencies. The second section corresponds to the SEI layer (first RC couple), which impacts ion transfer at the interface and appears in the high-to-mid frequency region. The third section represents charge transfer processes at the electrode/electrolyte interface, occurring in the mid-frequency range, where the Cathode Electrolyte Formation (CEI) occurs. Finally, the last section illustrates the Warburg impedance, related to the diffusion of lithium ions in the solid and liquid phases. The black line represents the theoretical impedance response of the system, while the blue line indicates the observed response, considering factors such as lithium inventory loss, SEI growth, and other degradation effects [41].

In several cases, the two semicircles are not observable, leading to a 1st order circuit characterization as the circuit below shows where the two semicircles are integrated into one R/CPE couple, with the sum of the resistance represented by Rct~~., and highly dependent of operating temperature.~~

## 2.7 Temperature and ageing effects in EIS tests

To evaluate the effect of cycling on LIB degradation, EIS tests are performed at various SOC levels, ageing stages, and temperatures to efficiently electrochemically characterize the batteries [40] [41]. The effects of SOC and number of cycles are crucial in understanding how the internal resistance and electrochemical processes of lithium-ion batteries evolve with cycling, as the figure below shows.

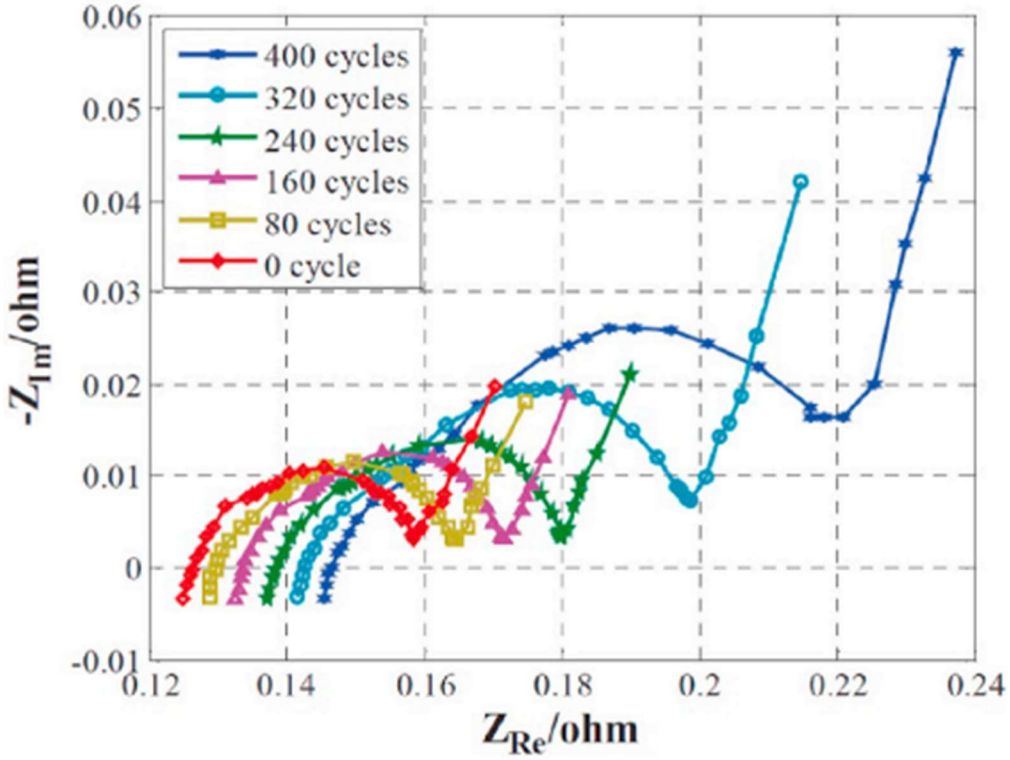


Figure 2.7.1: Cycling effects on the EIS spectra [42]

Initially, a shift to the right is observed in the high-frequency region, indicating an increase in electrolyte resistance. This increase is attributed to the growth of the SEI layer on the electrode surface and the loss of active material, both of which are proportional to the number of cycles. Subsequently, an expansion in the semicircle diameter is observed with cycling, reflecting an increase in charge transfer resistance or double-layer capacitance, influenced by the degradation of the electrode material. Finally, no significant changes are observed in the angle of the Warburg impedance with cycling [42].

Controlling temperature in electrochemical characterization is critical for understanding and improving the performance of lithium-ion batteries. According to Meddings et al [42] high temperatures generally result in lower impedances, which is attributed to a decrease in charge transfer resistance due to faster electrochemical reactions at the electrode-electrolyte interface. Additionally, increased electrolyte conductivity at higher temperatures contributes to lower electrolyte resistance. These effects lead to a reduction in the overall impedance of the battery, which can be observed as a shift of the impedance spectrum towards the origin in a Nyquist plot.

At low temperatures, the electrochemical processes are slower, leading to higher impedance and reduced efficiency. Measuring the EIS spectra allows for a separation of charge transfer impedance from other impedance features, such as high frequency [10]. The figure below shows the impedance spectra at different temperatures.

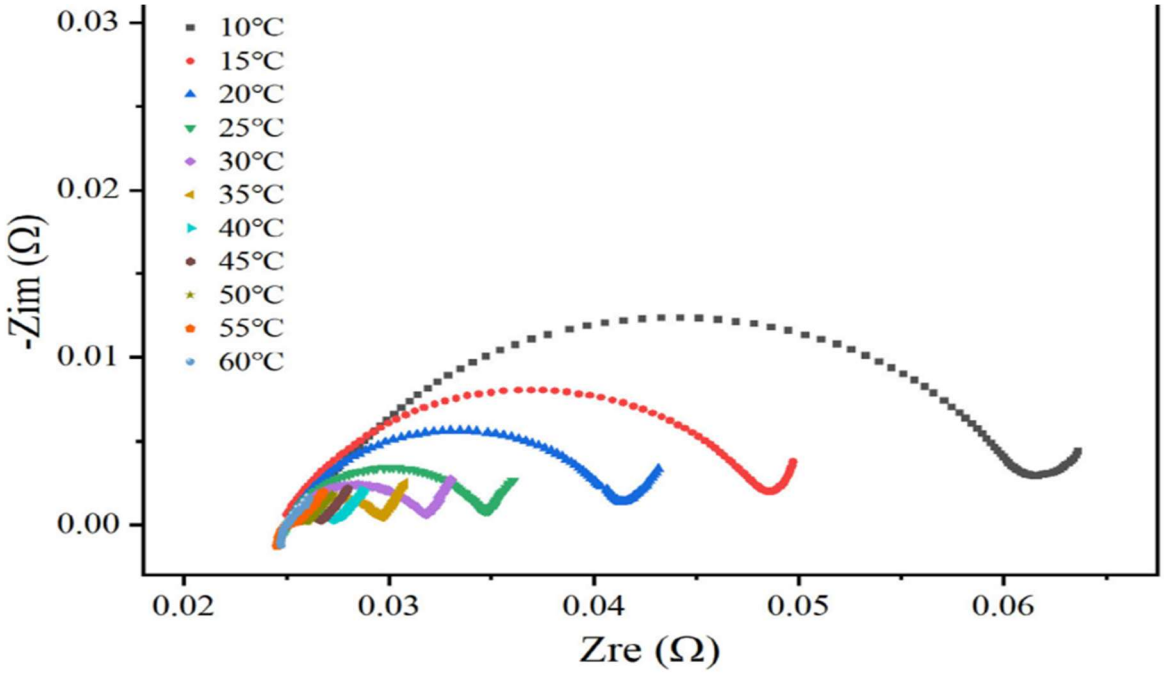


Figure 2.7.2: EIS spectra at different temperatures [10]

As observed in the graph, an increase in temperature corresponds to a reduction in the diameter of the semicircle, indicating a decrease in the charge transfer resistance. This suggests an improvement in ionic conductivity or charge transfer, that are thermally activated processes. The Warburg impedance, sometimes represented by the inverse property admittance, is highly influenced by temperature, with high impedance at low temperatures (indicating low ion diffusion) and low impedance at higher temperatures (indicating high ion diffusion), showing the same behavior as the charge transfer impedance (related to the length of the semicircle) [43].

The results of these studies highlight the importance of conducting electrochemical characterization across a range of controlled temperatures, as variations in impedance are observed, with both capacitive and resistive features shifting. These shifts are linked to temperature-induced changes in ionic transport and the interactions at the electrode-electrolyte interface.

In relation to the research question, performing EIS at different temperatures should allow for a greater range of data to be acquired, which will enhance the interpretation of the battery's degradation over its lifespan, specifically in terms of the impedance spectra changes observed with increasing cycle number under controlled temperatures. Thus, controlling temperature during electrochemical characterization is crucial. For this reason, it is imperative to develop a laboratory setup to regulate temperature during EIS characterization, ensuring that these temperature-dependent variations are properly captured and analyzed [10,43].

# 3 Methods

To address the proposed research questions, the study will be structured around four main processes. First, the cells to be studied are defined based on the technical specifications provided by the supplier. Second, the eight initial batteries will undergo cycling, during which several charges and discharges will be performed, allowing to evaluate the capacity of the battery at different stages. Third, impedance tests will be done, considering the implementation of an experimental setup, that includes the temperature control using a cryostat, and the performing of electrochemical impedance tests. Finally, after the measurements are obtained, the data will be fitted using ECM, to evaluate the evolution of parameters trough temperature changes and batteries lifespan.

## 3.1 Technical specifications of the battery

8 *ENERpower* 10430 (AAA) LFP 3.2V 200 mAh (Figure A.2.1) batteries were used for this study. The battery, according to the supplier, operate between 2.5 V (Low discharge voltage) and 3.6 (high charge voltage). In standard conditions it support a charging current of 0.1 A, and discharge rate of 1C (200 mA).

The internal resistance of the battery is below 120 mΩ, and the cell dimensions are 10 mm in diameter and 43 mm in length. This cell doesn't present a protection circuit, and their cycle life depend on the DOD, being 1500 cycles at 100%, 3000 cycles at 80%, and 6000 cycles at 60% DOD.

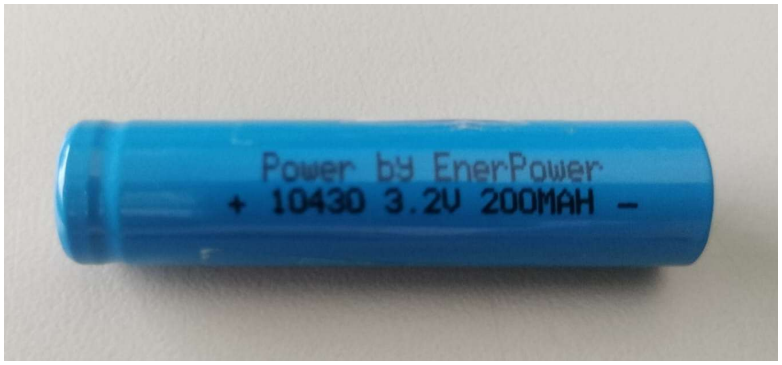


Figure 3.1.2: *ENER power* 10430 (AAA) LFP 3.2V 200 mAh

The selection of the battery size and capacity was based on previous work conducted in a master's thesis [44] , while the number of batteries was determined by the available cycling channels. The cycling device and procedure are described in a later section.

## 3.2 Cycling processes

To evaluate the evolution of the electrochemical characteristics of LFP batteries under different lifespans, cycling was performed under different protocols. According to the battery technical specifications (Figure A.2.1), we first introduced a standard cycle, where the charge process was carried out at 0.5 C (maximum charging current in the specifications) and discharge process performed at 1 C (equal to the continuous load in the specifications).

Each phase of the cycling process can be performed with independent constant-current and constant-voltage source, which can be programmed and controlled via computer software. In this case, the charge process is performed at constant current - constant voltage (CC_CV), where a constant current of 100 mA is applied, once the maximum voltage (3.6) is reached, the charger holds the constant voltage at the defined cutoff voltage of 3.6 V where the current gradually reduces.

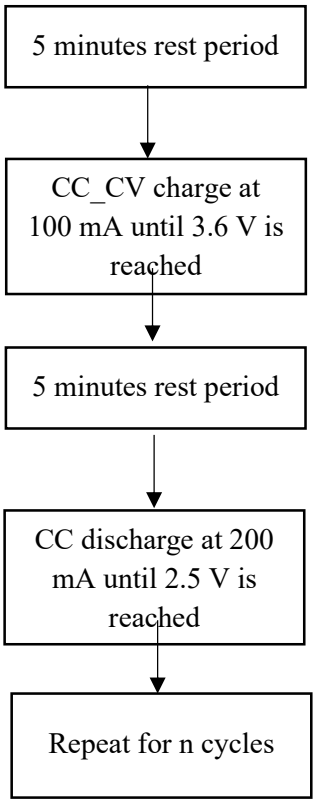


Figure 3.2.1: Standard Cycling Protocol

To assess the initial conditions of the batteries, 10 standard cycles were performed on the eight LFP batteries to determine their initial capacity. This will serve as a reference for analysing capacity loss and state of health over time. In this process, it is mandatory to set the limits specified in the battery specifications, particularly, the low and high protection voltages. The cycling process stops whenever one of these limits (2.5V or 3.6V) is reached, and the channel enters protection mode, indicating potential battery damage.

All the cycles were executed using an MTI BST 8-Channel Battery Analyzer. Each channel operates independently with constant-current and constant-voltage control, supporting a maximum of 5V and 3000mA. Each channel can execute independent protocols and retain a history of charge/discharge process data of every battery, voltage and capacity data were recorded every 30 seconds. The number of steps depends on whether the high or low voltage limit is reached. The setup of the battery analyzer is presented below.

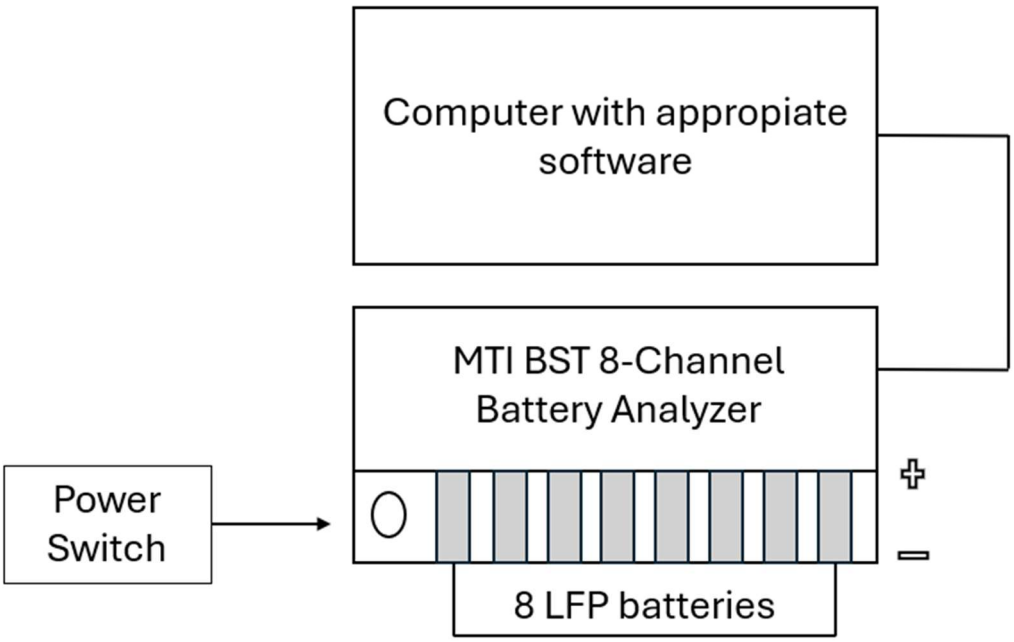


Figure 3.2.2: BTS Cycling Setup

Additionally, after each FRA measurement, the batteries are charged using the CC–CV protocol with a constant current of 100 mA before the next measurement is performed, in order to evaluate the electrochemical behavior of the battery during discharge.

## 3.3 Impedance Tests (EIS)

To electrochemically characterize the batteries across different lifespans and temperatures, electrochemical impedance (FRA) measurements were performed at various SOC levels, first at full capacity, then in 10% SOC intervals during battery discharge. As in the cycling protocols, the voltage was limited to the LFP cut-off value to prevent any damage to the battery.

The *PGSTAT302N Potentiostat/Galvanostat* by Metrohm Autolab allows for either *Galvanostatic* or *Potentiostatic* analysis. In this case, since LIB batteries have low internal impedance, the *Galvanostatic* technique is more suitable, whereas the *Potentiostatic* technique is preferable for high-impedance systems, where small voltage changes lead to small current responses. In low-impedance systems, even a little voltage change can cause an unstable current response. [45, 46]

The EIS measurements are performed by FRA discharge protocol that involves applying a current equal to the nominal capacity (200 mAh) for 6 minutes to discharge the battery by 10% of its state of charge (SOC). Following this discharge step, FRA measurement is performed across 45 different frequencies. This process is repeated at a fixed temperature until 10 discharge FRA protocols are performed, when the battery is discharged by 200mAh, approximately the full capacity of each battery. It is noted that the battery never reaches 0% of capacity, this is due to the standardization of the FRA protocols to the nominal labelled capacity of each LFP.

To accelerate the process, all the steps i.e., the initial FRA measurement and the subsequent 10 discharge FRA, are compiled into a schedule, allowing for sequential execution of all measurements until the battery nominally reaches 0%. In this case, the discharge is always limited by the lower voltage limit previously established.

The FRA measurement is performed between 10 kHz and 0.1 Hz, across 45 different frequencies, where a small current, limited to 0.02 A, is applied to observe the impedance response of the system. After the initial FRA measurement, the process shown below is executed, where a negative current is applied (to discharge the battery) for a period of six minutes (1/10 of an hour) in order to discharge 10% of the initial nominal capacity, followed by the process indicated in figure below.

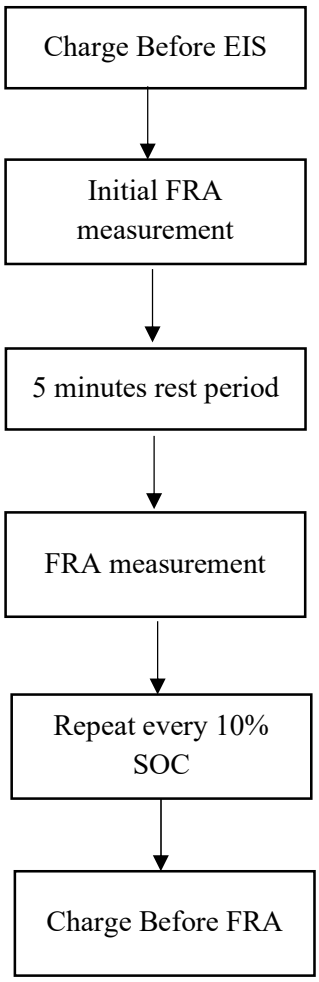


Figure 3.3.1: FRA Discharge Measurement Protocol

### 3.3.1 Temperature control

As the research question and objectives indicate, a significant portion of the experimental work was dedicated to developing a system that allows temperature control of the battery during EIS measurements. The experimental setup consists of a 700 mL plastic cylinder with a hermetic lid, including two holes for the *Galvanostatic* connections and another two for the thermocouple. Inside the cylinder, an AAA battery holder is secured, with wires soldered to the positive and negative terminals to enable EIS measurements.

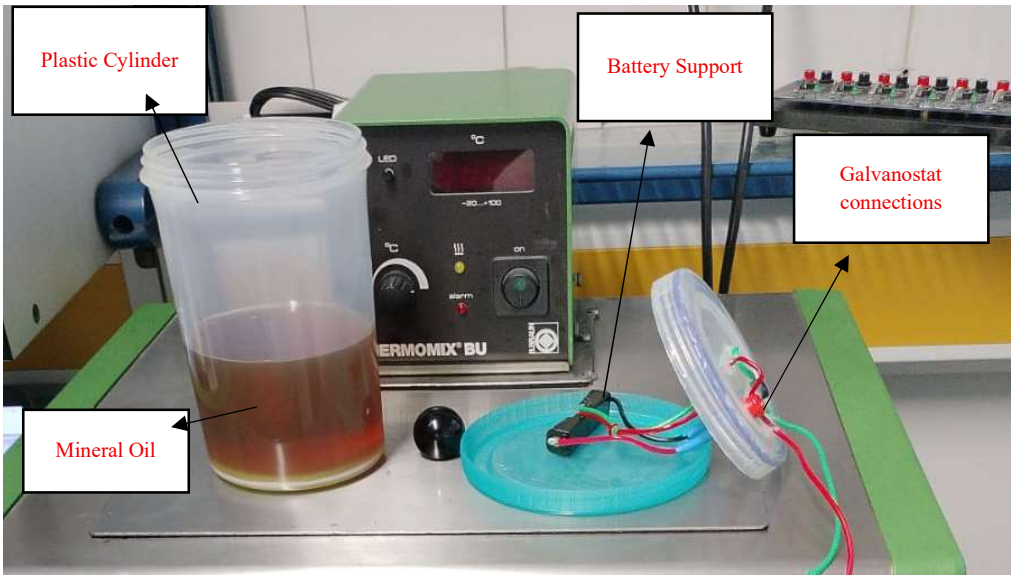


Figure 3.3.2: Plastic cylinder with lift-integrated connections

The system is placed inside a B. Braun Frigomix FX-U refrigerated water bath, which maintains a stable temperature bath using water and antifreeze (glycol) mixture. Meanwhile, to prevent water electrolysis and ensure effective heat transfer to the battery, the cylinder is filled with a volume between 300-400 ml of mineral oil (15W40), allowing to maintain and measure the battery impedance at different temperatures without affecting its electronic behaviour, as the oil is a non-electrical conductor.

The experimental setup is equipped with two sensors: one inside the antifreeze glycol and the other inside the cylinder (thermocouple), allowing adjustment of the bath temperature thought the thermocouple, to achieve the desired oil temperature (real battery temperature). The bath is kept in constant agitation to ensure a uniform temperature throughout its volume.

After setting the temperature, there is no significant difference between the temperature of the oil bath and that of the water bath. In the image above, the top part of the water bath displays the temperature, which typically fluctuates between 0.1 and 0.2 ºC during each FRA measurement but stabilizes during the rest periods of the measurement.

The experimental setup for temperature-controlled LFP battery testing is illustrated in Figure 3.3.3. All system components and their interconnections are shown, including the thermostat-regulated water bath, mineral oil chamber, thermocouple, battery holder, and potentiostat/galvanostat. This configuration ensures stable temperature conditions and accurate electrochemical measurements throughout the tests.

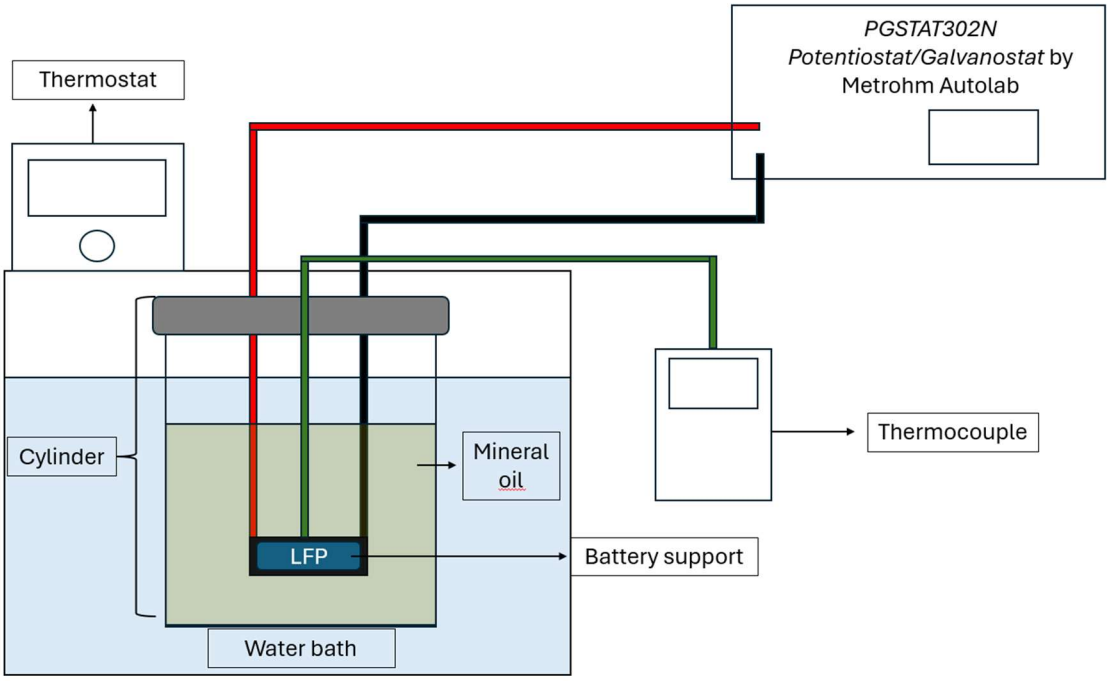


Figure 3.3.3: Schematic Diagram of the Temperature-Controlled LFP Battery Testing System

### 3.3.2 FRA Measurements

After setting the temperature of the water bath and ensuring that the thermocouple inside the battery indicates the desired temperature, the FRA measurements are performed. Once one impedance spectra at a specific temperature is measured, the battery is charged in the battery analyser, while another one is electrochemically analysed, ensuring a dynamic system where cycling and FRA measurements are continuous and uninterrupted.

During each measurement, it is ensured that the cut-off voltage is not reached, which is controlled by the software. To prevent charge destabilization and accumulative temperature modifications during testing, resting periods are introduced between cycles. To allow continuous measurements, the eight batteries are tested sequentially at a defined temperature. Once all batteries have been tested, the temperature is adjusted, and the process is repeated at the new set point. Measurements are conducted at 0 ºC, 5 ºC, 10 ºC, 15 ºC, and 20 ºC, the last one simulating ambient temperature, to understand LFP performance from low to ambient temperatures.

The data gathering process is illustrated in the figure below. Initially, the system is static, with no cycling during FRA measurements, ensuring all batteries are at the same stage of life. After this initial condition (10 cycles) and the first batch of cycled batteries, the system becomes dynamic. At this stage, batteries undergo different numbers of cycles, allowing for more efficient and optimized sampling.

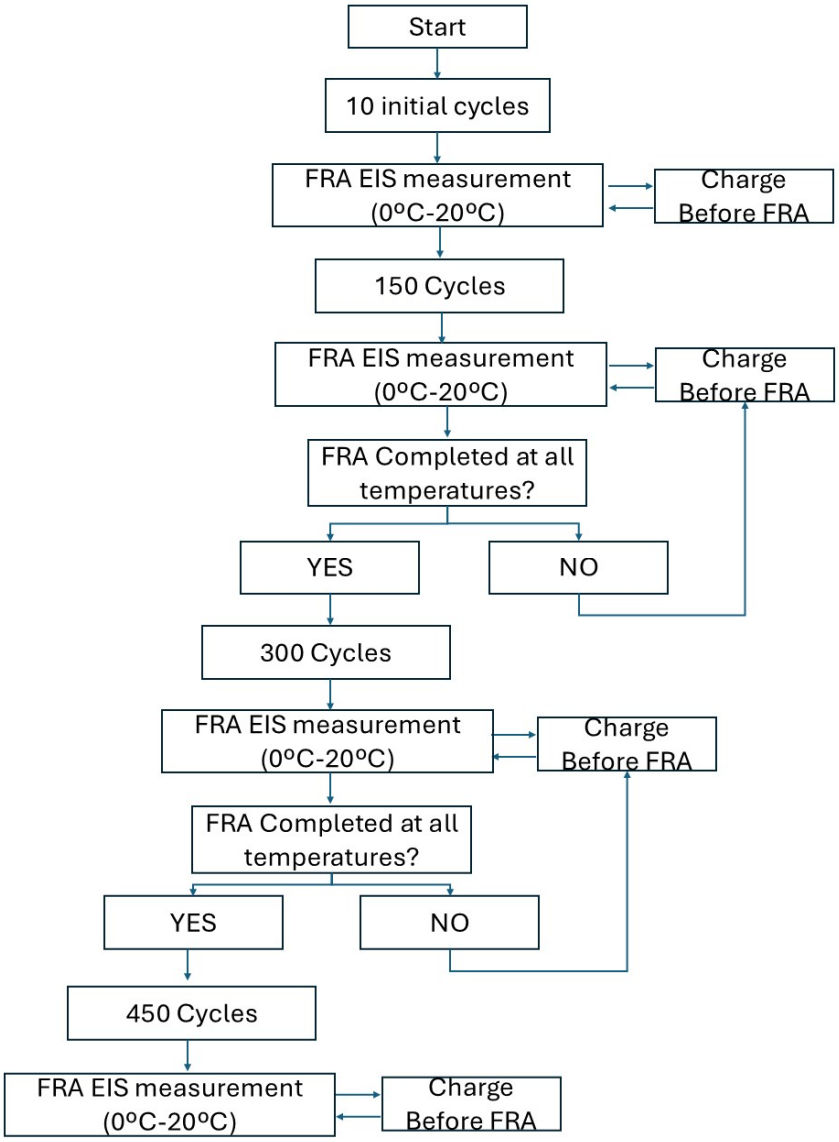


Figure 3.3.4: EIS Data gathering process

The spectra are obtained for each SOC percentage, totalling 11 spectra per battery at different stages of life and temperature. All data are labelled with the corresponding percentage and compiled for each battery.

## 3.4 Data-driven fitting of the ECM

The impedance spectra obtained in 3.3, is fitted with equivalent circuits depending on the electrochemical characteristics that are going to be studied, and also, the type of technology of the battery. In this research, will be studied mainly one ECM, that strictly depends on the number of semicircles observed in each spectra.

Based on these spectra, a first order equivalent circuit is fitted, chosen according to the number of semicircles observed and the battery's electrochemical characteristics. This circuit, derived from the semicircle fitting using Nova Software, enables the determination of the series resistance in the ohmic region and the total resistance in the high and mid frequency regions. At very low frequencies, the

Warburg impedance models lithium ion diffusion, while an inductor represents the initial inductive behavior of the wires connected to the LFP during the FRA measurement [41].

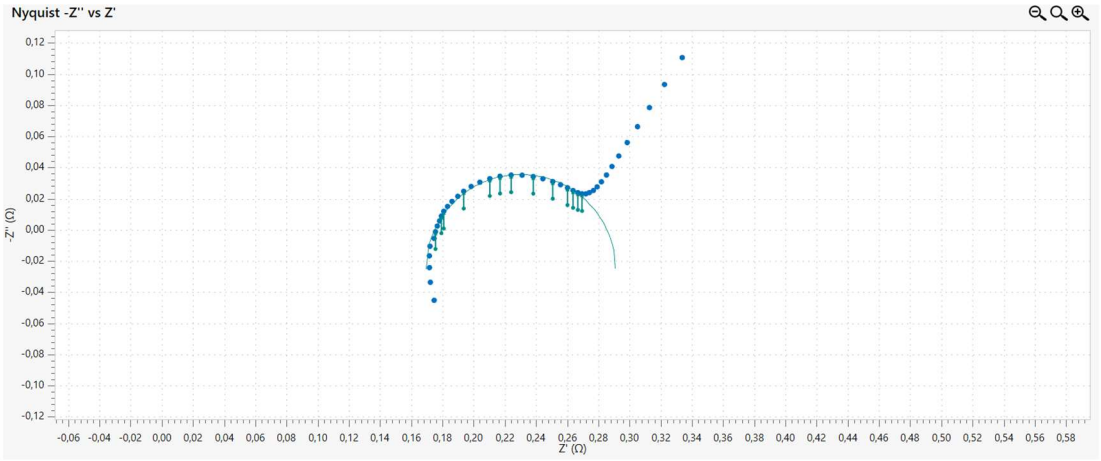


Figure 3.4.1: Example of Electrochemical circle fitting in the NOVA software

The figure above illustrates the electrochemical circuit fitting process using a first-order circuit (a single R/CPE couple) in the NOVA software. According to the software specifications, initial values are iteratively refined until the squared error ($X^2$) reaches a value equal to or lower than 0.01, indicating convergence between the model and the acquired data. After achieving the convergence of the data and minimizing the squared error, the final fitted equivalent circuit is obtained, as shown in the example above. The circle is obtained selecting the points that compose the high and mid frequency region to simulate the shape of the measured impedance spectra, i.e the semicircle.

After completing the electrochemical circle fitting, an equivalent circuit is generated that partially represents the circuit characteristic, missing the induction effect related to the wires, and the Warburg impedance related to the ion diffusion at lower frequencies. An example of an electrical circuit is represented below.


Figure 3.4.2: Example of a final equivalent circuit obtained with the ECM fitting

Alongside the electrical circuit, a new dataset of fitted impedance spectra is obtained, containing the total percentage error at each point during the iteration across all 45 different frequencies. If the values follow the trends reported in the literature, i.e. the series resistance corresponds to the intersection on the real axis and the charge transfer resistance is approximately the diameter of the semicircle, the fitting is considered valid. In the next chapter, we will analyze the experimental data together with the fitting results to evaluate the ECM parameters obtained, more specifically the resistance and Warburg obtained.

# 4 Results and Discussion

After obtaining all the results, the data analysis is going to be focused on studying the evolution of battery capacity over time, and more incisively on the study of all impedance spectra alongside circuit parameters of each battery as a unit, to obtain an average behaviour of the LFP, identifying outliers and trends with the variables of the study, i.e. SOC, temperature, and number of cycles.

## 4.1 Capacity evolution

As described in the cycling protocols, to assess battery degradation over time, the initial available capacity of the batteries was obtained through the discharge curve of each one, as the graphic below shows:

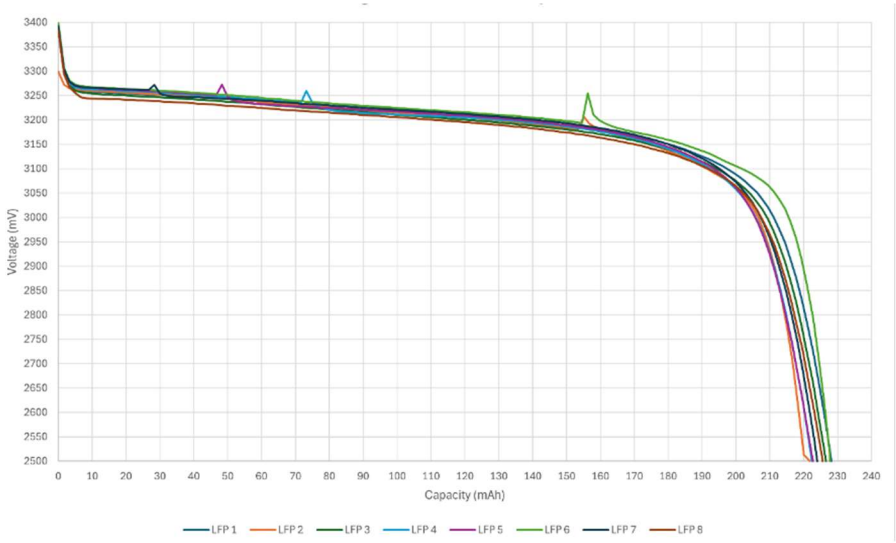


Figure 4.1.1: Discharge curve of all 8 LFP batteries at 10 cycles.

By the figure above, it is noted that there is a drop in voltage at the beginning, from 3400 to 3300 mV, due to the battery's internal resistance when a negative current is initially applied [47]. From 3300 mV onward, there is an almost linear discharge with a slight voltage drop but an increase in discharged capacity, showing that LFP technology has a stable voltage plateau (around 3200 mV) [48, 49]. Nearby 3100–3000 mV, there is a big downfall of the voltage with a very slight increase in capacity, where little active material remains available for deintercalation; in this region, an abrupt voltage drop occurs with only a small increase in capacity, as little active material is left for deintercalation. This curve behaviour is consistent with the literature, clearly showing both the initial and final voltage drops [50,51]. The initial capacity of the batteries is displayed in the table below:

Table 4-1: Initial Capacity of the eight LFP batteries tested

| Battery | LFP 1 | LFP 2 | LFP 3 | LFP 4 | LFP 5 | LFP 6 | LFP 7 | LFP 8 | Average | Standard deviation |
|---|---|---|---|---|---|---|---|---|---|---|
| Capacity (mAh) | 228.2 | 221.8 | 226.6 | 222.5 | 222.7 | 227.8 | 224.1 | 225.7 | 224.93 | 2.34 |

Experimental measurements showed that the actual discharge capacity is higher than the nominal capacity (200 mAh). According to the literature, this can be related to the cell weight (amount of active material at initial stage) and the initial internal resistance of each cell and safety margin to ensure the lifespan proposed by the manufacturer [52].

The initial capacity of each LFP battery changed during different cycling periods. Figure 4.1.2 shows the capacity evolution of the batteries at each impedance measurement stage, namely at 10, 150, 300, and 450 cycles.

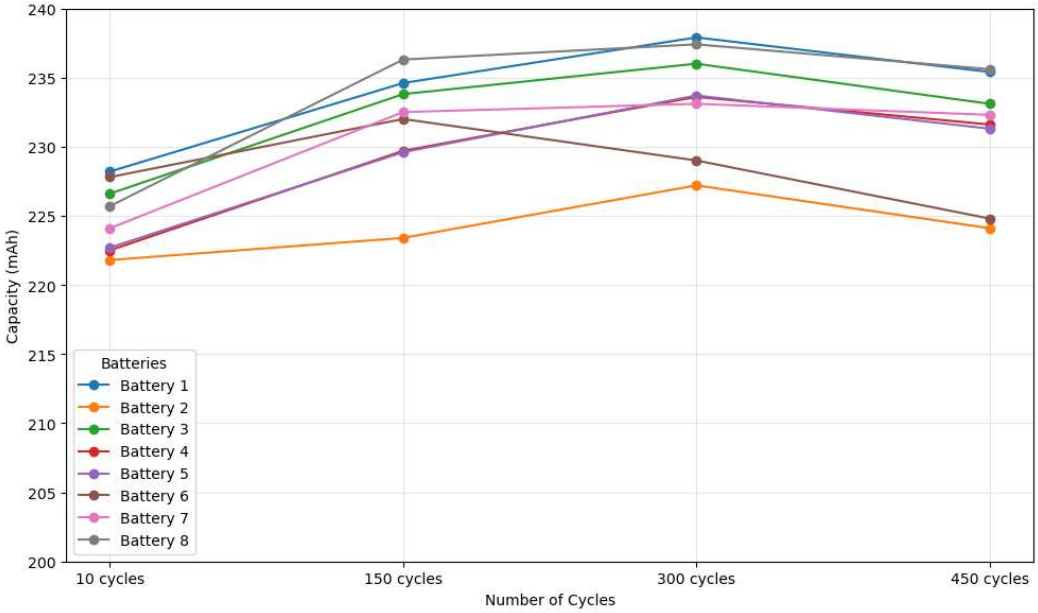


Figure 4.1.2: Capacity evolution of all 8 LFP during different lifespans (number of cycles).

It is evident that a capacity increase occurred in all 8 LFP batteries after the initial cycling stage (10 cycles). This behaviour has been well defined in the literature. Guo et al [53], reviewed previous works [54,55,56,57] in the field that applied non-destructive test, such as EIS and charge/discharge cycling under ideal conditions, allowing the observation of the cell's intrinsic electrochemical behaviour without external interference.

After 150 cycles there is a stabilization of battery capacity in almost all batteries, except from the case of battery 2 and 6, where a downfall in capacity is observed. Gyenes et al [56], concluded that some lithium ions are deposited in the overhang region of the anode during the initial stage, and are later deintercalated during cycling, increasing the available capacity of the battery, justifying the observed increase in capacity. As reported in literature [53], this phenomenon is typical of cycling with larger DOD or environment temperature variation, as cycling started in late January and lasted until September, during which a temperature increase occurred over time.

## 4.2 Impedance Spectra

The impedance spectra (EIS) collected after the initial 10 cycles shows the influence of temperature on impedance, as evidenced by the increasing diameter of the RC semicircle with lower temperature. It is important to note that only one semicircle is observed across all temperatures and battery types, indicating that the time scales of the charge transfer process and lithium-ion transport through the SEI layer are very similar. As a result, these contributions cannot be reliably separated through fitting with distinct initial parameters. Therefore, in this work, they are treated as a single RC element when graphical separation of the two semicircles is not feasible. This approach is consistent with methodologies used by other authors when the semicircles are overlaid. [53,54]

To evaluate the quality of the sample and its significance, the spectra of all eight batteries were compared at a fixed SOC value of 60% to note the differences and identify possible outliers and trends. The spectra of all batteries are plotted in the figure below at 10 cycles (initial stage). The impedance

spectra that will be considered for further analysis will be an average of all the batteries that behave similarly, based on the analysis of the Nyquist plots presented in Figure 4.2.1.

It is noted that there is more similarity between batteries when increasing temperature, with the spectra becoming more uniform among them. Batteries 3 and 8, represented in green and light blue respectively, present a larger semicircle diameter corresponding to higher charge transfer resistance at all temperatures. These batteries will be treated as outliers in the rest of the analysis. In further analysis, circuit-fitted parameters will be examined individually, allowing a better understanding of the differences between the outlier batteries and the average ones.

Furthermore, as expected since the batteries are made of the same materials (same anode and cathode), the series resistance (intersection on the real axis) is similar when examining the graph. This property remains almost constant across all temperatures, indicating that it is not a temperature-dependent parameter, as it mainly depends on the intrinsic resistivity of the material and the geometry of the cell [58]. The remaining visualized and identified parameters are strongly affected by temperature and battery ageing, and the analysis will be based on these variations. In all eight batteries exist an induction effect in the spectra, directly to the wires connected from the equipment to the battery support inside the cylinder, and it's noted by negative values of the reactance in the Nyquist plot.

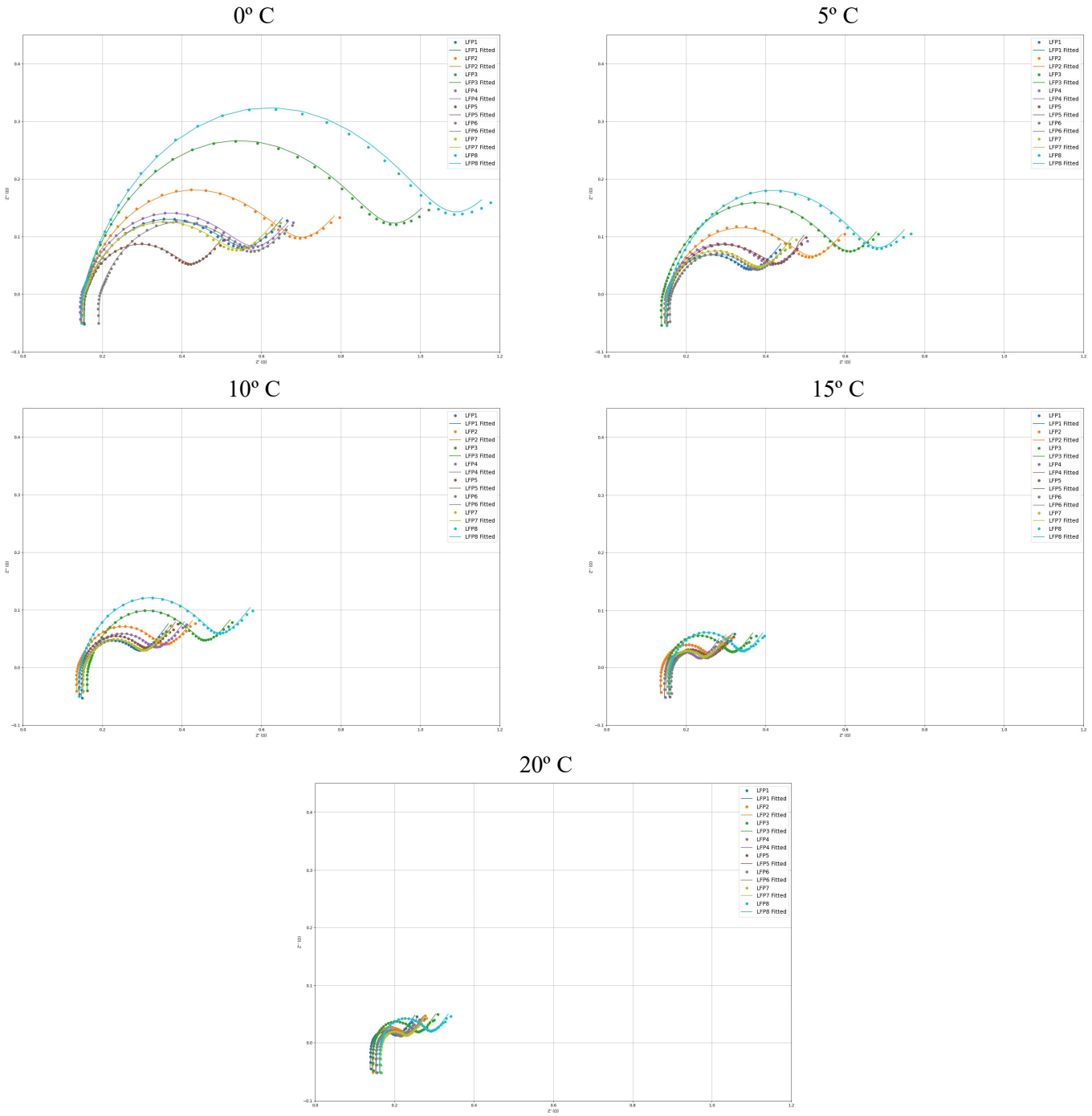


Figure 4.2.1: Impedance spectra of all 8 LFP batteries at 60% SOC at different temperatures (0º,5º,10,15º and 20º) in their initial stage.

In the spectra above, the fitted data are also shown (fitting parameters in the Appendix, Figure A.1.12), closely following the experimental data except in the Warburg region, that is, the part associated with the diffusion of lithium ions within the electrode and electrolyte interface. This region appears as an inclined tail after the semicircle, typically observed at low frequencies, where the response is dominated by the diffusion of lithium ions. It reflects the resistance to ion transport during intercalation and deintercalation processes and is strongly influenced by temperature, since higher temperatures enhance ion mobility and modify the diffusion behaviour. It is also observed that each battery behaves

differently from the others, but the increase in the semicircle that represents the rise in charge transfer resistance remains constant. The series resistance shows slight variations among all batteries.

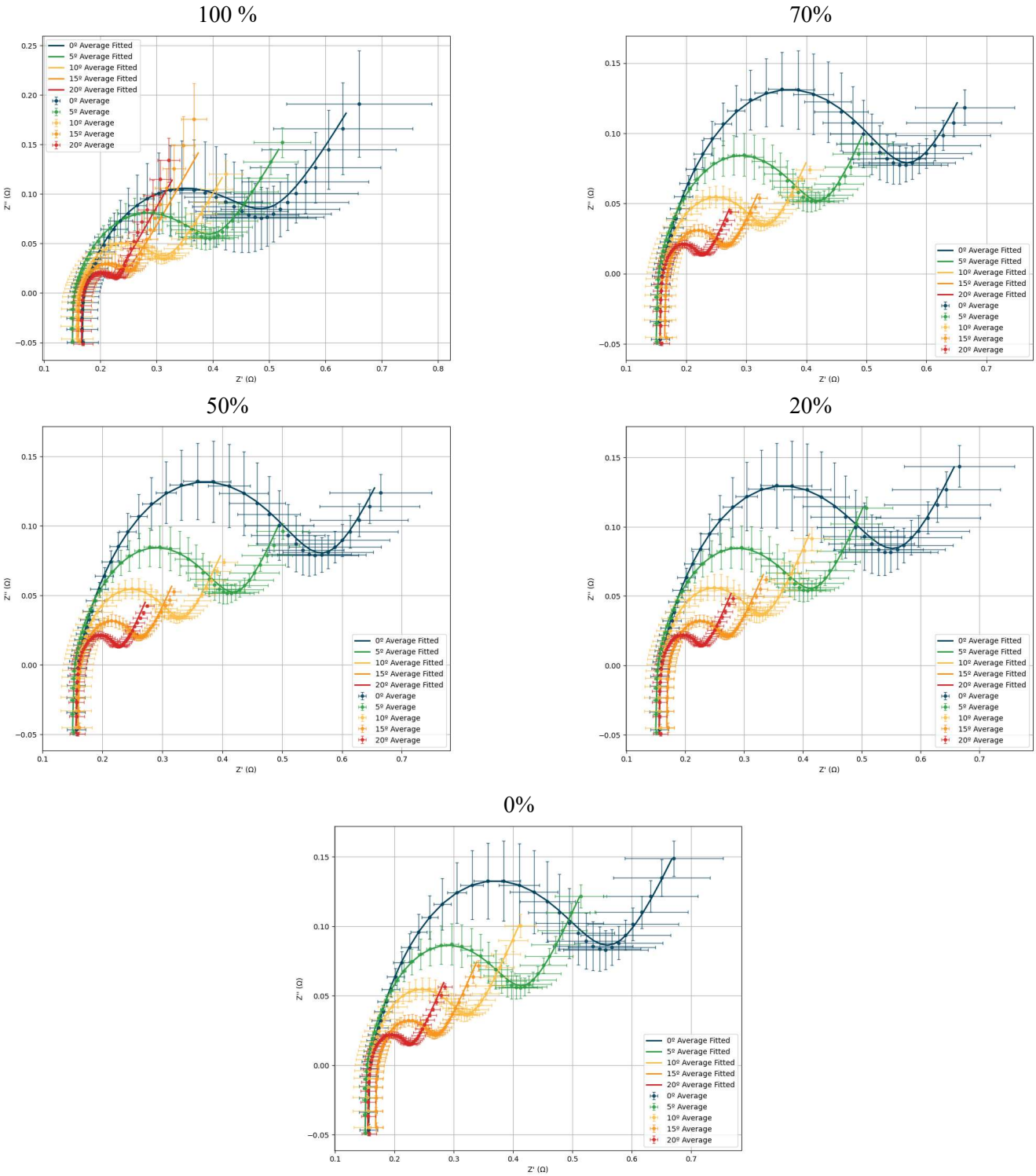


Figure 4.2.2: Average Impedance spectra at different SOC's and different temperatures (0º,5º,10,15º and 20º) in their initial stage (10 cycles).

The average spectra obtained from the batteries are compared across different temperatures and SOCs. As noted in Figure 4.2.2, there is a shift in the second semicircle of the impedance spectra to the

left with increasing temperatures, showing a significant difference between near ambient temperatures (20º, 15º, and 10º) and those at lower temperatures (0º and 5º), indicating higher opposition to current flow at lower temperatures.The fitting at 100% SOC showed noticeable discrepancies from the experimental data, particularly in the low-frequency region of the impedance spectra. This result indicates that the selected electrical circuit does not accurately model the system when the lithium-ion concentration in the anode is very high. To address this limitation, alternative circuit models should be analyzed specifically for this SOC. It is also evident that the error bars increase their size at the lower tempeatures, where exists more disparities between batteries as also showed in Figure 4.2.1.

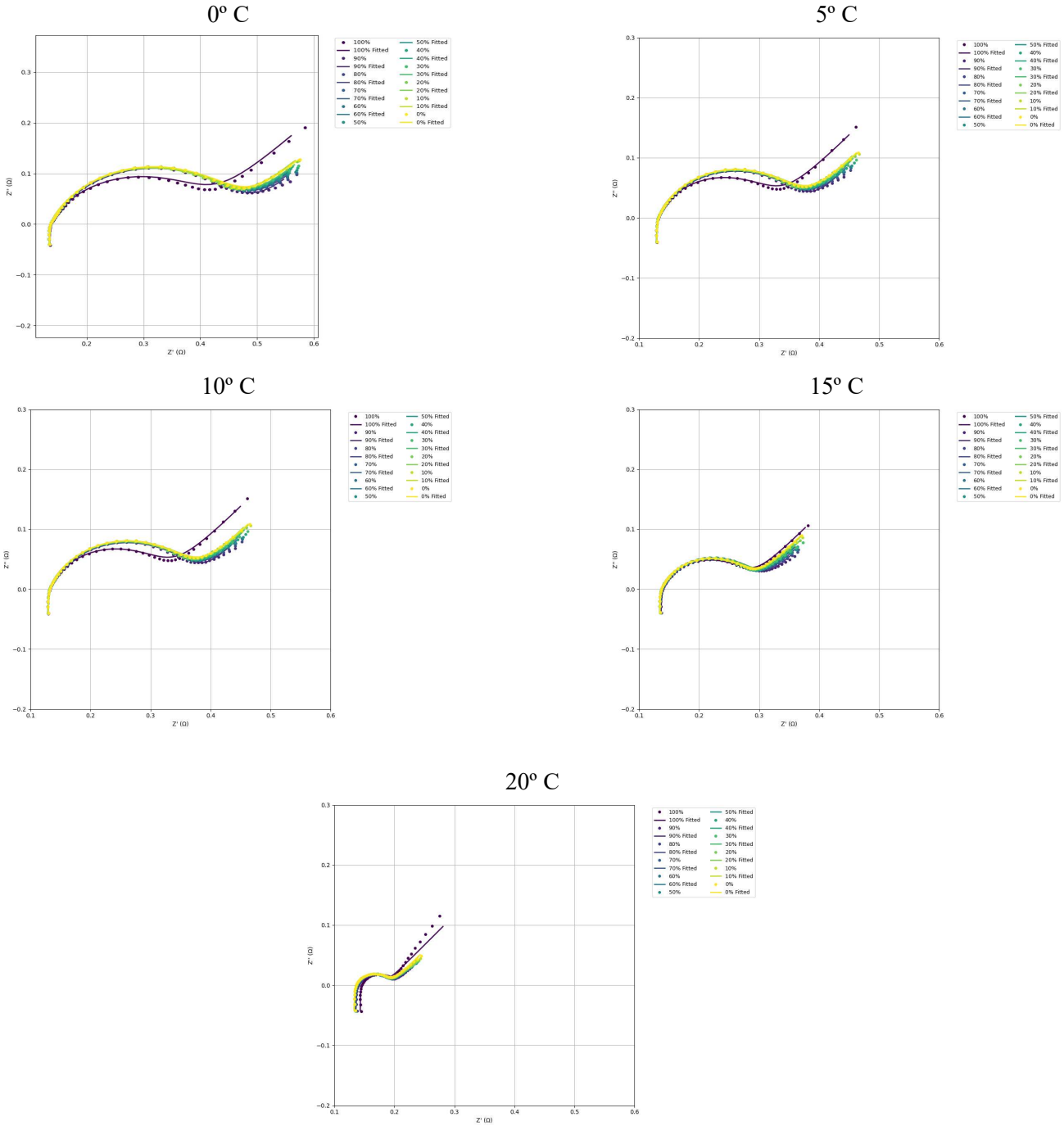


Figure 4.2.3: 10 cycle Average Impedance spectra SOC evolution at the five temperatures defined.

As can be seen in the figures, the measurement with SOC equal to 100% has a very different behaviour from the other measurements. This can be explained by analysing what is happening at the electrochemical level. At high SOC values (close to 100%), the concentration of lithium ions in the positive electrode (cathode) is low. Without lithium ions, the characteristic diffusion times tend to be infinite, and the impedance is higher than other SOCs. Overall, considering the chemistry, type, and capacity of the cells analysed, the results of impedance measurements shown by Nyquist plots are consistent with those described in previous works [59]. For further analysis, all results obtained at 100% SOC, more specifically those related to the circuit parameters in the mid- to low-frequency region of the impedance spectra, will be biased due to the lower accuracy of the electrical circuit used to fit the measured data.

It is also noticeable that there are no significant differences or trends among all SOCs, highlighting the stability of the electrochemical behavior across the batteries, while also showing a good concordancy between the fitted and real data in all spectra. The electrochemical behavior of the batteries remains unchanged with cycling, as shown in Example of impedance spectra section in the Appendix Section (which includes impedance spectra at different temperatures, variations with SOC, and the identification of outliers), and differences related to cycling degradation will be addressed in the next chapter, within the discussion of the electrical components of the ECM.

## 4.3 Circuit parameters analysis

Through the results obtained in Section 4.2, the fitted data allowed the extraction of the electrical circuit components that represent the behaviour of the analysed sample. This chapter is divided into the three main components of the circuits: the charge transfer resistance, related to ion deintercalation within the battery; the series resistance, related to the battery material properties; and the Warburg admittance, related to lithium-ion diffusion. These parameters are examined with respect to the number of cycles and temperature.

### 4.3.1 Charge transfer resistance

The ion deintercalation is highly temperature dependent, since ion intercalation is favoured by an increase in temperature, which accelerates the rate of chemical reactions within the battery and thereby reduces the charge transfer resistance of the electrochemical system [60]. As observed in the previous section, the diameter of the semicircle (proportional to the charge transfer resistance) decreases with increasing temperature. This phenomenon is illustrated in the figures below.

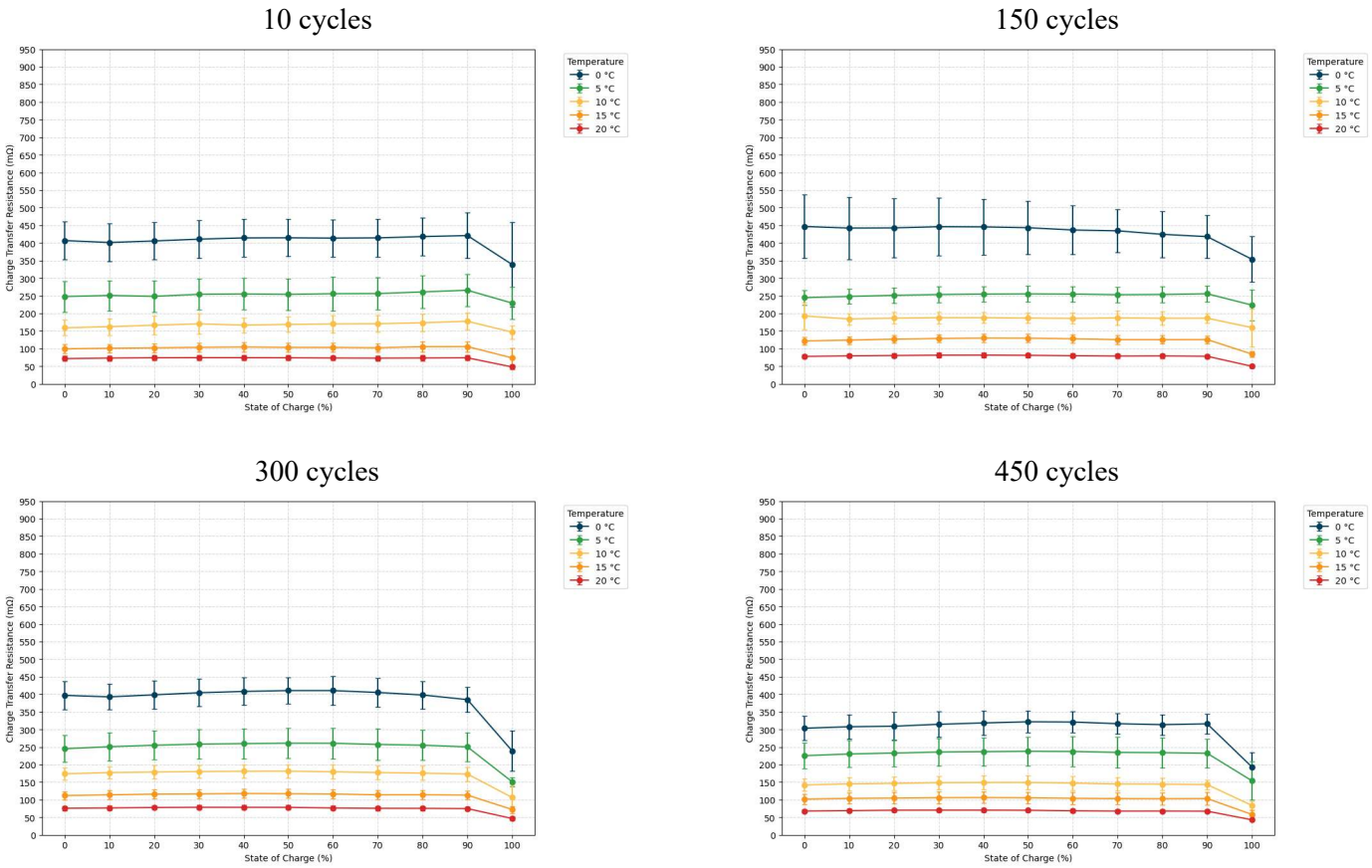


Figure 4.3.1: Charge transfer resistance evolution with cycling at different temperatures.

As observed in Figure 4.3.1, the charge transfer resistance decreases with increasing temperature, with large differences between the lowest temperature (0 °C) and the higher temperatures. However, the gap between successive temperatures becomes smaller at higher temperatures. There is no significant variation with SOC, as $R_{ct}$ remains nearly constant, except at 100%, where the selected equivalent circuit model is not appropriate. This tendency is consistent with the literature, which reports that the charge transfer impedance (mid-to-low frequency semicircle) increases significantly at lower temperatures [10].

It is also remarkable that the values of $R_{ct}$ for LFP 3 and LFP 8 (See Figure A.1.14 in the Appendix), are out of the considered range (two times the standard deviation), confirming that the outlier data of these batteries in the impedance spectra corresponds to the diameter of the semicircle.

Regarding the effect of cycling on the semicircle diameter, no significant impact on the charge transfer impedance was observed between 10 and 450 cycles. As shown in Figure 4.3.2, no trends are evident across the number of cycles considered during the experimental period. This behaviour is directly related to the stability and long lifespan of the LFP battery. A slight trend may be present, but given the size of the error bars, its significance cannot be determined. More batteries or repeated measurements would be required to reduce these uncertainties. This indicates that each battery behaves differently: if the history of a battery is known, its degradation can be observed, but for an unknown battery, it would be difficult to determine the number of cycles based solely on $R_{ct}$ as a function of SOC and temperature. These results are consistent with observations reported in the literature [61], a significant decrease in charge transfer resistance is only observed after 450 cycles.

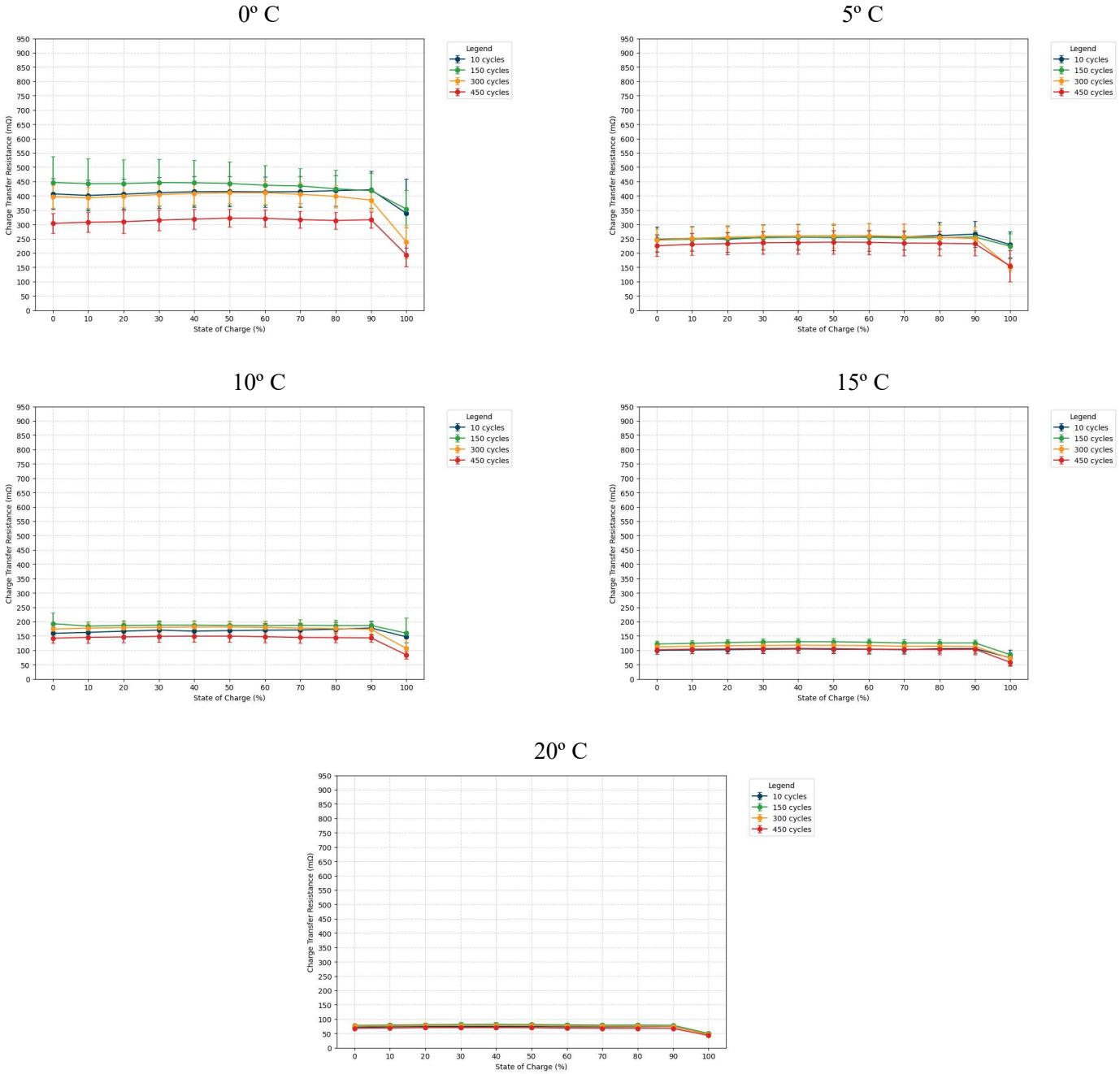


Figure 4.3.2: Charge transfer resistance evolution with temperatures at different number of cycles with outliers' representation.

### 4.3.2 Series Resistance

As seen in previous spectra, it is noticeable that the intersection on the Z' axis, corresponding to the series resistance, does not vary significantly across different temperatures. This behaviour is shown in the figure below, where the effect of outliers is not emphasized.

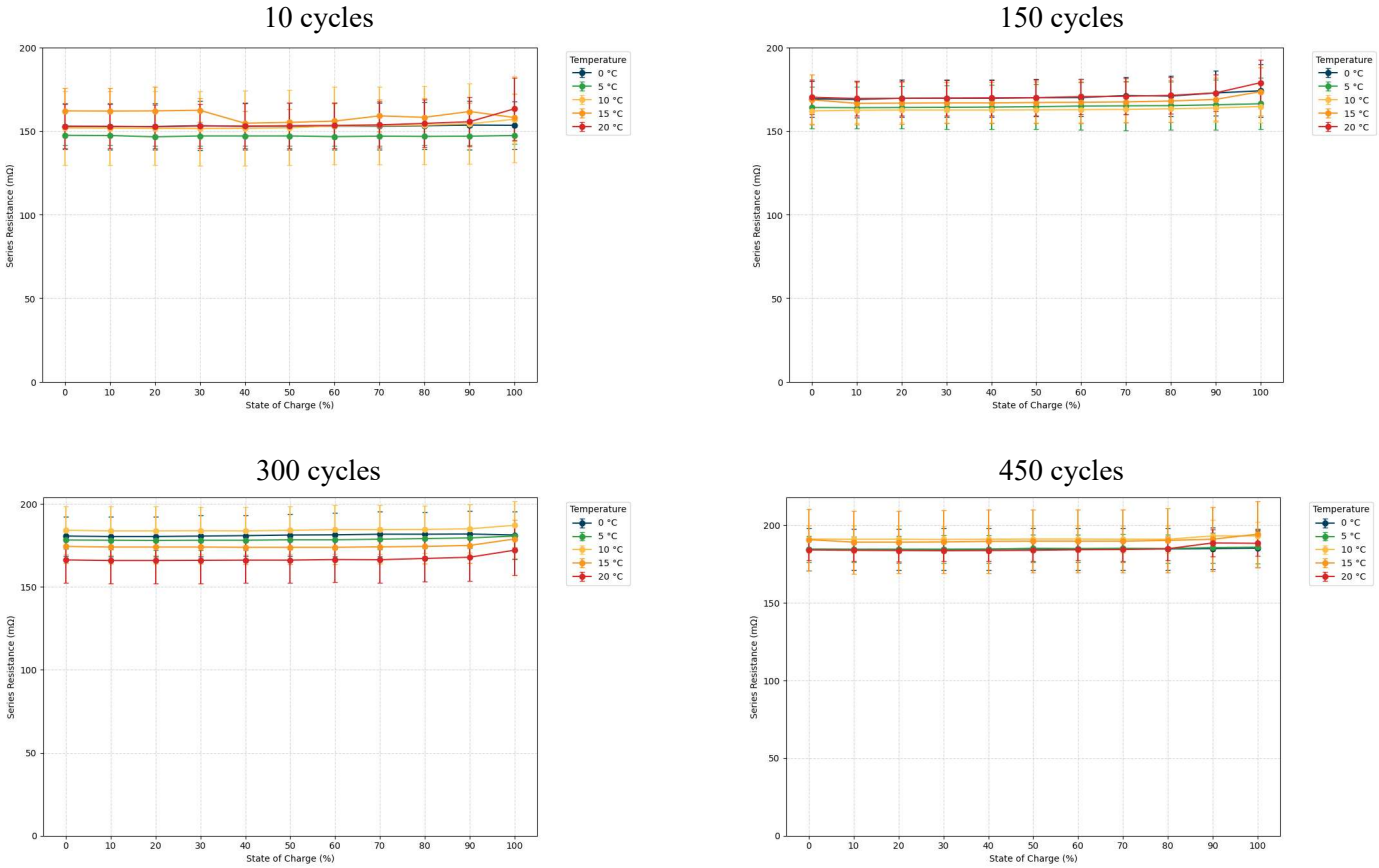


Figure 4.3.3: Series Resistance evolution with temperatures at different number of cycles

Figure 4.3.3 evidence that there are no observable trends in the series resistance with temperature. No degradation is seen in the measured impedance spectra at different temperatures, as the electrolyte and material properties remain unchanged. Only the charge transfer and ion diffusion behaviour increase or decrease, as also observed in the literature and as shown in Figure 2.7.2.

The error bars are represented in the same way as for the charge transfer resistance, corresponding to two times the standard deviation of the sample, with the average values for each temperature shown. In this case, the data at 100% SOC do not present issues, as the interception on the real axis does not depend on the low frequency region, where the electrical circuit doesn't fit the real data.

As previously explained in Chapter 2, a growth of the SEI layer on the electrode surface and the loss of active material are expected with the number of cycles. For this reason, a shift to the right in the impedance spectra occurs. This rightward shift in the spectra is directly related to an increase in the series resistance, as shown in the figure below.

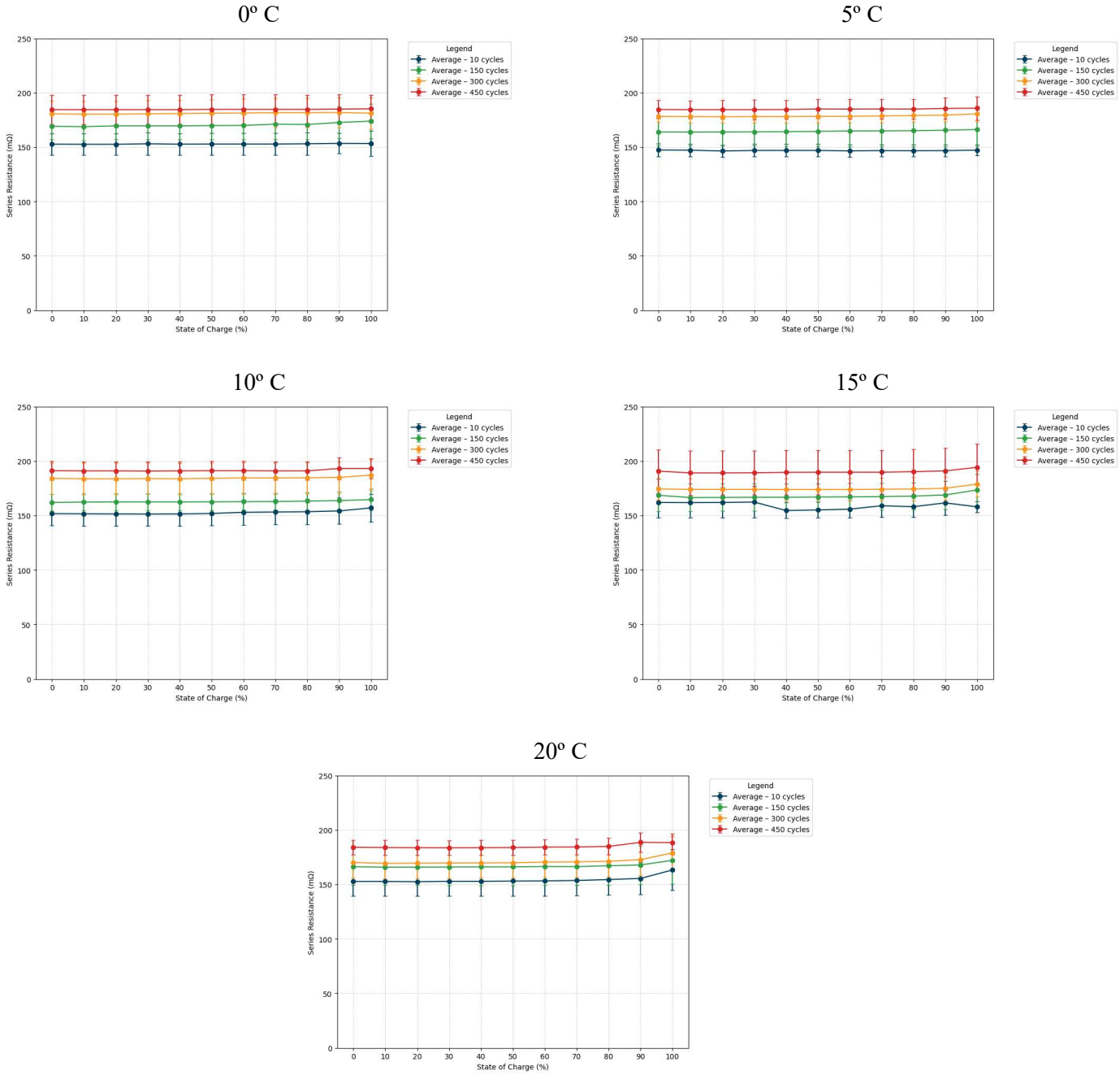


Figure 4.3.4: Series resistance evolution with temperatures at different numbers of cycles.

From the figures above, it can be noted that the series resistance increases with the battery cycling, i.e., the number of cycles, showing an increase in resistance along with the number of cycles that may be related to the degradation of battery components [62,63]. It is important to remark that the series resistance is directly influenced by the DOD and the charging protocols adopted in this study. Varying the DOD or C-rates for charge and discharge could result in measured data with higher variance, as reported in the literature [63].

### 4.3.3 Warburg admittance

Normally, when analysing circuit parameters obtained from fitting an equivalent electrical circuit, the Warburg admittance is discussed, as it models the low-frequency response of an electrochemical system and reflects the rate of ion diffusion in the cell. Ion diffusion is a temperature-

dependent property. As shown in Figure 4.3.5, the admittance clearly increases with temperature, which aligns with literature reports. In particular, the Warburg impedance, which is the inverse of admittance, decreases as temperature rises, indicating an increase in the solid-state diffusion coefficient of the active material at higher temperatures [64].

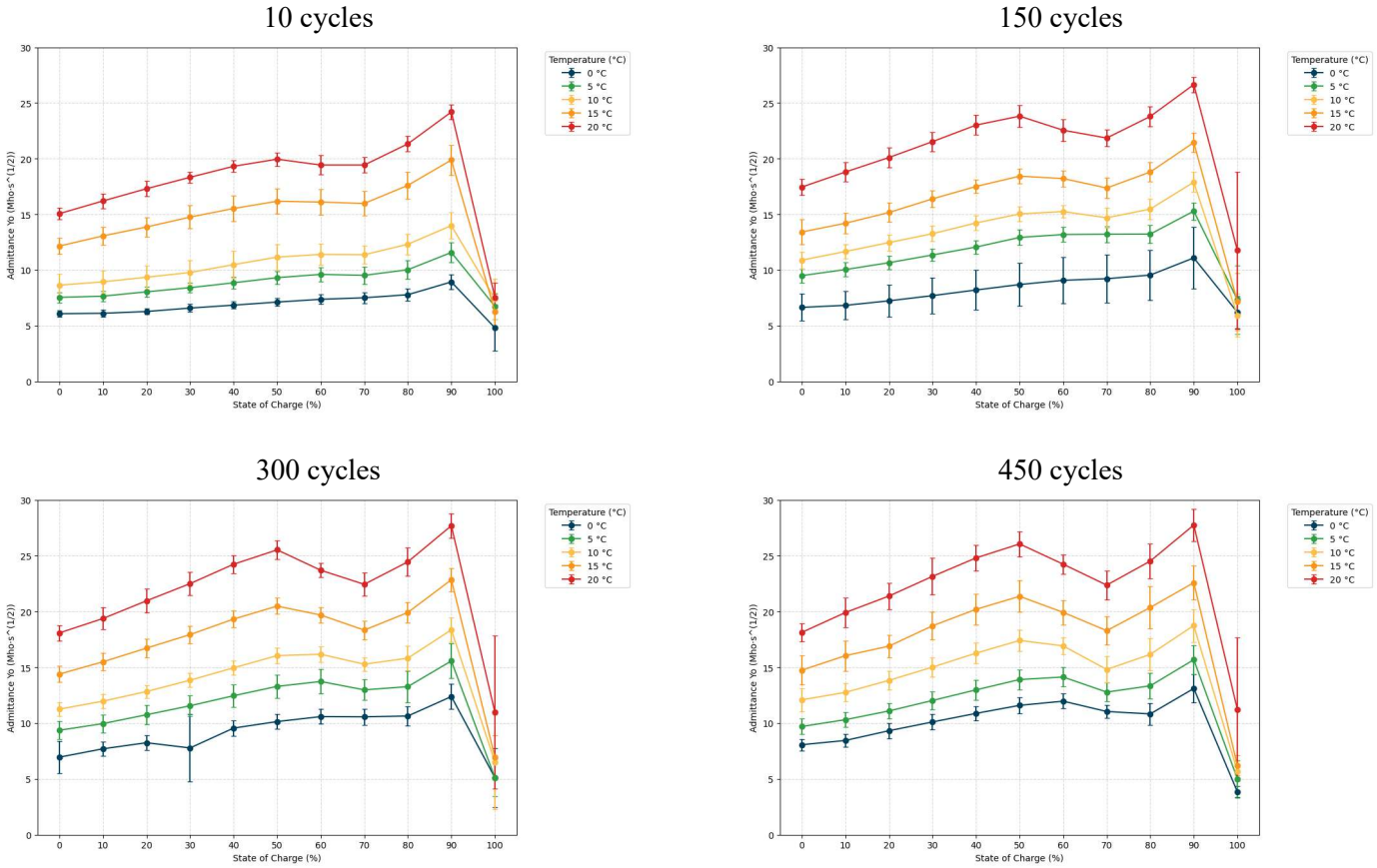


Figure 4.3.5: Warburg admittance evolution with temperature at different numbers of cycles.

Figure 4.3.5 shows a clear trend of increasing admittance as SOC rises from 0% to 90%, highlighting how ion diffusion and charge transport become more pronounced at higher SOCs. Across all cycle numbers, it is evident that admittance increases at higher temperatures, heavily influenced by the acceleration of electrochemical kinetics and lower resistance in ion diffusion in the LFP cell. At 100% SOC, admittance abruptly drops across all temperatures and cycles, suggesting that the ECM model selected for fitting does not capture the real behaviour of the LFP cell at full charge, as sustained by the large error bars presented.

As the cycling protocols were conservative, meaning the LFP were not forced into fast cycles and always operated within technical specification limits, the ion diffusion in the experiment is not heavily affected by the number of cycles. This highlights the stability of LFP ion transport under ideal conditions. As reported in the literature, LFP batteries can maintain stable electrochemical performance and ion diffusion over thousands of cycles under moderate SOC ranges and conservative charging rates, demonstrating their long-term stability [65,66].

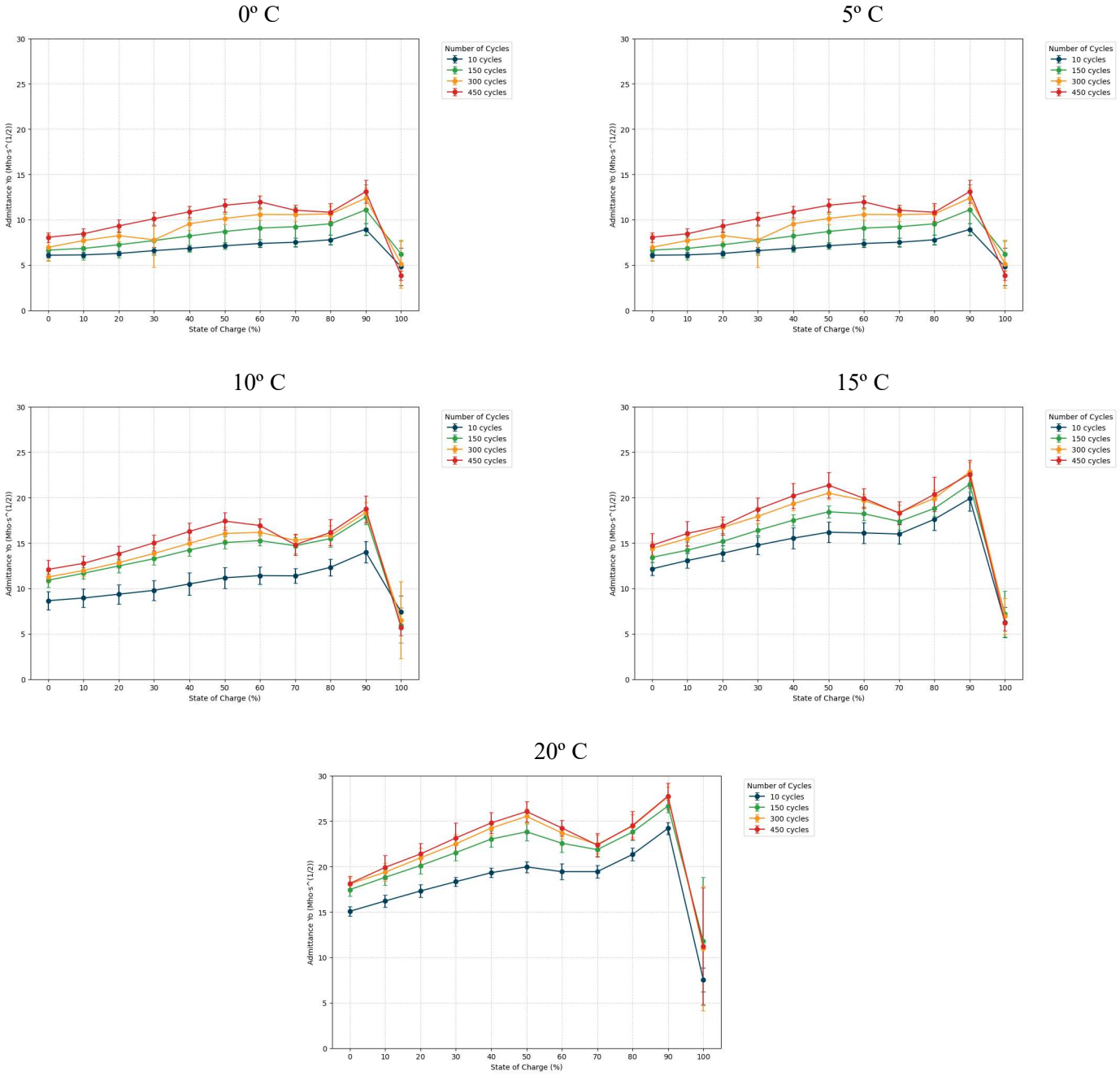


Figure 4.3.6: Warburg admittance evolution with cycling at different temperatures.

Figure 4.3.6 evidences a lower admittance for all temperatures at the early stage of the battery, which suggests that the Warburg admittance is stimulated with cycling, as reported in previous studies [67]. This behaviour indicates that ion difussion becomes more accessible after initial cycling, possibly related to structural and morphological changes in LFP [68]. Moreover, a slight increase in Warburg admittance is observed across all temperatures from 150 cycles to 450 cycles, indicating consistent trend for admittance to growth in the early stages of cycling.

## 4.4 Prediction of Battery Cycle Life Using EIS spectra and Derived Circuit Parameters

By analysing the obtained average spectra, a rightward shift with cycling is noticeable, indicating a continuous increase in series resistance (Figure 4.3.4). This behaviour clearly indicates degradation of the battery components, independent of the measurement temperature, and aligns with the degradation rate reported in the literature [42], which is approximately 20% in both cases at the same stage (400 cycles).

Charge transfer resistance can serve as an indicator of the battery's environmental temperature, as it is a temperature sensitive parameter. However, it does not show significant variations or dependency on the battery's state of health within the evaluated period, which makes it unsuitable for estimating battery lifespan in this study. As shown in Figure 4.4.1, the data from the cycling tests reveal a small initial increase in charge transfer resistance at the beginning of the cycles, followed by a gradual decrease as cycling progresses. This behaviour is more pronounced at lower temperatures, particularly at 0ºC, where the resistance starts higher and decreases more noticeably compared to higher temperatures.

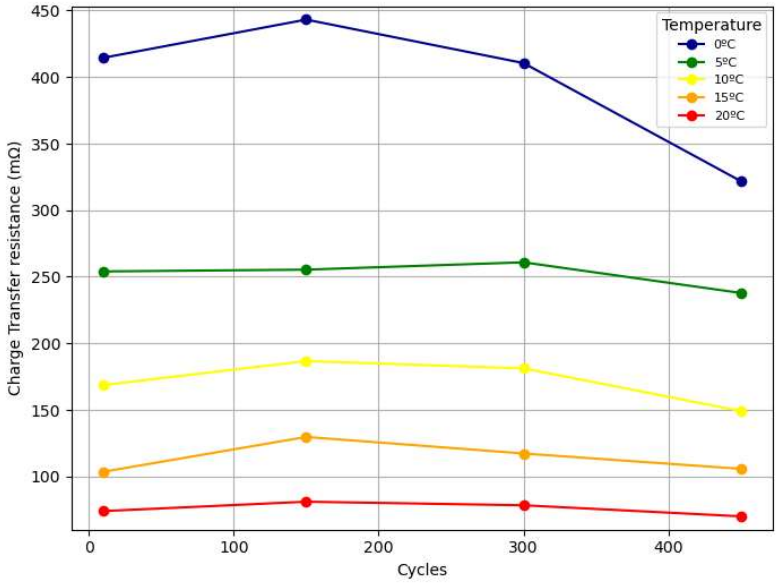


Figure 4.4.1:Charge Transfer Resistance with cycling at 50% SOC and different temperatures.

Warburg admittance tends to increase compared to the early stage of cycling, which may help determine whether a battery has already been cycled or is completely fresh. This parameter is also temperature-dependent, allowing an approximation of both battery temperature and stage of life simultaneously.

It is important to note that the cycling sample remains in the early stage of battery life, as previously discussed, considering that LFP batteries typically have a lifespan of 2000 cycles or more, therefore, the period analysed in this work represents only about one quarter of the minimum expected battery life.

To properly define trends in circuit parameter evolution and electrochemical impedance spectroscopy, more pronounced degradation is required, reaching cycle numbers closer to the end of life. In this study, the small degradation observed at the early stage indicates the stability of LFP batteries under different cycling temperature conditions when evaluated using EIS measurements.

# 5 Conclusions and future suggestions

The research explored the effects of both temperature and cycling conditions on the capacity and the electrochemical performance of the LFP batteries. It was observed that the capacity remained stable throughout the experiment, without remarkable fade, showing that under standard cycling conditions there is no significant effects on the SOH.

In the future, a higher number of cycles could be performed to determine when the capacity actually fades under standard cycling at 100% DOD, allowing comparison with the supplier specifications. Another route for future work could include faster cycling, in order to accelerate the degradation of the LFP batteries and provide more insight into battery degradation within a shorter period. Cycling at a fixed non ideal temperature would be an interesting direction for future research, to observe whether battery capacity degradation is accelerated under such conditions.

The electrochemical behaviour of LFP batteries is extremely sensitive to temperature changes, particularly in relation to charge transfer resistance. Results proven that ion deintercalation is enhanced at higher temperatures and reduced at lower temperatures. In contrast, series resistance shows no significant dependence on temperature, but rather on lifespan, as an increasing number of cycles leads to higher series resistance, thus slowing charge/discharge processes, being an indicator on the cycling conditions adopted.

Warburg admittance, which is related to ion diffusion, was shown experimentally to be proportional to temperature. For future work, increasing data resolution, therefore increase number of frequencies in EIS measurements, and testing at a lower range of temperatures could provide impedance spectra with two semicircles, enabling ECM fitting with different orders of RC components and offering deeper insight into the degradation mechanisms of LFP batteries. ECM fitting is inaccurate at 100% SOC, and another equivalent circuit could be implemented to reduce data inaccuracy.

This experimental data could be an indicator the estimation of the lifespan of an LFP battery when circuit parameters and impedance spectra are measured, always considering the temperature to which the battery is examined. It is important to note that future work is required to obtain a larger dataset, which would allow for the identification of additional trends in the evolution of ECM parameters at higher lifespans and a more accurate estimation of the number of cycles.

One possible approach for upcoming study could be to continue cycling and testing the already used batteries to reach a higher number of cycles, allowing for the observation of capacity fade and the emergence of the second semicircle in the impedance spectra.

# 6 References


[1] T. M. Bandhauer, S. Garimella, and T. F. Fuller, "A critical review of thermal issues in lithium-ion batteries," J. Electrochem. Soc., vol. 158, no. 3, p. R1, 2011, doi: 10.1149/1.3515880.

[2] S. O'Neill, "Development of lithium-ion batteries wins Nobel Prize," Engineering, vol. 6, no. 5, pp. 487–488, May 2020, doi: 10.1016/j.eng.2020.03.010.

[3] A. K. Padhi, K. S. Nanjundaswamy, and J. B. Goodenough, "Phospho-olivines as positive-electrode materials for rechargeable lithium batteries," J. Electrochem. Soc., vol. 144, no. 4, pp. 1188–1194, Apr. 1997, doi: 10.1149/1.1837571.

[4] P. D. Lund, J. Lindgren, J. Mikkola, and J. Salpakari, "Review of energy system flexibility measures to enable high levels of variable renewable electricity," Renew. Sustain. Energy Rev., vol. 45, pp. 785–807, May 2015, doi: 10.1016/j.rser.2015.01.057.

[5] International Energy Agency (IEA), Global EV Outlook 2025. Paris, France: IEA, May 2025. [Online]. Available: https://www.iea.org/reports/global-ev-outlook-2025 [Accessed: Oct. 27, 2025].

[6] C. Long, J. Wu, Y. Zhou, and N. Jenkins, "Peer-to-peer energy sharing through a two-stage aggregated battery control in a community microgrid," Appl. Energy, vol. 226, pp. 261–276, Sept. 2018, doi: 10.1016/j.apenergy.2018.05.097.

[7] R. Korthauer, Ed., Lithium-Ion Batteries: Basics and Applications. Berlin, Heidelberg: Springer, 2018, doi: 10.1007/978-3-662-53071-9.

[8] M. M. Kabir and D. E. Demirocak, "Degradation mechanisms in Li-ion batteries: a state-of-the-art review," Int. J. Energy Res., vol. 41, no. 14, pp. 1963–1986, Nov. 2017, doi: 10.1002/er.3762.

[9] International Energy Agency (IEA), Global EV Outlook 2023: Catching Up with Climate Ambitions. Paris, France: OECD, 2023. [Online]. Available: https://doi.org/10.1787/cbe724e8-en [Accessed: Jan. 3, 2025].

[10] A. S. Keefe, S. Buteau, I. G. Hill, and J. R. Dahn, "Temperature dependent EIS studies separating charge transfer impedance from contact impedance in lithium-ion symmetric cells," J. Electrochem. Soc., vol. 166, no. 14, 2019, doi: 10.1149/2.0541914jes.

[11] A. Fly, I. Kirkpatrick, and R. Chen, "Low temperature performance evaluation of electrochemical energy storage technologies," Appl. Therm. Eng., vol. 189, p. 116750, May 2021, doi: 10.1016/j.applthermaleng.2021.116750.

[12] S. Ma et al., "Temperature effect and thermal impact in lithium-ion batteries: A review," Prog. Nat. Sci. Mater. Int., vol. 28, no. 6, pp. 653–666, Dec. 2018, doi: 10.1016/j.pnsc.2018.11.002.

[13] J. Garche, Ed., Encyclopedia of Electrochemical Power Sources. Amsterdam: Elsevier, 2009.

[14] M. Winter and B. Barnett, "BU 205: Types of Lithium ion," Battery University, Dec. 8, 2023. [Online]. Available: https://batteryuniversity.com/article/bu-205-types-of-lithium-ion [Accessed: Jan. 4, 2025].

[15] D. Linden and T. B. Reddy, "BU-216: Summary Table of Lithium-based Batteries," Battery University. [Online]. Available: https://batteryuniversity.com/article/bu-216-summary-table-of-lithium-based-batteries [Accessed: Jan. 15, 2025].

[16] Q. Wu, B. Zhang, and Y. Lu, "Progress and perspective of high-voltage lithium cobalt oxide in lithium-ion batteries," J. Energy Chem., vol. 74, pp. 283–308, Nov. 2022, doi: 10.1016/j.jechem.2022.07.007.

[17] Q.-Q. Yu, R. Xiong, L.-Y. Wang, and C. Lin, "A comparative study on open circuit voltage models for lithium-ion batteries," Chin. J. Mech. Eng., vol. 31, no. 1, p. 65, Dec. 2018, doi: 10.1186/s10033-018-0268-8.

[18] O. Capron, R. Gopalakrishnan, J. Jaguemont, P. Van Den Bossche, N. Omar, and J. Van Mierlo, "On the ageing of high energy lithium-ion batteries—comprehensive electrochemical diffusivity studies of harvested nickel manganese cobalt electrodes," Materials, vol. 11, no. 2, p. 176, Jan. 2018, doi: 10.3390/ma11020176.

[19] MIT Electric Vehicle Team, "A Guide to Understanding Battery Specifications," MIT EVT, Dec. 2008. [Online]. Available: https://web.mit.edu/evt/summary_battery_specifications.pdf . [Accessed: Jan. 15, 2025].

[20] B. Xia, C. Chen, Y. Tian, M. Wang, W. Sun, and Z. Xu, "State of charge estimation of lithium-ion batteries based on an improved parameter identification method," Energy, vol. 90, pp. 1426–1434, Oct. 2015, doi: 10.1016/j.energy.2015.06.095.
[21] A. Ahmadian, M. Sedghi, A. Elkamel, M. Fowler, and M. Aliakbar Golkar, "Plug-in electric vehicle batteries degradation modeling for smart grid studies: Review, assessment and conceptual framework," Renew. Sustain. Energy Rev., vol. 81, pp. 2609–2624, Jan. 2018, doi: 10.1016/j.rser.2017.06.067.
[22] S. Chowdhury, M. N. B. Shaheed, and Y. Sozer, "An integrated state of health (SOH) balancing method for lithium-ion battery cells," in Proc. IEEE Energy Conversion Congress and Exposition (ECCE), Baltimore, MD, USA, Sept. 2019, pp. 5759–5763, doi: 10.1109/ECCE.2019.8912932.
[23] J. S. Edge et al., "Lithium ion battery degradation: what you need to know," Phys. Chem. Chem. Phys., vol. 23, no. 14, pp. 8200–8221, 2021, doi: 10.1039/D1CP00359C.
[24] G. Luo, Y. Zhang, and A. Tang, "Capacity degradation and aging mechanisms evolution of lithium-ion batteries under different operation conditions," Energies, vol. 16, no. 10, p. 4232, May 2023, doi: 10.3390/en16104232.
[25] L. Köbbing, A. Latz, and B. Horstmann, "Growth of the solid-electrolyte interphase: Electron diffusion versus solvent diffusion," J. Power Sources, vol. 561, p. 232651, Mar. 2023, doi: 10.1016/j.jpowsour.2023.232651.
[26] X. Huang, S. Ke, H. Lv, and Y. Liu, "A dynamic capacity fading model with thermal evolution considering variable electrode thickness for lithium-ion batteries," Ionics, vol. 24, no. 11, pp. 3439–3450, Nov. 2018, doi: 10.1007/s11581-018-2476-8.
[27] M. B. Pinson and M. Z. Bazant, "Theory of SEI formation in rechargeable batteries: Capacity fade, accelerated aging and lifetime prediction," J. Electrochem. Soc., vol. 160, no. 2, pp. A243–A250, 2013, doi: 10.1149/2.044302jes.
[28] X. Lin, K. Khosravinia, X. Hu, J. Li, and W. Lu, "Lithium plating mechanism, detection, and mitigation in lithium-ion batteries," Prog. Energy Combust. Sci., vol. 87, p. 100953, Nov. 2021, doi: 10.1016/j.pecs.2021.100953.
[29] S. Hein and A. Latz, "Influence of local lithium metal deposition in 3D microstructures on local and global behavior of lithium-ion batteries," Electrochim. Acta, vol. 201, pp. 354–365, May 2016, doi: 10.1016/j.electacta.2016.01.220.
[30] "Blog – Guide to lithium plating in lithium-ion batteries," Accure, [Online]. Available: https://www.accure.net/battery-knowledge/blog-guide-to-lithium-plating-in-lithium-ion-batteries [Accessed: Jan. 14, 2025].
[31] Z. Wang, Q. Zhao, X. Yu, W. An, and B. Shi, "Impacts of vibration and cycling on electrochemical characteristics of batteries," J. Power Sources, vol. 601, p. 234274, May 2024, doi: 10.1016/j.jpowsour.2024.234274.
[32] Y. Ji, Y. Zhang, and C.-Y. Wang, "Li-Ion cell operation at low temperatures," J. Electrochem. Soc., vol. 160, no. 4, pp. A636–A649, 2013, doi: 10.1149/2.047304jes.
[33] A. Carnovale and X. Li, "A modeling and experimental study of capacity fade for lithium-ion batteries," Energy AI, vol. 2, p. 100032, Nov. 2020, doi: 10.1016/j.egyai.2020.100032.
[34] A. Ch. Lazanas and M. I. Prodromidis, "Electrochemical impedance spectroscopy – a tutorial," ACS Meas. Sci. Au, vol. 3, no. 3, 2023, doi: 10.1021/acsmeasuresciau.2c00070.
[35] H. S. Magar, R. Y. A. Hassan, and A. Mulchandani, "Electrochemical impedance spectroscopy (EIS): Principles, construction, and biosensing applications," Sensors, vol. 21, no. 19, p. 6578, Oct. 2021, doi: 10.3390/s21196578.
[36] IEST Battery, "An Overview of Electrochemical Impedance Spectroscopy (EIS) for Lithium-Ion Batteries," IEST Battery, Aug. 15, 2025. [Online]. Available: https://iestbattery.com/overview-of-electrochemical-impedance-spectroscopy/ [Accessed: Jan. 10, 2025].
[37] W. Choi, H.-C. Shin, J. M. Kim, J.-Y. Choi, and W.-S. Yoon, "Modeling and applications of electrochemical impedance spectroscopy (EIS) for lithium-ion batteries," J. Electrochem. Sci. Technol., vol. 11, no. 1, pp. 1–13, Feb. 2020, doi: 10.33961/jecst.2019.00528.
[38] M. Gaberscek, J. Moskon, B. Erjavec, R. Dominko, and J. Jamnik, "The importance of interphase contacts in Li ion electrodes: The meaning of the high-frequency impedance arc," Electrochem. Solid-State Lett., vol. 11, no. 10, p. A170, 2008, doi: 10.1149/1.2964220.

[39] D. M. G. Preethichandra and P. Sonar, "Electrochemical impedance spectroscopy and its applications in sensor development and measuring battery performance," IEEE Sens. J., vol. 22, no. 11, pp. 10152–10162, June 2022, doi: 10.1109/JSEN.2021.3119650.
[40] P. Iurilli, C. Brivio, and V. Wood, "On the use of electrochemical impedance spectroscopy to characterize and model the aging phenomena of lithium-ion batteries: A critical review," J. Power Sources, vol. 505, p. 229860, Sept. 2021, doi: 10.1016/j.jpowsour.2021.229860.
[41] J. Huang, Z. Li, B. Y. Liaw, and J. Zhang, "Graphical analysis of electrochemical impedance spectroscopy data in Bode and Nyquist representations," J. Power Sources, vol. 309, pp. 82–98, Mar. 2016, doi: 10.1016/j.jpowsour.2016.01.073.
[42] N. Meddings et al., "Application of electrochemical impedance spectroscopy to commercial Li-ion cells: A review," J. Power Sources, vol. 480, p. 228742, Dec. 2020, doi: 10.1016/j.jpowsour.2020.228742.
[43] X. Wu et al., "Effects of temperature on electrochemical impedance spectroscopy of the LiFePO4 battery," IOP Conf. Ser. Earth Environ. Sci., vol. 675, no. 1, p. 012220, Feb. 2021, doi: 10.1088/1755-1315/675/1/012220.
[44] D. V. G. Rodrigues, "Electrochemical impedance spectroscopy for diagnosing cycling degradation in commercial LiFePO4 cells: Lessons on the role of temperature," unpublished.
[45] H. Nunes, J. Martinho, J. Fermeiro, J. Pombo, S. Mariano, and M. do R. Calado, "Impedance analysis and parameter estimation of lithium-ion batteries using the EIS technique," IEEE Trans. Ind. Appl., vol. 60, no. 3, pp. 5048–5060, May 2024, doi: 10.1109/TIA.2024.3365451.
[46] K. Mc Carthy, H. Gullapalli, and T. Kennedy, "Real-time internal temperature estimation of commercial Li-ion batteries using online impedance measurements," J. Power Sources, vol. 519, p. 230786, Jan. 2022, doi: 10.1016/j.jpowsour.2021.230786.
[47] F. A. Perdana, A. Supriyanto, A. Purwanto, and A. Jamaluddin, "Study of imbalanced internal resistance on drop voltage of LiFePO4 battery system connected in parallel," J. Phys. Conf. Ser., vol. 795, p. 012036, Jan. 2017, doi: 10.1088/1742-6596/795/1/012036.
[48] D. Li and H. Zhou, "Two-phase transition of Li-intercalation compounds in Li-ion batteries," Mater. Today, vol. 17, no. 9, pp. 451–463, Nov. 2014, doi: 10.1016/j.mattod.2014.06.002.
[49] X. Li, M. Xiao, S.-Y. Choe, and W. T. Joe, "Modeling and analysis of LiFePO4/Carbon battery considering two-phase transition during galvanostatic charging/discharging," Electrochim. Acta, vol. 155, pp. 447–457, Feb. 2015, doi: 10.1016/j.electacta.2014.12.034.
[50] M. Berecibar, M. Garmendia, I. Gandiaga, J. Crego, and I. Villarreal, "State of health estimation algorithm of LiFePO4 battery packs based on differential voltage curves for battery management system application," Energy, vol. 103, pp. 784–796, May 2016, doi: 10.1016/j.energy.2016.02.163.
[51] J. Vetter et al., "Ageing mechanisms in lithium-ion batteries," J. Power Sources, vol. 147, no. 1–2, pp. 269–281, Sept. 2005, doi: 10.1016/j.jpowsour.2005.01.006.
[52] S. Lehner, T. Baumhöfer, and D. U. Sauer, "Disparity in initial and lifetime parameters of lithium-ion cells," IET Electr. Syst. Transp., vol. 6, no. 1, pp. 34–40, Mar. 2016, doi: 10.1049/iet-est.2015.0007.
[53] J. Guo, Y. Li, J. Meng, K. Pedersen, L. Gurevich, and D.-I. Stroe, "Understanding the mechanism of capacity increase during early cycling of commercial NMC/graphite lithium-ion batteries," J. Energy Chem., vol. 74, pp. 34–44, Nov. 2022, doi: 10.1016/j.jechem.2022.07.005.
[54] M. Dubarry, C. Truchot, and B. Y. Liaw, "Synthesize battery degradation modes via a diagnostic and prognostic model," J. Power Sources, vol. 219, pp. 204–216, Dec. 2012, doi: 10.1016/j.jpowsour.2012.07.016.
[55] M. Lewerenz, J. Münnix, J. Schmalstieg, S. Käbitz, M. Knips, and D. U. Sauer, "Systematic aging of commercial LiFePO4 |Graphite cylindrical cells including a theory explaining rise of capacity during aging," J. Power Sources, vol. 345, pp. 254–263, Mar. 2017, doi: 10.1016/j.jpowsour.2017.01.133.
[56] B. Gyenes, D. A. Stevens, V. L. Chevrier, and J. R. Dahn, "Understanding anomalous behavior in coulombic efficiency measurements on Li-ion batteries," J. Electrochem. Soc., vol. 162, no. 3, pp. A278–A283, 2015, doi: 10.1149/2.0191503jes.

[57] Y. Kobayashi, H. Miyashiro, A. Yamazaki, and Y. Mita, "Unexpected capacity fade and recovery mechanism of LiFePO4/graphite cells for grid operation," J. Power Sources, vol. 449, p. 227502, Feb. 2020, doi: 10.1016/j.jpowsour.2019.227502.
[58] Y. Xiao, X. Huang, J. Meng, Y. Zhang, V. Knap, and D.-I. Stroe, "Electrochemical impedance spectroscopy-based characterization and modeling of lithium-ion batteries based on frequency selection," Batteries, vol. 11, no. 1, p. 11, Dec. 2024, doi: 10.3390/batteries11010011.
[59] H. Mustafa, C. Bourelly, M. Vitelli, F. Milano, M. Molinara, and L. Ferrigno, "SoC estimation on Li-ion batteries: A new EIS-based dataset for data-driven applications," Data Brief, vol. 57, p. 110947, Dec. 2024, doi: 10.1016/j.dib.2024.110947.
[60] V. Ovejas and A. Cuadras, "Impedance characterization of an LCO-NMC/Graphite cell: Ohmic conduction, SEI transport and charge-transfer phenomenon," Batteries, vol. 4, no. 3, p. 43, Sept. 2018, doi: 10.3390/batteries4030043.
[61] L. M. Thompson et al., "Study of electrolyte and electrode composition changes vs time in aged Li-ion cells," J. Electrochem. Soc., vol. 168, no. 2, p. 020532, Feb. 2021, doi: 10.1149/1945-7111/abe1da.
[62] J. S. Menye, M.-B. Camara, and B. Dakyo, "Lithium battery degradation and failure mechanisms: A state-of-the-art review," Energies, vol. 18, no. 2, p. 342, Jan. 2025, doi: 10.3390/en18020342.
[63] J. G. Qu, Z. Y. Jiang, and J. F. Zhang, "Investigation on lithium-ion battery degradation induced by combined effect of current rate and operating temperature during fast charging," J. Energy Storage, vol. 52, p. 104811, Aug. 2022, doi: 10.1016/j.est.2022.104811.
[64] A. Fly, B. Wimarshana, I. Bin-Mat-Arishad, and M. Sarmiento-Carnevali, "Temperature dependency of diagnostic methods in lithium-ion batteries," J. Energy Storage, vol. 52, p. 104721, Aug. 2022, doi: 10.1016/j.est.2022.104721.
[65] T.-Y. Shim et al., "Enhanced C-rate capability and long-term cycling behavior of LiFePO4/C-BaTiO3 composite cathode," J. Energy Storage, vol. 90, p. 111915, June 2024, doi: 10.1016/j.est.2024.111915.
[66] J. Kang, G. Yang, Y. Wang, J. V. Wang, Q. Wang, and G. Zhu, "Study of aging mechanisms in LiFePO4 batteries with various SOC levels using the zero-sum pulse method," iScience, vol. 27, no. 7, p. 110287, July 2024, doi: 10.1016/j.isci.2024.110287.
[67] U. Tröltzsch, O. Kanoun, and H.-R. Tränkler, "Characterizing aging effects of lithium ion batteries by impedance spectroscopy," Electrochim. Acta, vol. 51, no. 8–9, pp. 1664–1672, Jan. 2006, doi: 10.1016/j.electacta.2005.02.148.
[68] D.-T. Ngo, R. Scipioni, S. B. Simonsen, P. S. Jørgensen, and S. H. Jensen, "A TEM study of morphological and structural degradation phenomena in LiFePO4-CB cathodes," Int. J. Energy Res., vol. 40, no. 14, pp. 2022–2032, Nov. 2016, doi: 10.1002/er.3575.

# Appendix

## A.1 Example of Impedance Spectra of LFP batteries

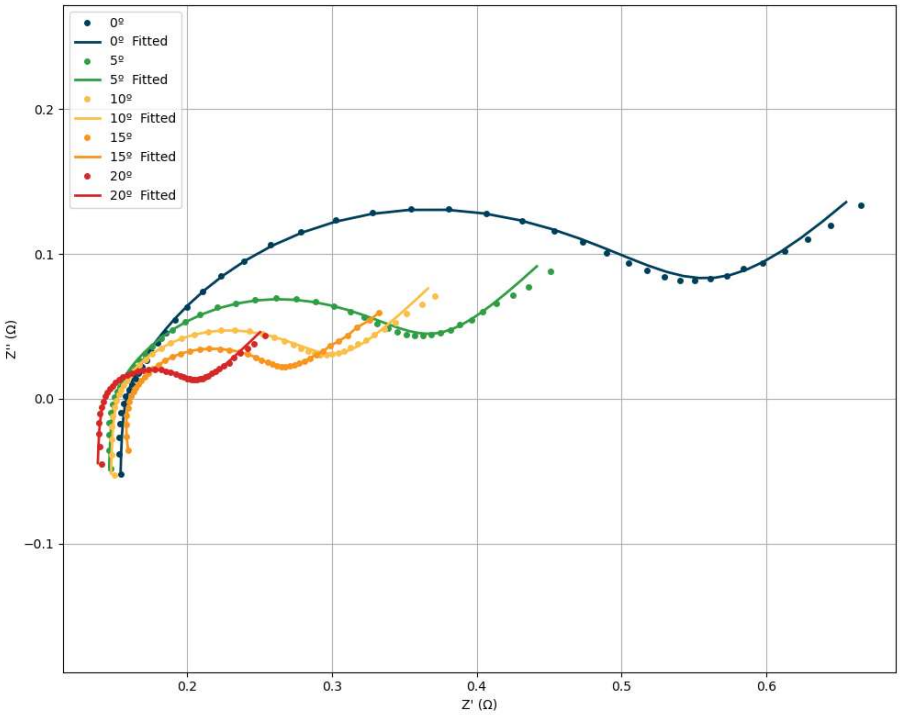


Figure A.1.1: Impedance spectra of the LFP 1 at 50% SOC and different temperatures at 10 cycles.

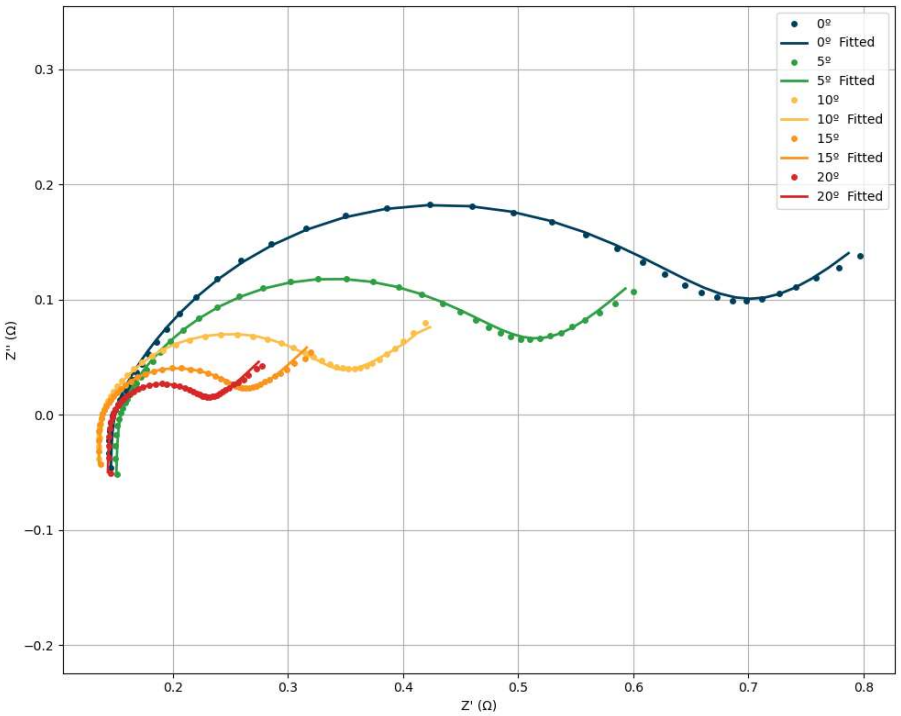


Figure A.1.2: Impedance spectra of the LFP 2 at 50% SOC and different temperatures at 10 cycles.

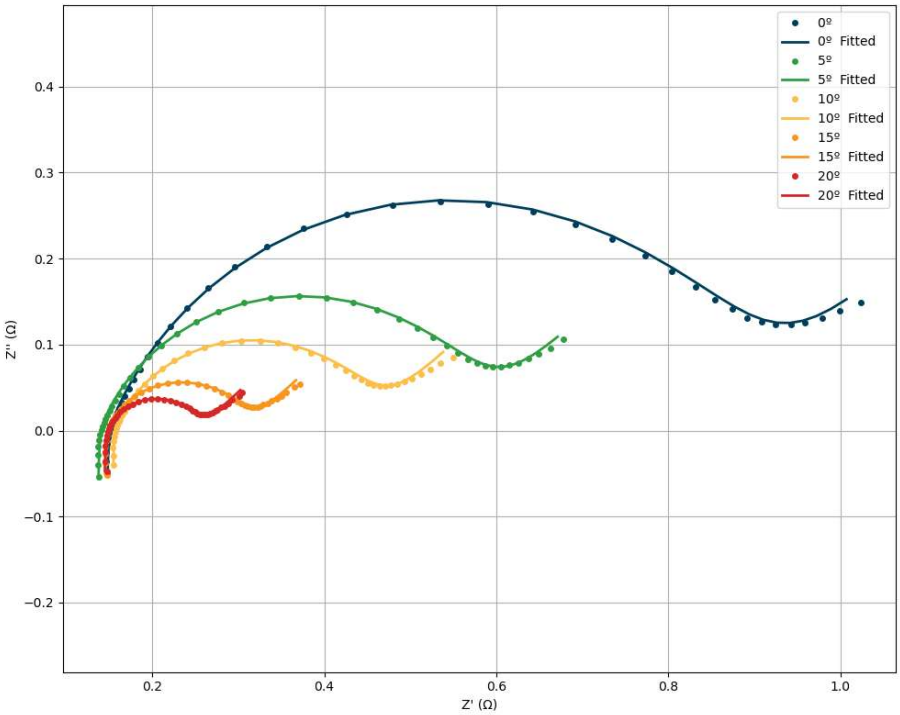


Figure A.1.3: Impedance spectra of the LFP 3 at 50% SOC and different temperatures at 10 cycles.

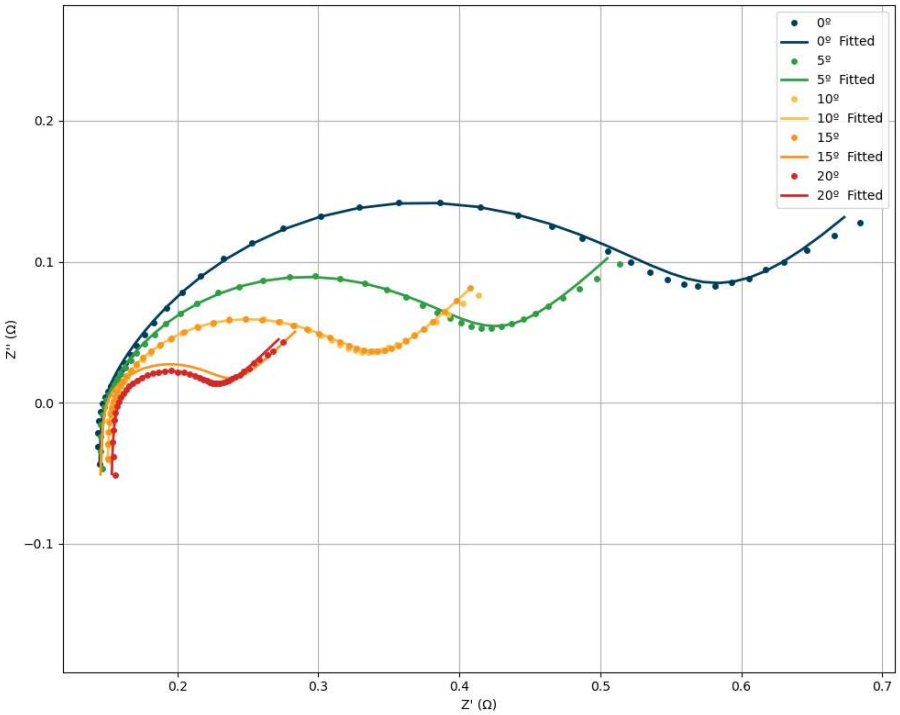


Figure A.1.4: Impedance spectra of the LFP 4 at 50% SOC and different temperatures at 10 cycles.

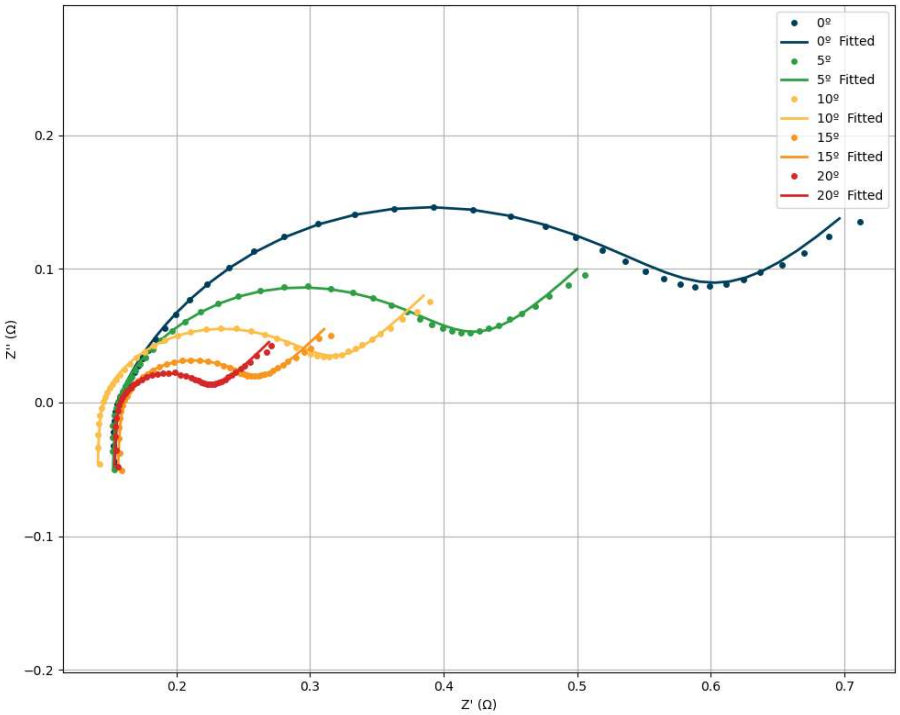


Figure A.1.5: Impedance spectra of the LFP 5 at 50% SOC and different temperatures at 10 cycles.

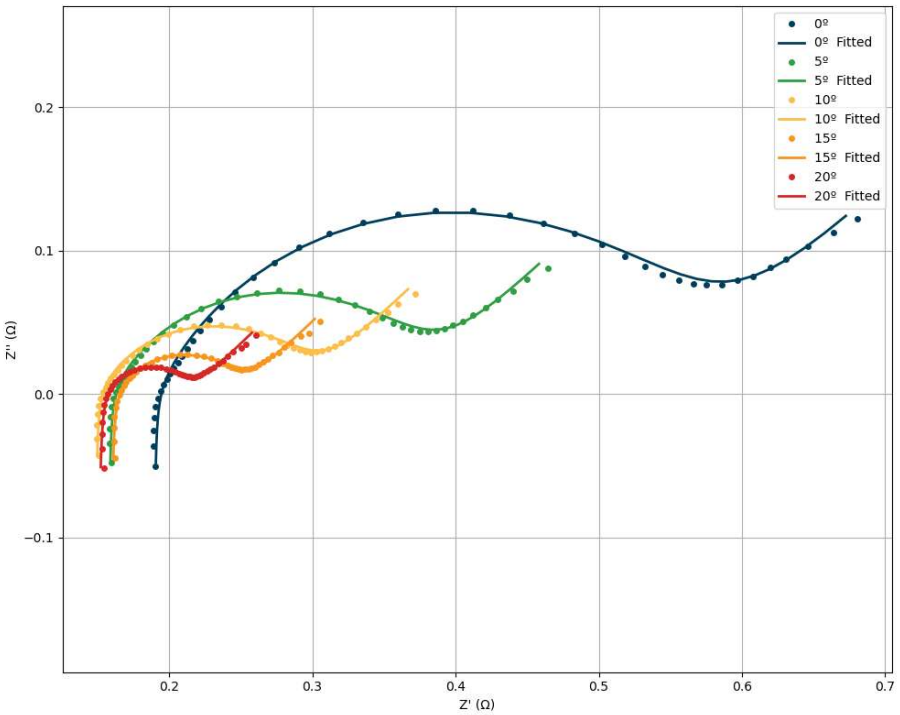


Figure A.1.6: Impedance spectra of the LFP 6 at 50% SOC and different temperatures at 10 cycles.

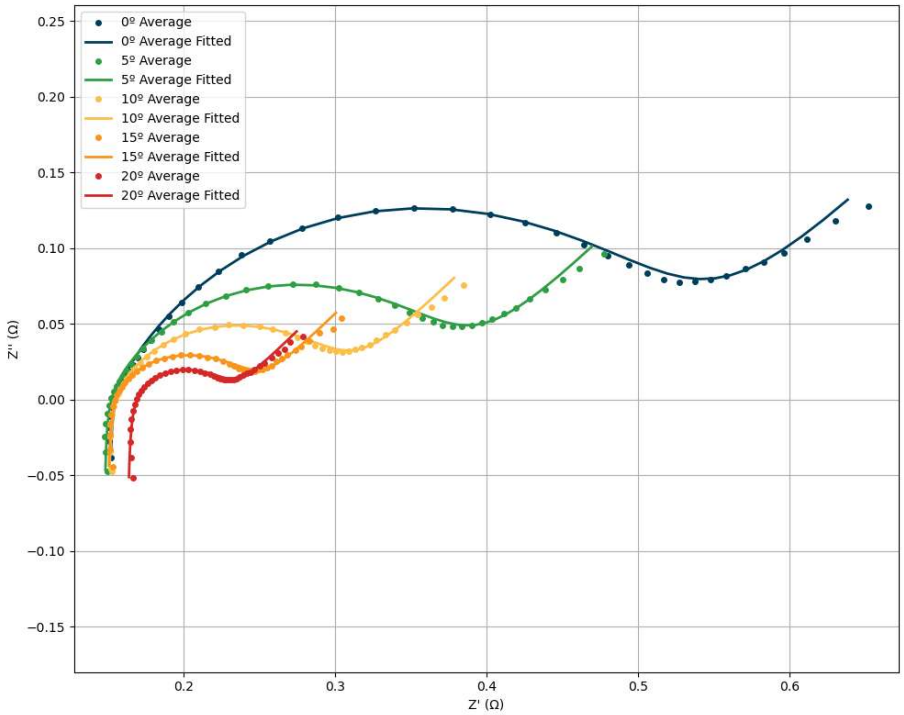


Figure A.1.7: Impedance spectra of the LFP 7 at 50% SOC and different temperatures at 10 cycles.

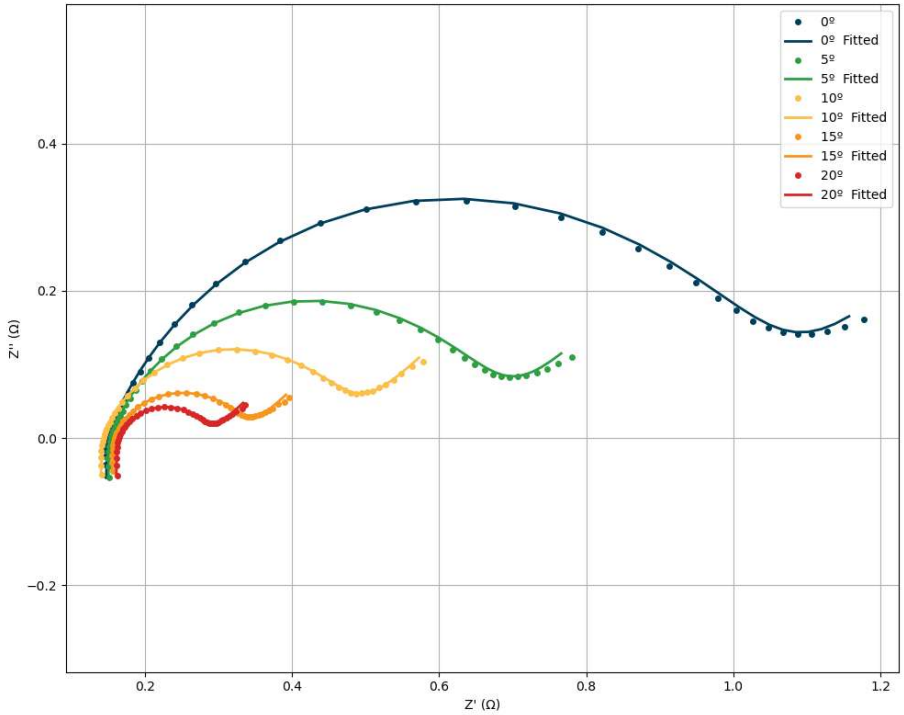


Figure A.1.8: Impedance spectra of the LFP 8 at 50% SOC and different temperatures at 10 cycles.

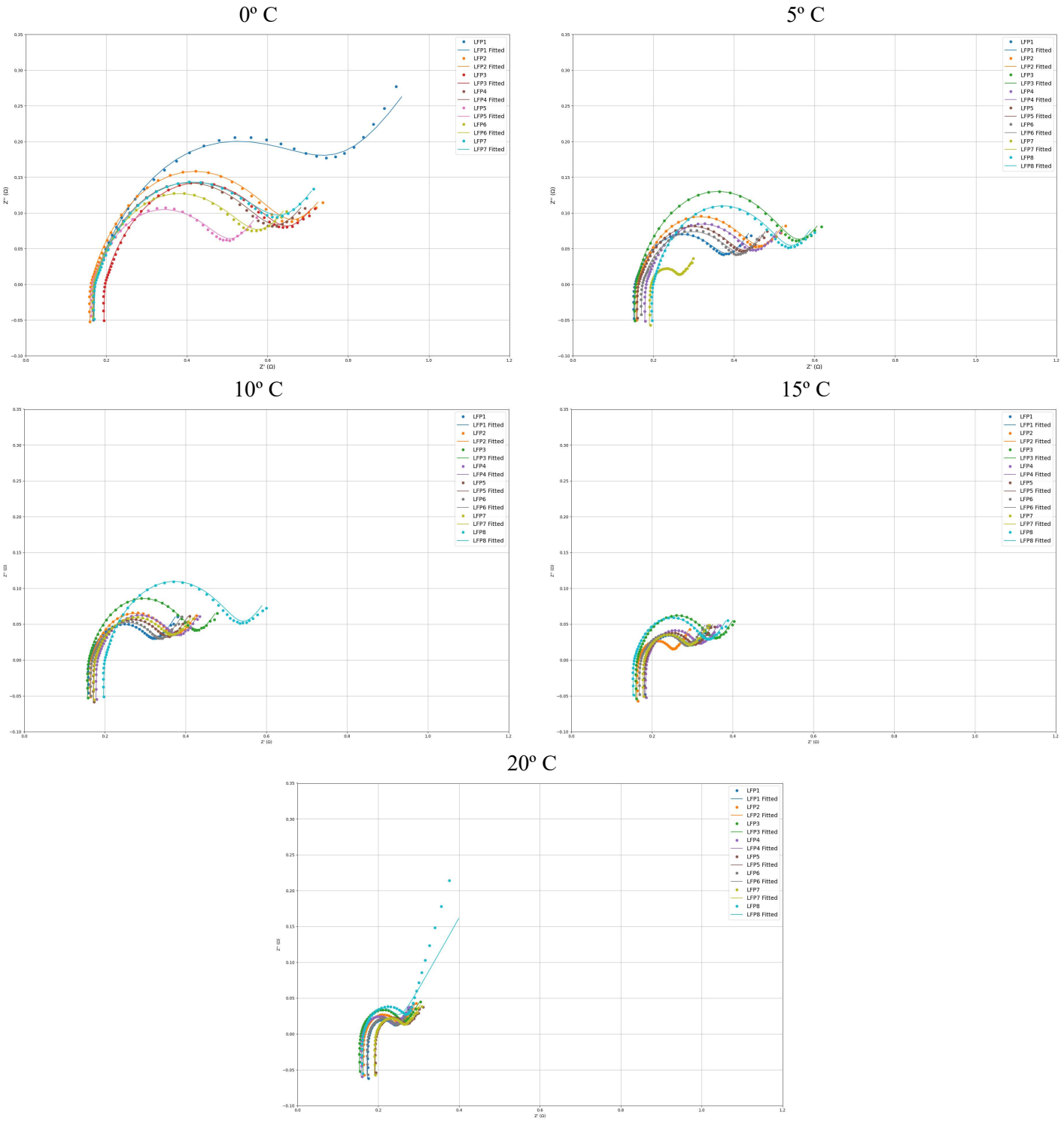


Figure A.1.9: Impedance spectra of all 8 LFP batteries at 60% SOC at different temperatures (0º,5º,10,15º and 20º) at 150 cycles

0º C

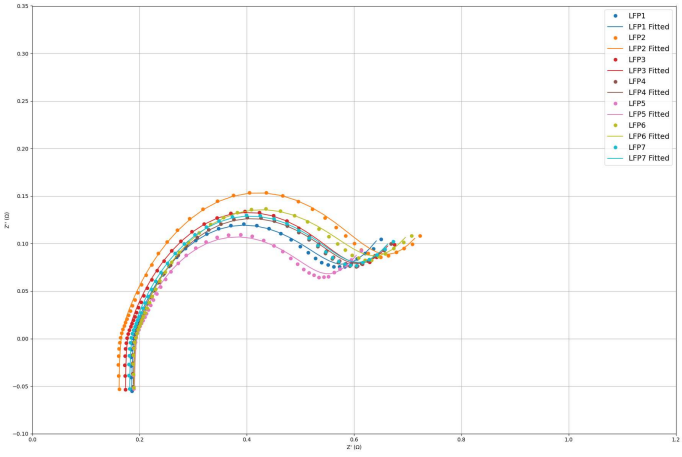


5º C

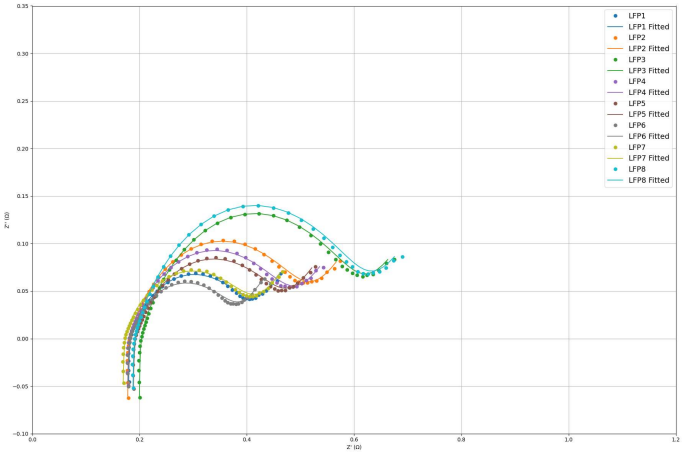


10º C

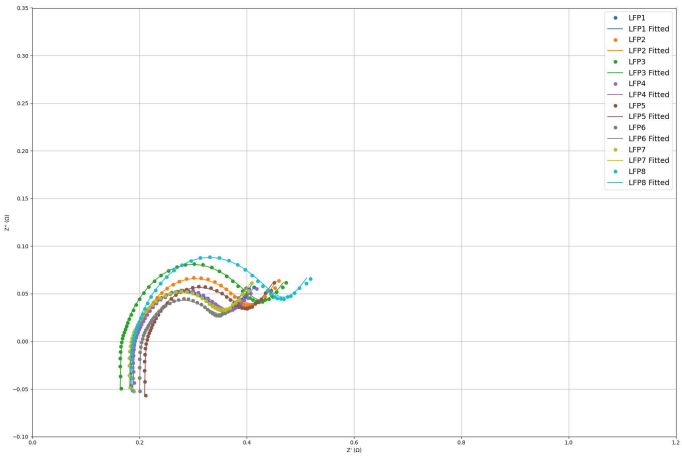


15º C

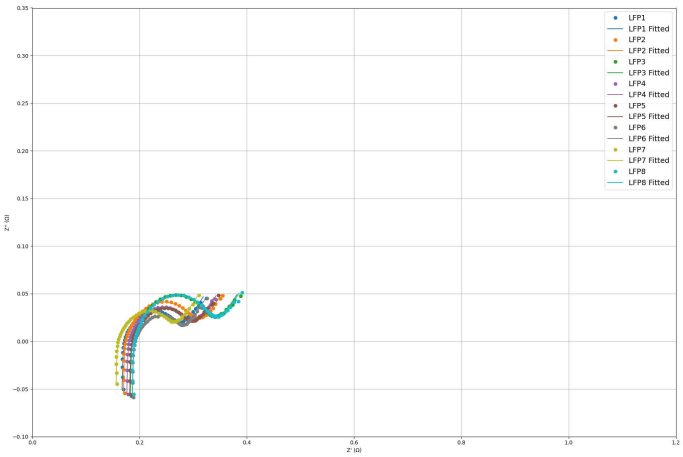


20º C

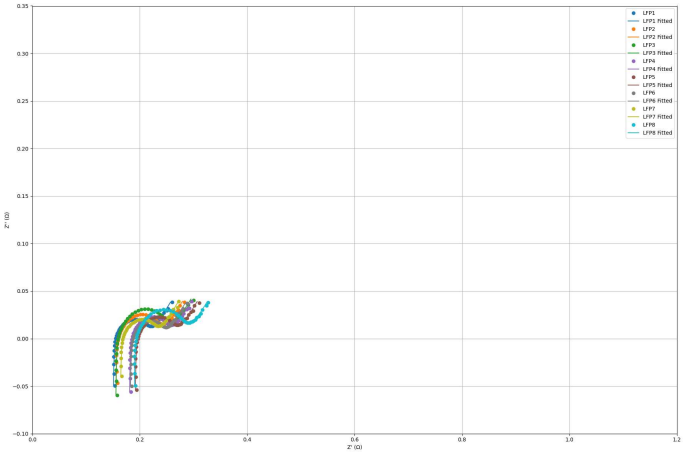


Figure A.1.10: Impedance spectra of all 8 LFP batteries at 60% SOC at different temperatures (0º,5º,10,15º and 20º) at 300 cycles

**0°**

| LFP 1 | | | | LFP 2 | | | |
|---|---|---|---|---|---|---|---|
| Element | Parameter | Value | Estimated Error (%) | Element | Parameter | Value | Estimated Error (%) |
| L1 | L | 0,000 | 2,029 | L1 | L | 0,000 | 2,622 |
| Rs | R | 0,152 | 0,358 | Rs | R | 0,144 | 0,419 |
| Rp | R | 0,383 | 0,897 | Rp | R | 0,525 | 0,962 |
| CPE | Y0 | 0,106 | 2,946 | CPE | Y0 | 0,084 | 2,861 |
| | N | 0,712 | 0,774 | | N | 0,731 | 0,740 |
| W1 | Y0 | 7,252 | 2,901 | W1 | Y0 | 7,348 | 4,363 |
| $\chi^2$ | | 0,004 | | $\chi^2$ | | 0,006 | |
| LFP 3 | | | | LFP 4 | | | |
| Element | Parameter | Value | Estimated Error (%) | Element | Parameter | Value | Estimated Error (%) |
| L1 | L | 0,000 | 2,045 | L1 | L | 0,000 | 2,536 |
| Rs | R | 0,147 | 0,324 | Rs | R | 0,143 | 0,401 |
| Rp | R | 0,739 | 0,724 | Rp | R | 0,415 | 0,942 |
| CPE | Y0 | 0,064 | 1,928 | CPE | Y0 | 0,098 | 3,044 |
| | N | 0,765 | 0,489 | | N | 0,716 | 0,790 |
| W1 | Y0 | 6,996 | 4,474 | W1 | Y0 | 7,673 | 3,524 |
| $\chi^2$ | | 0,004 | | $\chi^2$ | | 0,005 | |
| LFP 5 | | | | LFP 6 | | | |
| Element | Parameter | Value | Estimated Error (%) | Element | Parameter | Value | Estimated Error (%) |
| L1 | L | 0,000 | 2,372 | L1 | L | 0,000 | 2,654 |
| Rs | R | 0,152 | 0,357 | Rs | R | 0,189 | 0,361 |
| Rp | R | 0,414 | 0,886 | Rp | R | 0,373 | 1,014 |
| CPE | Y0 | 0,101 | 2,835 | CPE | Y0 | 0,109 | 3,433 |
| | N | 0,720 | 0,742 | | N | 0,709 | 0,921 |
| W1 | Y0 | 7,472 | 3,199 | W1 | Y0 | 8,152 | 3,477 |
| $\chi^2$ | | 0,004 | | $\chi^2$ | | 0,004 | |
| LFP 7 | | | | LFP 8 | | | |
| Element | Parameter | Value | Estimated Error (%) | Element | Parameter | Value | Estimated Error (%) |
| L1 | L | 0,000 | 2,572 | L1 | L | 0,000 | 2,233 |
| Rs | R | 0,150 | 0,354 | Rs | R | 0,146 | 0,354 |
| Rp | R | 0,372 | 0,871 | Rp | R | 0,885 | 0,797 |
| CPE | Y0 | 0,105 | 2,932 | CPE | Y0 | 0,058 | 1,946 |
| | N | 0,710 | 0,765 | | N | 0,774 | 0,497 |
| W1 | Y0 | 7,457 | 2,827 | W1 | Y0 | 6,611 | 5,530 |
| $\chi^2$ | | 0,004 | | $\chi^2$ | | 0,005 | |

**5°**

| LFP 1 | | | | LFP 2 | | | |
|---|---|---|---|---|---|---|---|
| Element | Parameter | Value | Estimated Error (%) | Element | Parameter | Value | Estimated Error (%) |
| L1 | L | 0,000 | 1,797 | L1 | L | 0,000 | 2,498 |
| Rs | R | 0,144 | 0,351 | Rs | R | 0,146 | 0,214 |
| Rp | R | 0,213 | 0,921 | Rp | R | 0,354 | 1,001 |
| CPE | Y0 | 0,142 | 3,763 | CPE | Y0 | 0,106 | 3,546 |
| | N | 0,682 | 0,985 | | N | 0,699 | 0,826 |
| W1 | Y0 | 10,660 | 2,366 | W1 | Y0 | 9,293 | 4,235 |
| $\chi^2$ | | 0,003 | | $\chi^2$ | | 0,007 | |
| LFP 3 | | | | LFP 4 | | | |
| Element | Parameter | Value | Estimated Error (%) | Element | Parameter | Value | Estimated Error (%) |
| L1 | L | 0,000 | 1,324 | L1 | L | 0,000 | 1,813 |
| Rs | R | 0,136 | 0,256 | Rs | R | 0,144 | 0,226 |
| Rp | R | 0,447 | 0,539 | Rp | R | 0,263 | 0,794 |
| CPE | Y0 | 0,073 | 1,858 | CPE | Y0 | 0,113 | 3,150 |
| | N | 0,756 | 0,451 | | N | 0,706 | 0,800 |
| W1 | Y0 | 9,005 | 2,711 | W1 | Y0 | 9,616 | 2,378 |
| $\chi^2$ | | 0,002 | | $\chi^2$ | | 0,003 | |
| LFP 5 | | | | LFP 6 | | | |
| Element | Parameter | Value | Estimated Error (%) | Element | Parameter | Value | Estimated Error (%) |
| L1 | L | 0,000 | 1,615 | L1 | L | 0,000 | 1,967 |
| Rs | R | 0,151 | 0,290 | Rs | R | 0,157 | 0,341 |
| Rp | R | 0,261 | 0,743 | Rp | R | 0,216 | 0,928 |
| CPE | Y0 | 0,118 | 2,921 | CPE | Y0 | 0,134 | 3,872 |
| | N | 0,706 | 0,750 | | N | 0,689 | 1,005 |
| W1 | Y0 | 9,566 | 2,167 | W1 | Y0 | 10,513 | 2,390 |
| $\chi^2$ | | 0,002 | | $\chi^2$ | | 0,003 | |
| LFP 7 | | | | LFP 8 | | | |
| Element | Parameter | Value | Estimated Error (%) | Element | Parameter | Value | Estimated Error (%) |
| L1 | L | 0,000 | 1,667 | L1 | L | 0,000 | 1,706 |
| Rs | R | 0,146 | 0,312 | Rs | R | 0,149 | 0,297 |
| Rp | R | 0,229 | 0,801 | Rp | R | 0,503 | 0,643 |
| CPE | Y0 | 0,126 | 3,283 | CPE | Y0 | 0,068 | 2,136 |
| | N | 0,694 | 0,843 | | N | 0,763 | 0,522 |
| W1 | Y0 | 9,335 | 1,994 | W1 | Y0 | 8,849 | 3,560 |
| $\chi^2$ | | 0,003 | | $\chi^2$ | | 0,003 | |

**10°**

| LFP 1 | | | | LFP 2 | | | |
|---|---|---|---|---|---|---|---|
| Element | Parameter | Value | Estimated Error (%) | Element | Parameter | Value | Estimated Error (%) |
| L1 | L | 0,000 | 1,422 | L1 | L | 0,000 | 1,916 |
| Rs | R | 0,145 | 0,319 | Rs | R | 0,133 | 0,341 |
| Rp | R | 0,147 | 0,918 | Rp | R | 0,218 | 0,799 |
| CPE | Y0 | 0,157 | 4,243 | CPE | Y0 | 0,117 | 3,447 |
| | N | 0,676 | 1,093 | | N | 0,701 | 0,860 |
| W1 | Y0 | 12,014 | 1,799 | W1 | Y0 | 11,408 | 2,357 |
| $\chi^2$ | | 0,002 | | $\chi^2$ | | 0,003 | |
| LFP 3 | | | | LFP 4 | | | |
| Element | Parameter | Value | Estimated Error (%) | Element | Parameter | Value | Estimated Error (%) |
| L1 | L | 0,000 | 1,591 | L1 | L | 0,000 | 1,936 |
| Rs | R | 0,160 | 0,211 | Rs | R | 0,198 | 0,317 |
| Rp | R | 0,284 | 0,504 | Rp | R | 0,132 | 1,369 |
| CPE | Y0 | 0,085 | 2,144 | CPE | Y0 | 0,291 | 5,413 |
| | N | 0,743 | 0,517 | | N | 0,614 | 1,631 |
| W1 | Y0 | 11,357 | 2,007 | W1 | Y0 | 17,494 | 2,849 |
| $\chi^2$ | | 0,001 | | $\chi^2$ | | 0,002 | |
| LFP 5 | | | | LFP 6 | | | |
| Element | Parameter | Value | Estimated Error (%) | Element | Parameter | Value | Estimated Error (%) |
| L1 | L | 0,000 | 1,549 | L1 | L | 0,000 | 1,762 |
| Rs | R | 0,139 | 0,310 | Rs | R | 0,148 | 0,318 |
| Rp | R | 0,170 | 0,826 | Rp | R | 0,152 | 0,904 |
| CPE | Y0 | 0,143 | 3,714 | CPE | Y0 | 0,152 | 4,197 |
| | N | 0,686 | 0,946 | | N | 0,677 | 1,078 |
| W1 | Y0 | 11,662 | 1,866 | W1 | Y0 | 12,393 | 1,892 |
| $\chi^2$ | | 0,002 | | $\chi^2$ | | 0,002 | |
| LFP 7 | | | | LFP 8 | | | |
| Element | Parameter | Value | Estimated Error (%) | Element | Parameter | Value | Estimated Error (%) |
| L1 | L | 0,000 | 1,805 | L1 | L | 0,000 | 1,226 |
| Rs | R | 0,211 | 0,253 | Rs | R | 0,139 | 0,220 |
| Rp | R | 0,151 | 0,935 | Rp | R | 0,335 | 0,473 |
| CPE | Y0 | 0,153 | 4,388 | CPE | Y0 | 0,072 | 1,906 |
| | N | 0,675 | 1,151 | | N | 0,763 | 0,447 |
| W1 | Y0 | 11,680 | 1,744 | W1 | Y0 | 9,011 | 1,852 |
| $\chi^2$ | | 0,001 | | $\chi^2$ | | 0,002 | |

**15°**

| LFP 1 | | | | LFP 2 | | | |
|---|---|---|---|---|---|---|---|
| Element | Parameter | Value | Estimated Error (%) | Element | Parameter | Value | Estimated Error (%) |
| L1 | L | 0,000 | 2,166 | L1 | L | 0,000 | 1,502 |
| Rs | R | 0,211 | 0,255 | Rs | R | 0,133 | 0,158 |
| Rp | R | 0,110 | 1,091 | Rp | R | 0,128 | 0,669 |
| CPE | Y0 | 0,183 | 5,365 | CPE | Y0 | 0,158 | 3,805 |
| | N | 0,660 | 1,417 | | N | 0,671 | 0,819 |
| W1 | Y0 | 14,164 | 1,672 | W1 | Y0 | 16,084 | 1,977 |
| $\chi^2$ | | 0,001 | | $\chi^2$ | | 0,002 | |
| LFP 3 | | | | LFP 4 | | | |
| Element | Parameter | Value | Estimated Error (%) | Element | Parameter | Value | Estimated Error (%) |
| L1 | L | 0,000 | 1,473 | L1 | L | 0,000 | 1,464 |
| Rs | R | 0,144 | 0,301 | Rs | R | 0,143 | 0,379 |
| Rp | R | 0,167 | 0,776 | Rp | R | 0,091 | 1,272 |
| CPE | Y0 | 0,113 | 3,809 | CPE | Y0 | 0,202 | 6,346 |
| | N | 0,717 | 0,917 | | N | 0,649 | 1,666 |
| W1 | Y0 | 15,441 | 2,372 | W1 | Y0 | 18,256 | 2,059 |
| $\chi^2$ | | 0,002 | | $\chi^2$ | | 0,002 | |
| LFP 5 | | | | LFP 6 | | | |
| Element | Parameter | Value | Estimated Error (%) | Element | Parameter | Value | Estimated Error (%) |
| L1 | L | 0,000 | 1,606 | L1 | L | 0,000 | 1,539 |
| Rs | R | 0,154 | 0,358 | Rs | R | 0,159 | 0,318 |
| Rp | R | 0,103 | 1,236 | Rp | R | 0,091 | 1,167 |
| CPE | Y0 | 0,192 | 6,089 | CPE | Y0 | 0,203 | 5,814 |
| | N | 0,659 | 1,590 | | N | 0,646 | 1,536 |
| W1 | Y0 | 16,231 | 2,080 | W1 | Y0 | 17,155 | 1,742 |
| $\chi^2$ | | 0,002 | | $\chi^2$ | | 0,002 | |
| LFP 7 | | | | LFP 8 | | | |
| Element | Parameter | Value | Estimated Error (%) | Element | Parameter | Value | Estimated Error (%) |
| L1 | L | 0,000 | 1,927 | L1 | L | 0,000 | 1,522 |
| Rs | R | 0,148 | 0,418 | Rs | R | 0,155 | 0,250 |
| Rp | R | 0,097 | 1,426 | Rp | R | 0,181 | 0,654 |
| CPE | Y0 | 0,209 | 6,918 | CPE | Y0 | 0,104 | 3,209 |
| | N | 0,644 | 1,843 | | N | 0,727 | 0,767 |
| W1 | Y0 | 15,862 | 2,166 | W1 | Y0 | 15,532 | 2,195 |
| $\chi^2$ | | 0,003 | | $\chi^2$ | | 0,002 | |

**20°**

| LFP 1 | | | | LFP 2 | | | |
|---|---|---|---|---|---|---|---|
| Element | Parameter | Value | Estimated Error (%) | Element | Parameter | Value | Estimated Error (%) |
| L1 | L | 0,000 | 1,436 | L1 | L | 0,000 | 1,201 |
| Rs | R | 0,136 | 0,380 | Rs | R | 0,142 | 0,304 |
| Rp | R | 0,069 | 1,423 | Rp | R | 0,088 | 1,012 |
| CPE | Y0 | 0,243 | 7,084 | CPE | Y0 | 0,181 | 5,273 |
| | N | 0,634 | 1,892 | | N | 0,663 | 1,339 |
| W1 | Y0 | 19,067 | 1,678 | W1 | Y0 | 19,073 | 1,676 |
| $\chi^2$ | | 0,002 | | $\chi^2$ | | 0,001 | |
| LFP 3 | | | | LFP 4 | | | |
| Element | Parameter | Value | Estimated Error (%) | Element | Parameter | Value | Estimated Error (%) |
| L1 | L | 0,000 | 1,328 | L1 | L | 0,000 | 1,454 |
| Rs | R | 0,143 | 0,274 | Rs | R | 0,151 | 0,376 |
| Rp | R | 0,112 | 0,817 | Rp | R | 0,076 | 1,438 |
| CPE | Y0 | 0,130 | 4,404 | CPE | Y0 | 0,223 | 7,210 |
| | N | 0,707 | 1,050 | | N | 0,639 | 1,916 |
| W1 | Y0 | 18,255 | 1,875 | W1 | Y0 | 20,218 | 2,013 |
| $\chi^2$ | | 0,002 | | $\chi^2$ | | 0,002 | |
| LFP 5 | | | | LFP 6 | | | |
| Element | Parameter | Value | Estimated Error (%) | Element | Parameter | Value | Estimated Error (%) |
| L1 | L | 0,000 | 1,375 | L1 | L | 0,000 | 1,387 |
| Rs | R | 0,182 | 0,267 | Rs | R | 0,150 | 0,387 |
| Rp | R | 0,073 | 1,255 | Rp | R | 0,066 | 1,590 |
| CPE | Y0 | 0,214 | 6,473 | CPE | Y0 | 0,243 | 7,919 |
| | N | 0,652 | 1,688 | | N | 0,631 | 2,129 |
| W1 | Y0 | 19,291 | 1,589 | W1 | Y0 | 21,066 | 1,882 |
| $\chi^2$ | | 0,001 | | $\chi^2$ | | 0,002 | |
| LFP 7 | | | | LFP 8 | | | |
| Element | Parameter | Value | Estimated Error (%) | Element | Parameter | Value | Estimated Error (%) |
| L1 | L | 0,000 | 1,582 | L1 | L | 0,000 | 1,415 |
| Rs | R | 0,162 | 0,410 | Rs | R | 0,160 | 0,266 |
| Rp | R | 0,069 | 1,766 | Rp | R | 0,128 | 0,812 |
| CPE | Y0 | 0,256 | 8,591 | CPE | Y0 | 0,120 | 4,331 |
| | N | 0,624 | 2,356 | | N | 0,715 | 1,033 |
| W1 | Y0 | 19,848 | 2,067 | W1 | Y0 | 18,520 | 2,165 |
| $\chi^2$ | | 0,002 | | $\chi^2$ | | 0,002 | |

Figure A.1.11: Fitting parameters for all LFP batteries in their initial stage.

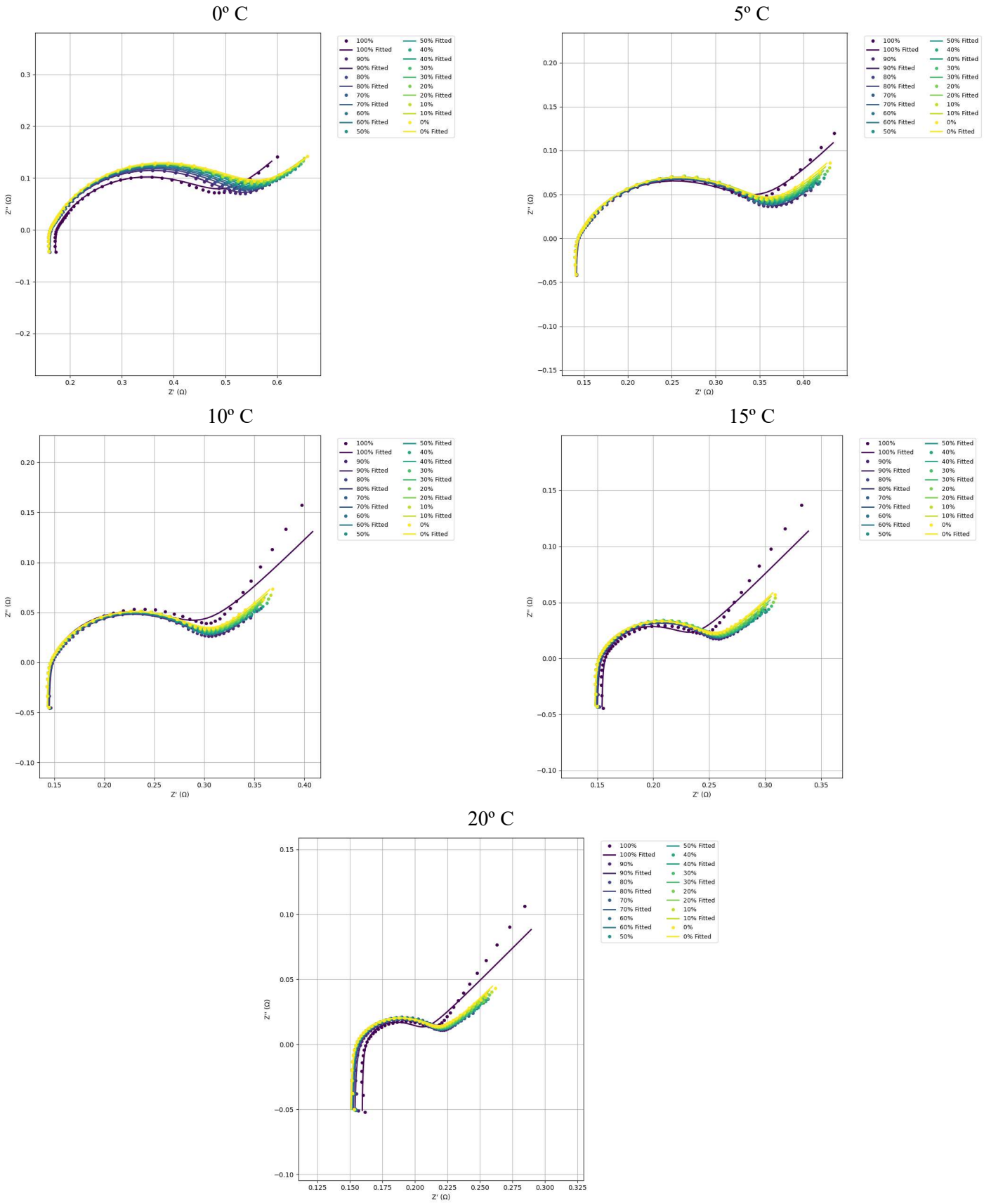


Figure A.1.12: 150 cycles Average Impedance spectra SOC evolution at the five temperatures defined

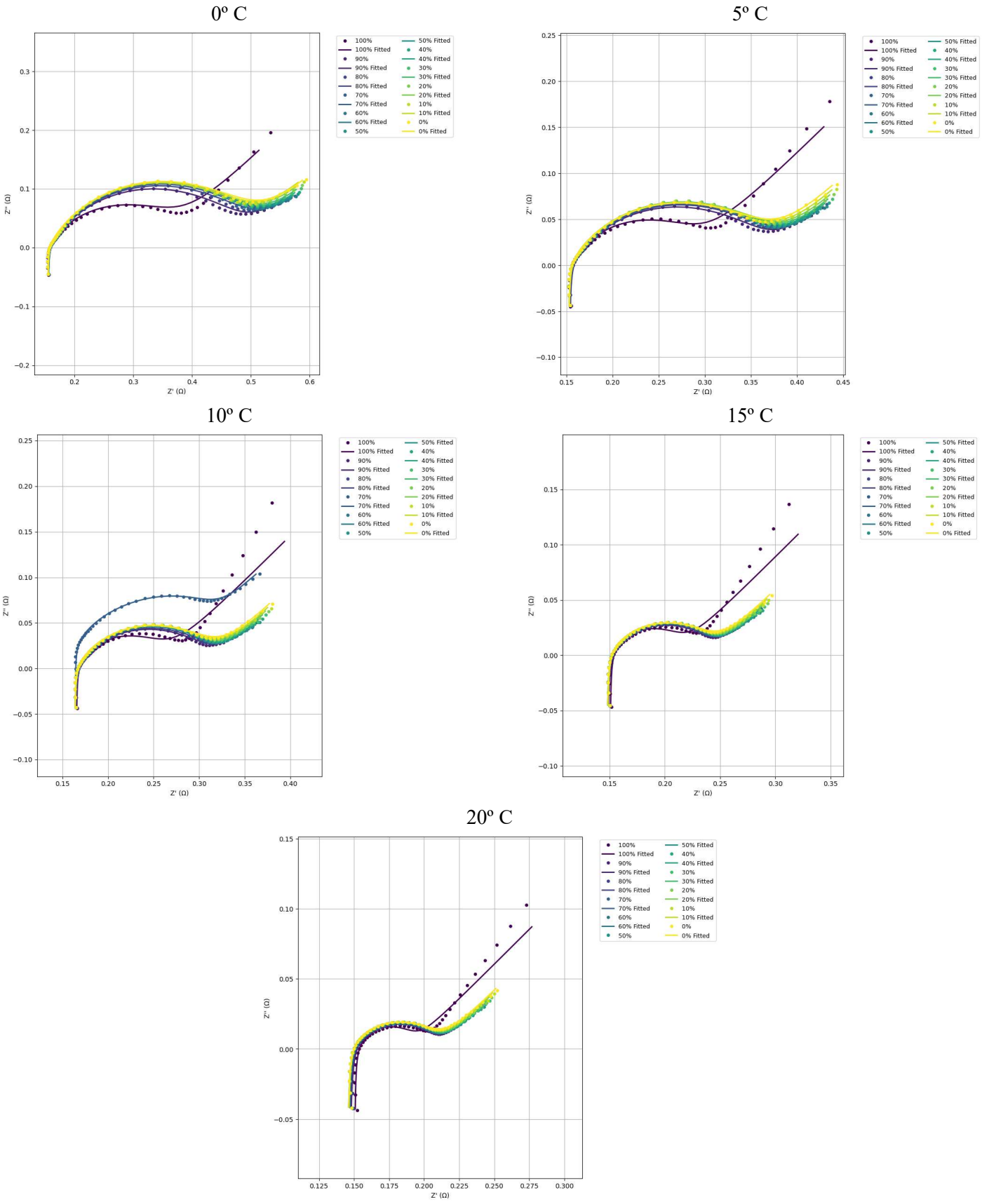


Figure A.1.13: 300 cycles Average Impedance spectra SOC evolution at the five temperatures defined

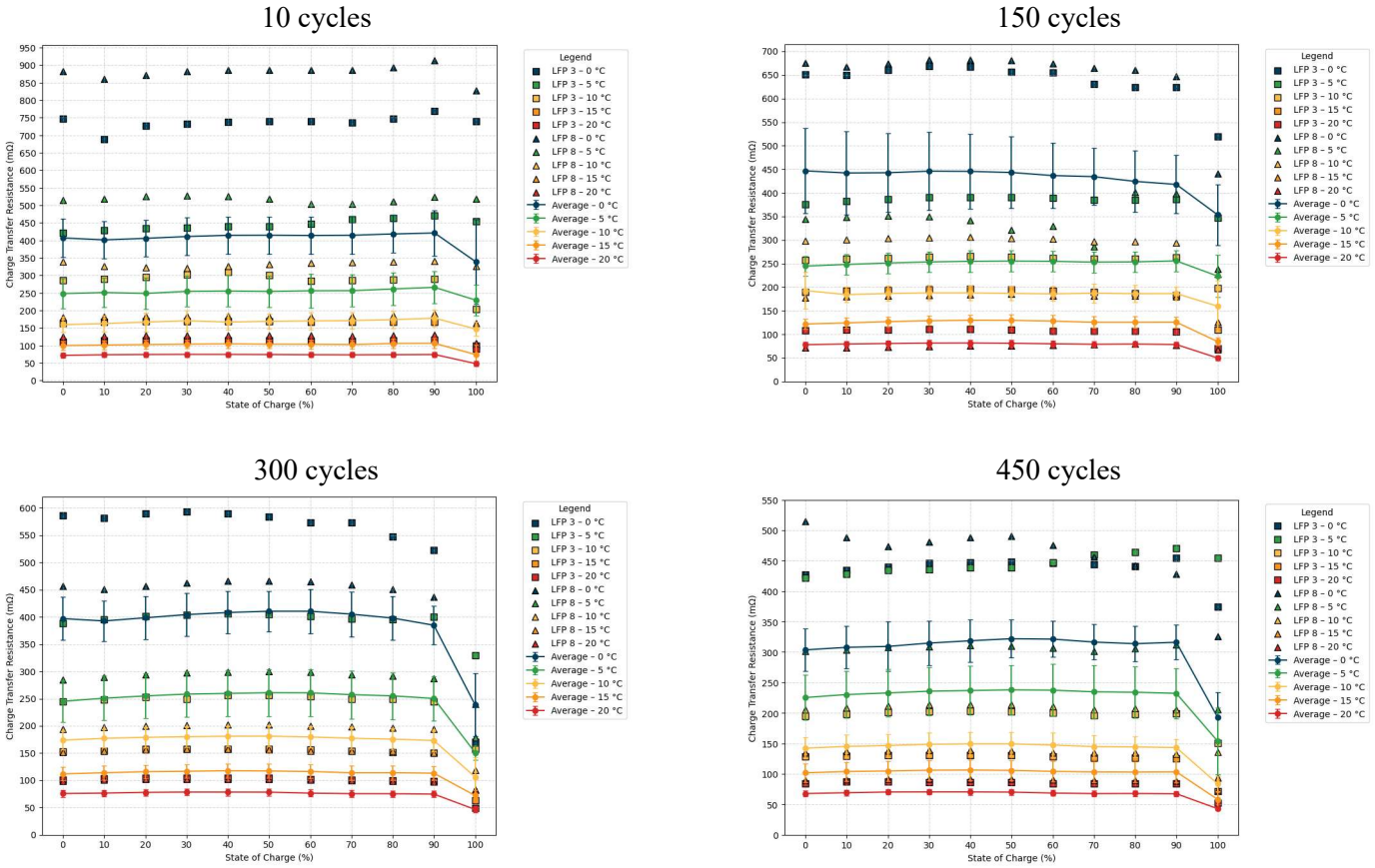


Figure A.1.14: Charge transfer resistance evolution with cycling at different temperatures with outliers' representation.

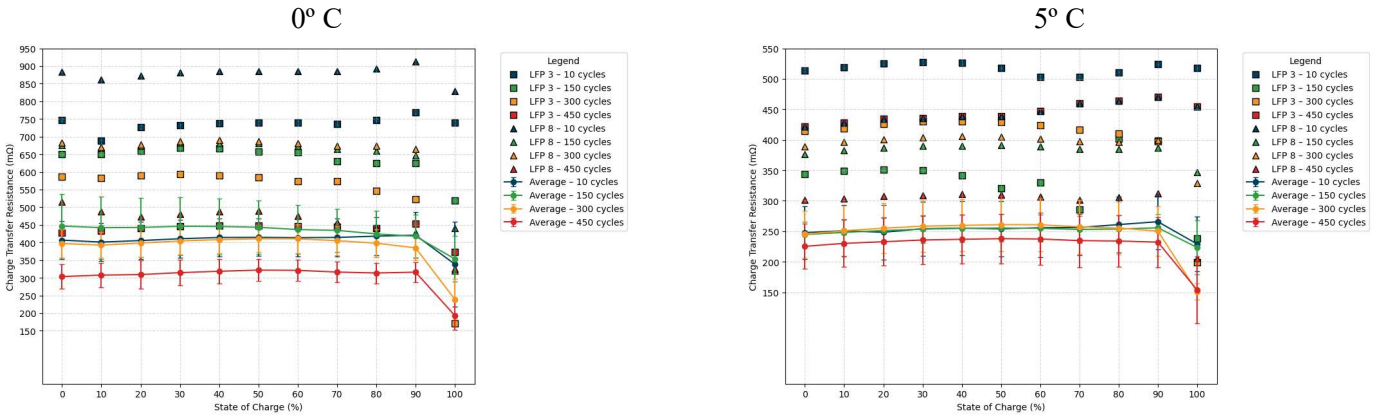

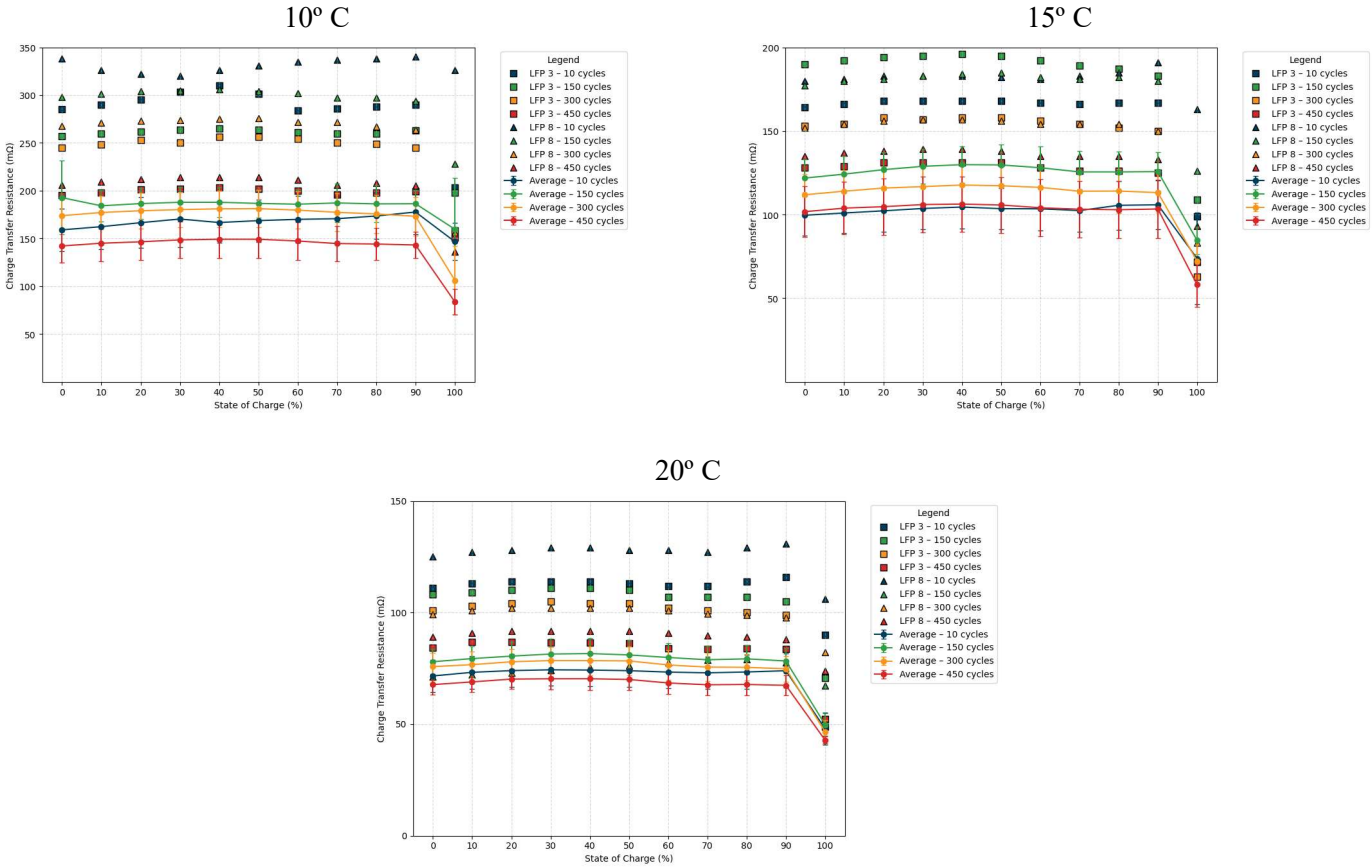


Figure A.1.15: Charge transfer resistance evolution with cycling at number of cycles with outliers' representation.

## A.2 Experimental setups and procedures

| Specification | Value |
|---|---|
| Chemistry | $LiFePO_4$ |
| Type | 10430 |
| Brand / Manufacturer | Enerpower / Vipow |
| Designation | IFR10430-200 |
| Nominal Voltage | 3.2 V |
| Charge Voltage | 3.6 V |
| Discharge Voltage | 2.5 V |
| Max Charge Current | 0.1 A |
| Capacity | 200 mAh |
| Continuous Load | 1C (~0.2 A) |
| Internal Resistance | <120 mΩ |
| Dimensions | Ø10 × 43 mm |
| Protection Circuit | None |
| Lifespan (100% / 80% / 60% DOD) | 1500 / 3000 / 6000 cycles |

Figure A.2.1:Specifications of ENERpower 10430 (AAA) LifePo4 3.2V 200 mAh 1C Flat.

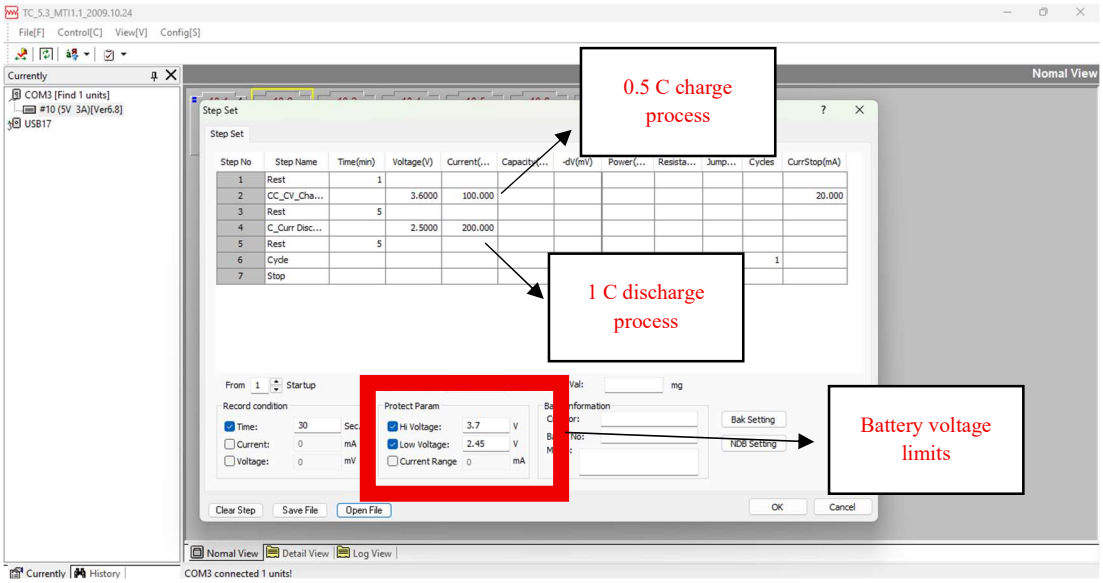


Figure A.2.2: MTI BST 8-Channel Battery Analyzer parameters for standard cycling.

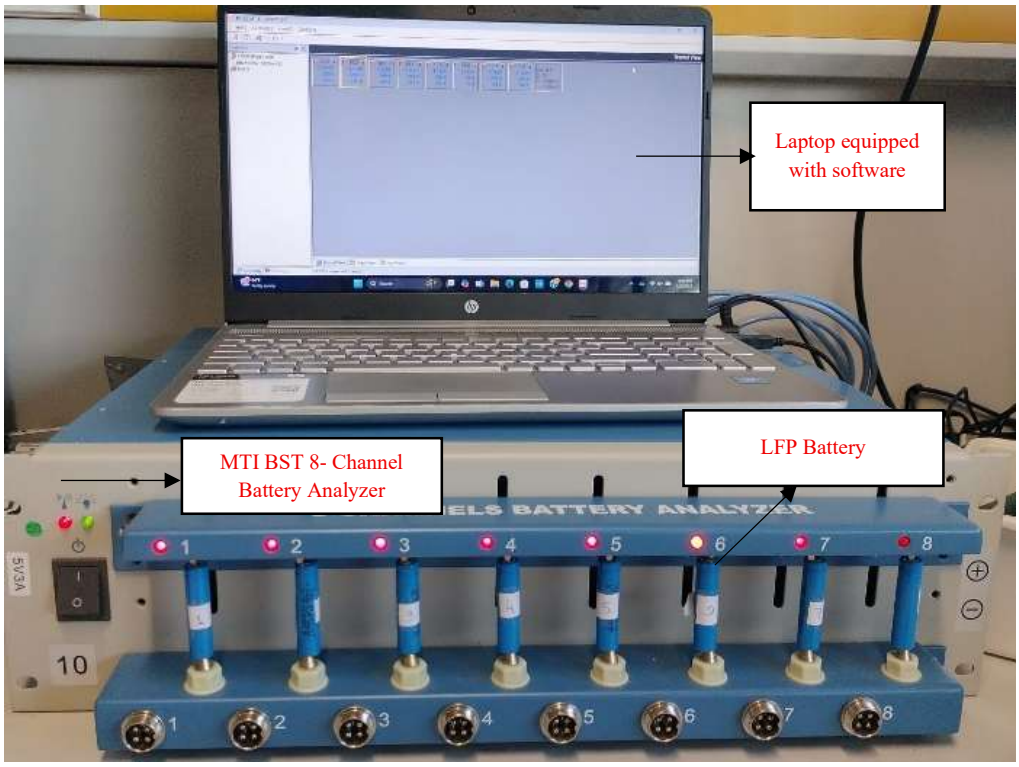


Figure A.2.3: MTI BST 8-Channel Battery Analyzer LFP battery setup


Figure A.2.4: Integration of the EIS Autolab equipment with the cryostat. On top of the Autolab device, a laptop equipped with control software and a thermocouple oil sensor is placed.

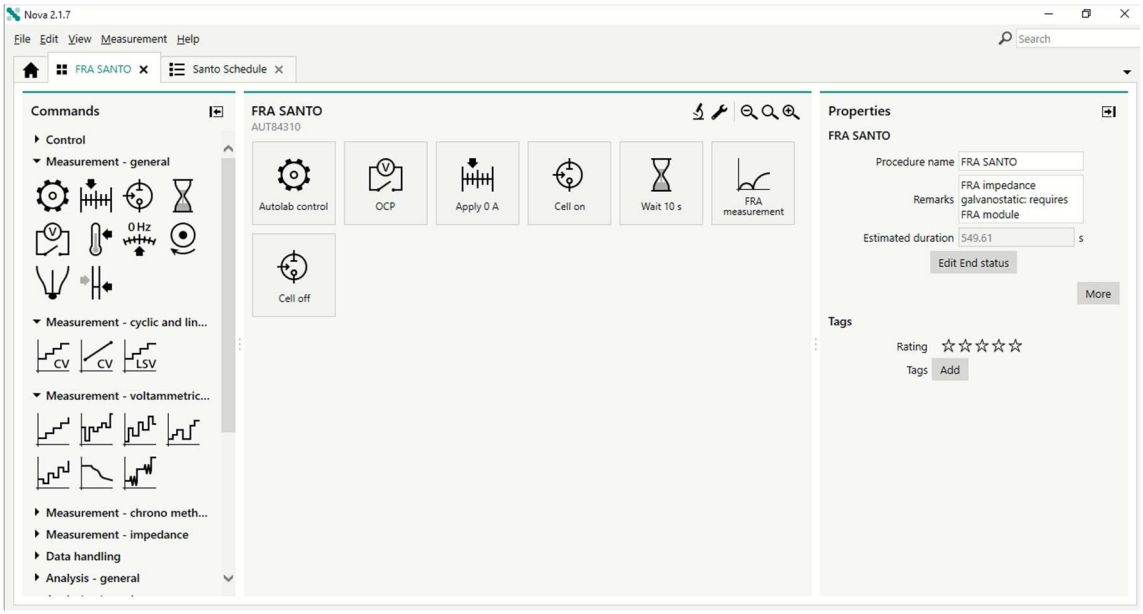


Figure A.2.5: FRA EIS Measurement *Nova Software protocol*

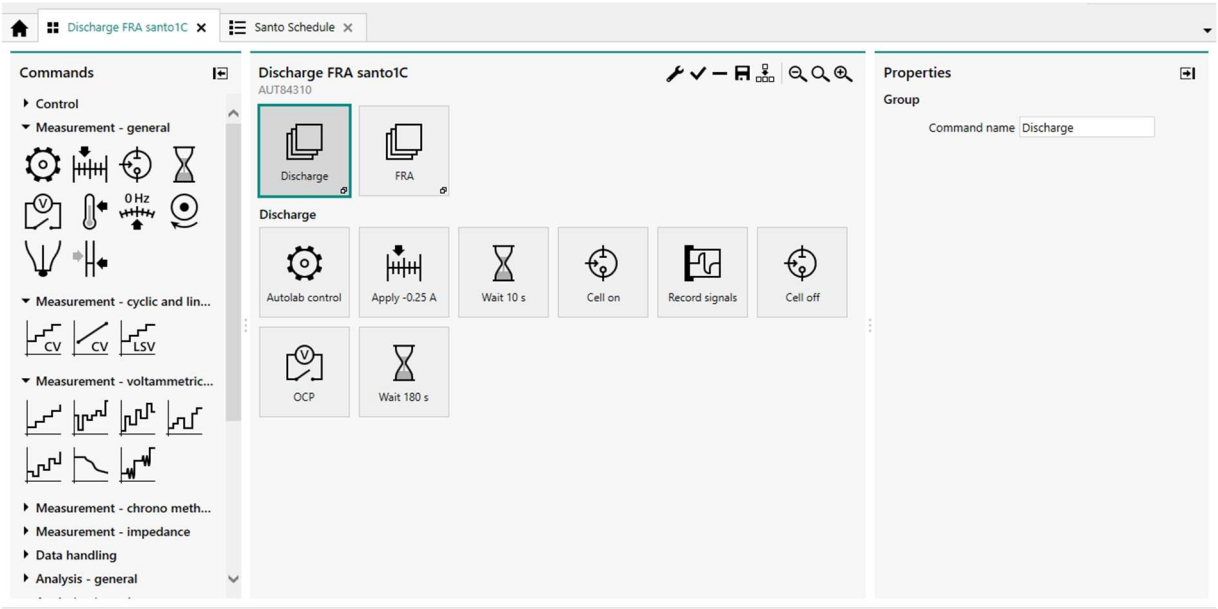


Figure A.2.6: Discharge FRA EIS Measurement *Nova Software protocol*

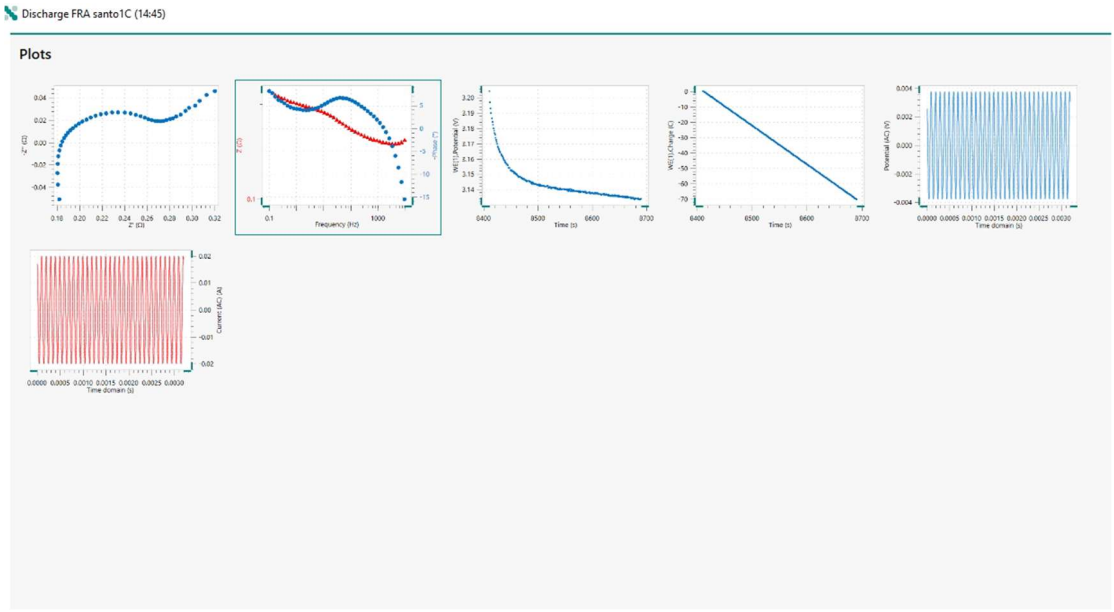


Figure A.2.7: Discharge FRA EIS Measurement graphical outputs (Nyquist Plot, Bode Plot, Discharge curve).

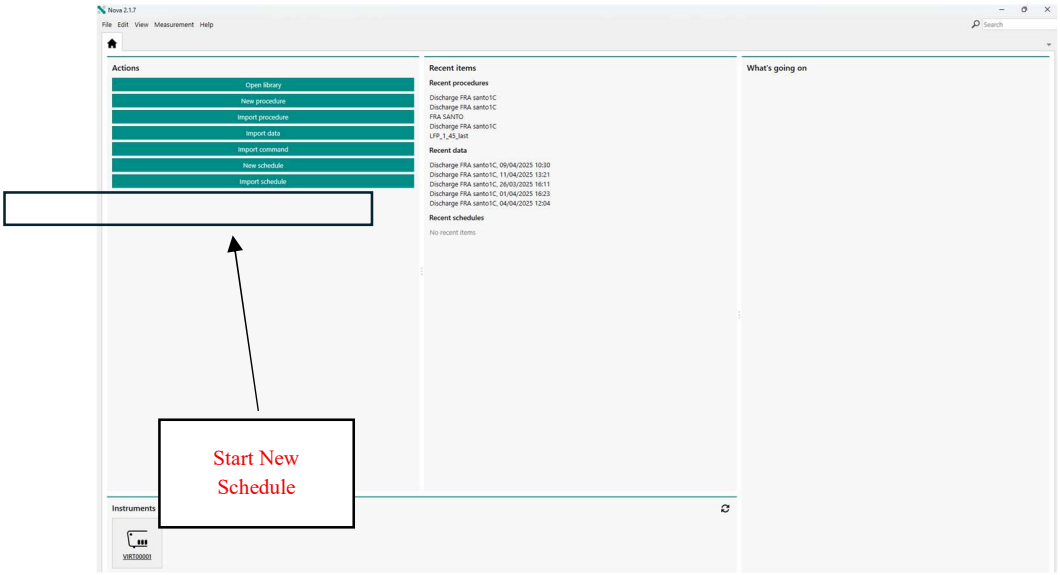


Figure A.2.8: Schedule setup for EIS Measurement (Step 1)

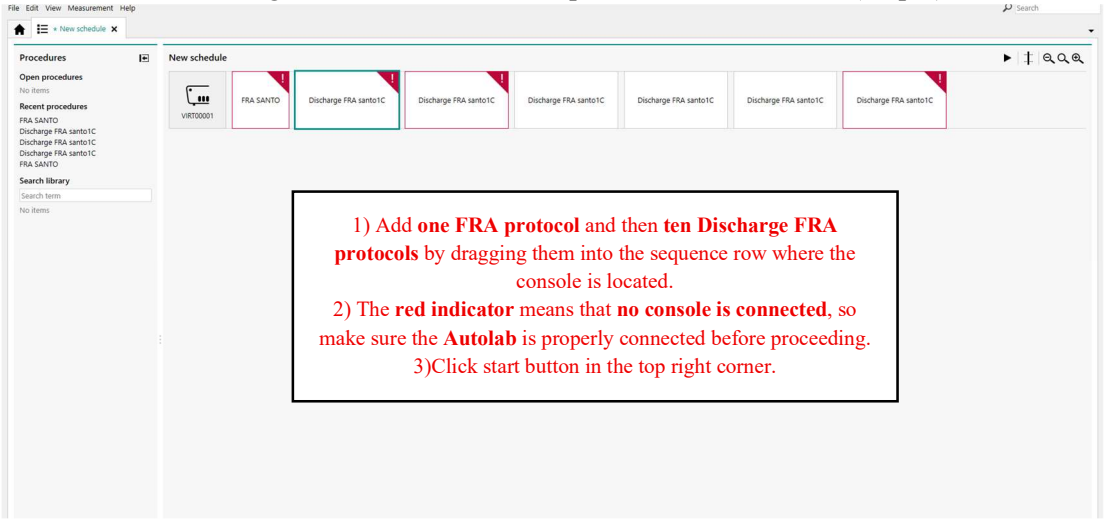


Figure A.2.9: Schedule setup for EIS Measurement (Step 2)

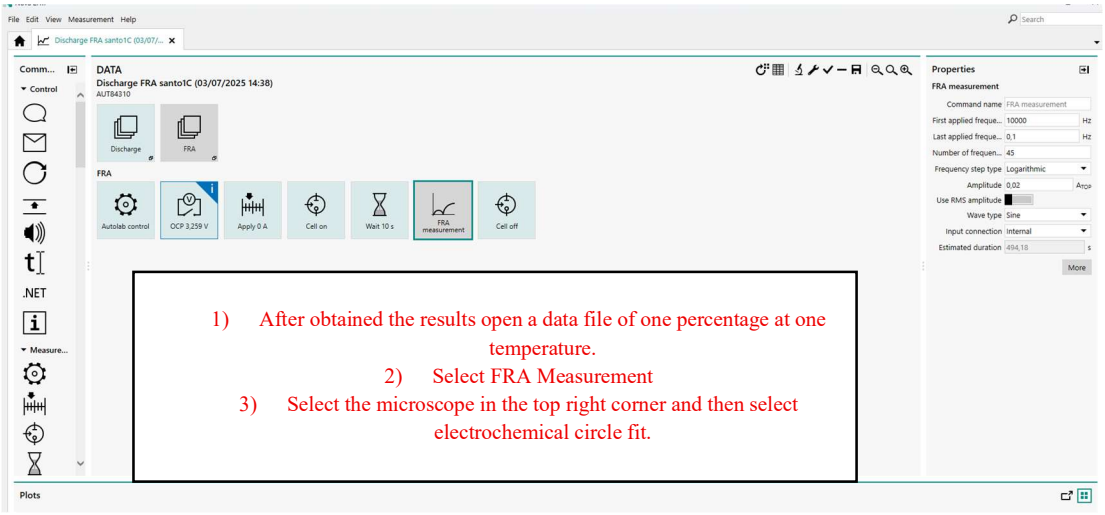


Figure A.2.10: Fitting procedure in Nova Software (Step 1)

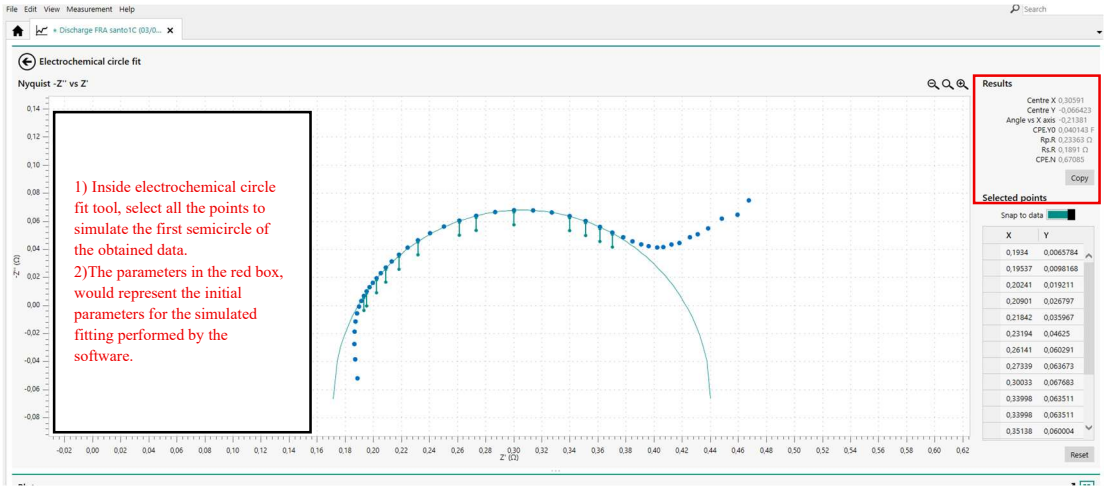


Figure A.2.11: Fitting procedure in Nova Software (Step 2)

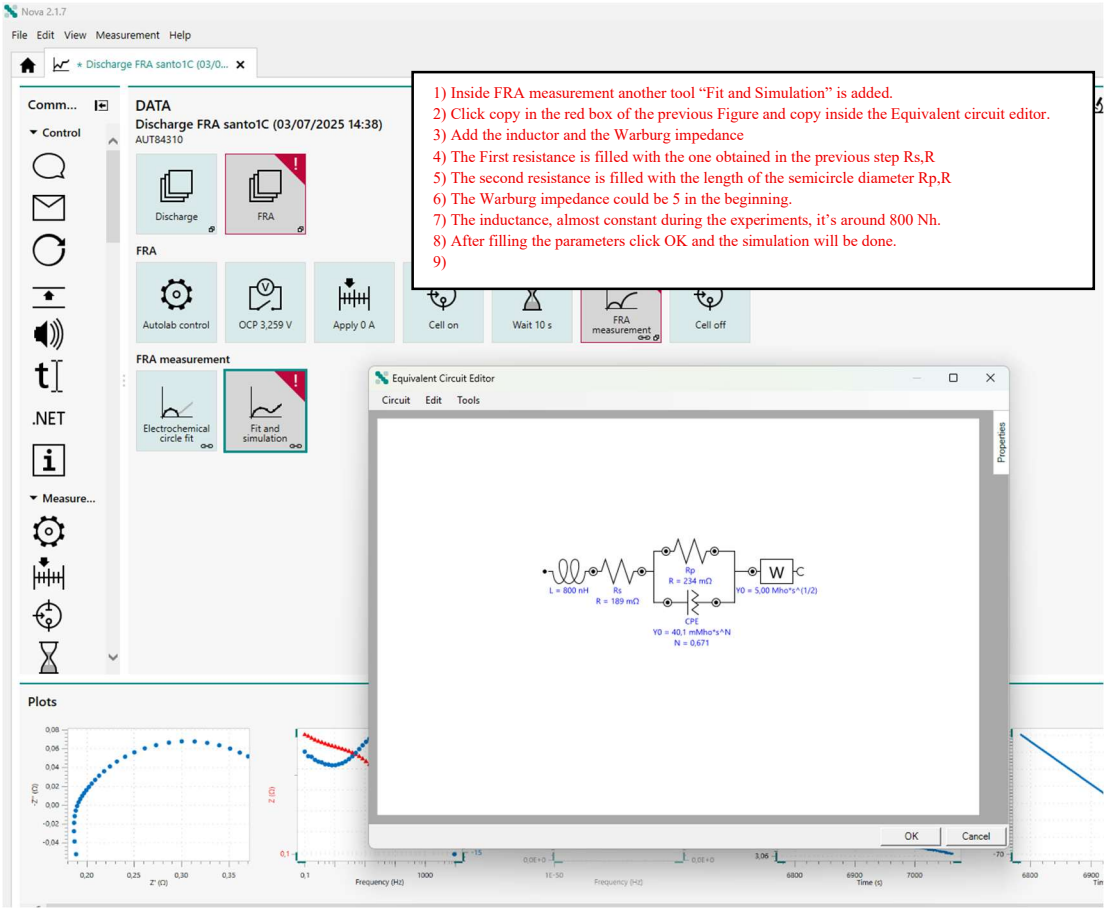


Figure A.2.12: Fitting procedure in Nova Software (Step 3)

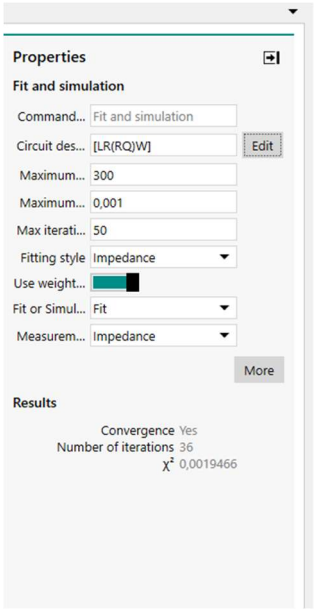


Figure A.2.13: Fitting procedure in Nova Software (Step 4)